NEW PERSPECTIVES ON MID-OCEAN RIDGE MAGMATIC SYSTEMS AND DEFORMATION IN THE UPPERMOST OCEANIC MANTLE FROM ACTIVE- AND PASSIVE-SOURCE SEISMIC IMAGING IN CASCADIA

by

BRANDON PAUL VANDERBEEK

A DISSERTATION

Presented to the Department of Earth Sciences
and the Graduate School of the University of Oregon
in partial fulfillment of the requirements
for the degree of
Doctor of Philosophy

September 2018

DISSERTATION APPROVAL PAGE

Student: Brandon Paul VanderBeek

Title: New Perspectives on Mid-Ocean Ridge Magmatic Systems and Deformation in the Uppermost Oceanic Mantle from Active- and Passive-Source Seismic Imaging in Cascadia

This dissertation has been accepted and approved in partial fulfillment of the requirements for the Doctor of Philosophy degree in the Department of Earth Sciences by:

Prof. Douglas R. Toomey	Chairperson/ Advisor
Prof. Emilie E. E. Hooft	Core Member
Prof. Eugene D. Humphreys	Core Member
Prof. Alan W. Rempel	Core Member
Prof. Allen D. Malony	Institutional Representative

and

Janet Woodruff-Borden	Vice Provost and Dean of the Graduate School

Original approval signatures are on file with the University of Oregon Graduate School.

Degree awarded September 2018

© 2018 Brandon Paul VanderBeek
This work is licensed under a Creative Commons
Attribution (United States) License.

DISSERTATION ABSTRACT

Brandon Paul VanderBeek

Doctor of Philosophy

Department of Earth Sciences

September 2018

Title: New Perspectives on Mid-Ocean Ridge Magmatic Systems and Deformation in the Uppermost Oceanic Mantle from Active- and Passive-Source Seismic Imaging in Cascadia

In this dissertation, I use seismic imaging methods to constrain the evolution of the oceanic upper mantle across the Juan de Fuca (JdF) and Gorda plates. This work begins by studying the geometry of the mantle magmatic system and patterns of mantle flow beneath the northern JdF ridge in relation to ridge-parallel changes in accretionary processes. I find that the dynamics of lithospheric rifting exert the primary control on the distribution of shallow mantle melts and variations in crustal thickness and composition. The orientation of mantle divergence beneath the JdF ridge, as inferred from seismic anisotropy, is oblique to the overlying plate divergence direction. Similar observations made at the East Pacific Rise and Mid-Atlantic ridge suggest plate motions alone do not control mantle flow patterns. On the contrary, stresses exerted at the base of the plate by the asthenospheric flow field may contribute to changes in plate motion prompting a reorientation of oceanic spreading segments. The mantle anisotropic fabric of the JdF plate interior is then investigated to identify whether the rotated mantle flow field observed beneath the JdF ridge persisted throughout the recent geologic past. However, observations suggest that the anisotropic structure created at the ridge partially reorganizes off-axis obscuring the paleo-flow geometry. Next, I focus on how the

physical state of the oceanic lithosphere evolves with time. Using local earthquake arrival times I test whether the seismic velocity structure of the upper mantle lithosphere is thermally controlled or dominated by heterogeneities introduced upon accretion at the ridge or by subsequent deformation off axis. Despite extensive surficial evidence of faulting across the Gorda plate, deformation appears to be restricted to crustal depths and mantle velocities are explained by conductive cooling. In contrast, the velocity structure of the JdF plate is inconsistent with conductively-cooled mantle. Hydration of the mantle lithosphere associated with tectonic discontinuities is invoked to explain anomalously slow P-wave speeds. Lastly, a joint inversion of teleseismic body and surface wave data is proposed to image the geometry of mantle upwelling and melt production beneath the JdF and Gorda Ridges.

This dissertation includes previously published and unpublished coauthored material.

CURRICULUM VITAE

NAME OF AUTHOR: Brandon Paul VanderBeek

GRADUATE AND UNDERGRADUATE SCHOOLS ATTENDED:

University of Oregon, Eugene, Oregon, USA
Western Michigan University, Kalamazoo, Michigan, USA

DEGREES AWARDED:

Doctor of Philosophy, Geological Sciences, 2018, University of Oregon
Bachelors of Science, Geology, 2011, Western Michigan University

AREAS OF SPECIAL INTEREST:

Seismic Imaging
Mid-ocean Ridge Magmatic and Tectonic Processes
Seismic Anisotropy

PROFESSIONAL EXPERIENCE:

Graduate Teaching Fellow, University of Oregon, 2012-2018

Field Technician, Environmental Resource Management, 2012

Undergraduate Research Assistant, Western Michigan University, 2010-2011

GRANTS, AWARDS, AND HONORS:

Weiser Scholarship, University of Oregon, 2017

Staples Scholarship, University of Oregon, 2016

Graduate Student Research Grant, Geological Society of America, 2016

Johnston Scholarship, University of Oregon, 2013, 2014, 2015, and 2016

PUBLICATIONS:

VanderBeek, B. P. and Rempel, A. W. (2018). On the importance of advective versus diffusive transport in controlling the distribution of methane hydrate in heterogeneous marine sediments. *Journal of Geophysical Research: Solid Earth*, 123.

VanderBeek, B. P. and Toomey, D. R. (2017). Shallow Mantle Anisotropy Beneath the Juan de Fuca Plate. *Geophysical Research Letters*, 44, 11, 382-11, 389.

Hooft, E. E., Nomikou, P., Toomey, D. R., Lampridou, D., Getz, C., Christopoulou, M. E., O'Hara, D., Arnoux, G. M., Bodmer, M., Gray, M., Heath, B. A., **VanderBeek, B. P.** (2017). Backarc tectonism, volcanism, and mass wasting shape seafloor morphology in the Santorini-Christiana-Amorgos region of the Hellenic Volcanic Arc. *Tectonophysics*, 712, 396-414.

Arnoux, G. M., Toomey, D. R., Hooft, E. E., Wilcock, W. S., Morgan, J., Warner, M., and **VanderBeek, B. P.** (2017). Seismic evidence that black smoker heat flux is influenced by localized magma replenishment and associated increases in crustal permeability. *Geophysical Research Letters*, 44, 1687-1695.

VanderBeek, B. P., Toomey, D. R., Hooft, E. E., and Wilcock, W. S. (2016). Segmentation of mid-ocean ridges attributed to oblique mantle divergence. *Nature Geoscience*, 9(8), 636-642.

Morgan, J., Warner, M., Arnoux, G., Hooft, E., Toomey, D., **VanderBeek, B.**, and Wilcock, W. (2016). Next-generation seismic experiments—II: wide-angle, multi-azimuth, 3-D, full-waveform inversion of sparse field data. *Geophysical Journal International*, 204(2), 1342-1363.

ACKNOWLEDGMENTS

I completed this dissertation with the guidance and support of many people. First and foremost, I must thank my advisors, Douglas Toomey and Emilie Hooft, whose time, patience, and encouragement contributed immensely to the success of this dissertation. Doug and Emilie have provided me with amazing travel opportunities and served as role models for how to maintain a healthy work-life balance (a skill I have not yet mastered). I am grateful for the friendships, conversations, and distractions of my fellow graduate students particularly Gillean Arnoux, Miles Bodmer, Joseph Byrnes, and Ben Heath. I owe special gratitude to Alan Rempel who advised me on research completely unrelated to this dissertation and, in doing so, helped expand my scientific knowledge. I would like to thank my committee members, Eugene Humphreys and Allen Malony, for their feedback on this work. I am grateful for the hospitality of Garett Ito (University of Hawaii) and Mike Warner and Joanna Morgan (Imperial College London) during my research visits to their institutions. Craig Rasmussen and Robert Yelle have provided superhero status computer assistance throughout my PhD. I must acknowledge the amazing work of the UO Department of Earth Sciences office staff. Finally, I would like to thank my family for their unconditional love and support (I know I should have called more).

This work was partially supported by the National Science Foundation under grants OCE-0454747, OCE-0651123, OCE-1139701, OCE-1333196, and EAR-1520694 to the University of Oregon.

For my friends and family, whose company kept me mostly sane throughout my PhD.

TABLE OF CONTENTS

Chapter Page

Chapter Page

LIST OF FIGURES

Figure Page

CHAPTER II

CHAPTER III

CHAPTER IV

Figure Page

CHAPTER V

LIST OF TABLES

Table Page

CHAPTER IV

CHAPTER I

INTRODUCTION

The motion of the oceanic lithosphere drives the vast majority volcanic and seismic activity on Earth. Along the mid-ocean ridge systems, oceanic lithosphere diverges exciting mantle upwelling and melting. These melts are focused toward the surface where they fuel the volcanism responsible for the generation of the world's seafloor. The lithosphere thickens through conductive cooling as it flows away from the MOR and is eventually recycled back into the mantle along subduction zones. Here, stress release along the interface between the downgoing oceanic plate and overriding lithosphere generates extensive seismicity. Compositional and structural heterogeneities inherited upon accretion and introduced by off-axis deformation of the plate are subducted where they may influence the seismic behavior of the plate interface and the generation of arc magmas. Owing to the remoteness of the ocean floor, observational constraints on the structure of the upper mantle are limited. Consequently, the nature of mantle upwelling and and the processes that govern lithospheric accretion are poorly constrained. In particular, how is mantle upwelling and melt production at depth connected to shallow tectonic and magmatic processes occurring along the MOR system? How heterogeneous is the oceanic lithosphere? Does the structure of the mantle lithosphere influence the seismic behavior of subduction zones and arc magmatic processes? This dissertation begins to address these questions by studying the evolution of oceanic upper mantle beneath the Juan de Fuca (JdF) plate system from the ridge to the trench. Using complimentary seismic datasets collected offshore of the Cascadia margin,

I tomographically image the seismic velocity structure of the upper mantle at progressively larger scales. These images are used to place constraints on mantle physical properties.

In Chapter II, I use active-source seismic data to probe the structure of the shallow mantle magmatic system and pattern of mantle flow beneath the Endeavour segment on the northern JdF ridge. I investigate whether the morphologic expression of the ridge and along-strike variations in tectonic and magmatic processes reflect the dynamics of mantle upwelling and melting below or are controlled by the rifting of the young oceanic plate above. Tomographic images reveal that the more heavily tectonized and volcanically less active ends of the Endeavour segment are underlain by broad regions of mantle melt at the base of the Moho. In contrast, the volcanically more active segment center is underlain by a narrower mantle magmatic system containing volumetrically less melt. The orientation of mantle flow inferred from seismic anisotropy is rotated 12° from the orientation of plate divergence suggesting that mantle flow at shallow depths is influenced by forces other than the overlying plate divergence. I synthesize these results with geophysical and petrological observations from a variety of MOR segments to develop a new conceptual model for the structure of oceanic spreading centers. In this model, the distribution of melt is controlled by the axial thermal structure rather than variations in the production of melt from the upwelling mantle. The thermal structure is controlled by the overlying rift geometry which evolves in response to stresses exerted along the base of the plate by mantle flow that is oblique to the motion of the lithosphere.

The skew between the plate and mantle divergence directions beneath the northern JdF ridge discussed in Chapter II is surprising. However, similar patterns have been observed beneath the fast-spreading East Pacific Rise and slow-spreading Mid-Atlantic Ridge suggesting that plate and mantle flow directions may be misaligned globally. Because the upper oceanic mantle is progressively frozen into the lithosphere and paleo-spreading directions are recorded by seafloor magnetization and basement lineations, the relationship between relative plate motion and mantle flow in the geologic past may be discerned through seismic investigation of plate interiors. In Chapter III, I test whether the oblique pattern of mantle divergence inferred beneath the present-day northern JdF ridge is characteristic of the entire JdF ridge system over recent (< 10 Myr) geologic time. Azimuthal variations in local earthquake P-wave arrival times are used to measure the mean anisotropic fabric of the entire JdF plate. The results are inconclusive. I find evidence that prior to being accreted to the oceanic lithosphere, the anisotropic fabric of the uppermost 10 km of the mantle reorganizes as it is transported off-axis to more closely align with the direction of absolute plate motion. Consequently, the pattern of mantle flow beneath the paleo-spreading center is obscured. The results do hold promise for inferring paleo-absolute plate motion directions from measurements of lithospheric anisotropy.

Chapter IV is an extension of the study in Chapter III and explores mantle heterogeneity within the JdF and internally deforming Gorda plates using local earthquake tomography. I construct images of P-wave velocity and use these to constrain the thermal structure and hydration state of the oceanic lithosphere as a function of plate age. Despite surficial evidence of extensive active faulting, the velocity structure of the

Gorda uppermost mantle is remarkably consistent with predictions from a conductive cooling model. Observations from seismic anisotropy suggest that brittle deformation is restricted to crustal depths. In contrasts, the seismic velocity structure of the JdF plate does not exhibit a clear age dependence. Pronounced mantle low-velocity zones are found along the southern edge of the JdF plate and attributed to alteration by seawater. Large tectonic offsets near the low-velocity anomalies are hypothesized to provide pathways for fluid circulation. While the mantle lithosphere offshore Cascadia contains a number of heterogeneities, there is not a clear relationship between these anomalies and along-strike variations in subduction zone processes

Chapters II-IV focused on the structure of the shallow (i.e. within 10 km of the Moho) mantle and explored its evolution from ridge to trench. In Chapter V, I consider the larger scale dynamics of the lithosphere-asthenosphere system beneath Cascadia. To better constrain the geometry of mantle flow and upwelling beneath the JdF and Gorda ridges, I propose to jointly invert teleseismic body and surface wave arrivals for the shear velocity structure of the upper ~500 km of the mantle. These two seismic phases have complimentary sensitivities to earth structure and their joint analysis holds promise for yielding higher resolution images of the Earth. Chapter V provides scientific motivation for the joint inversion and develops the methodology.

Chapter II of this dissertation was coauthored with Douglas R. Toomey, Emilie E. E. Hooft, and William S. D. Wilcock and published in *Nature Geoscience* in August 2016. Chapter III was coauthored with Douglas R. Toomey and published in *Geophysical Research Letters* in November 2017. Chapter IV is in preparation for publications and was coauthored with Douglas R. Toomey.

CHAPTER II

SEGMENTATION OF MID-OCEAN RIDGES ATTRIBUTED TO OBLIQUE MANTLE DIVERGENCE

From VanderBeek, B. P., Toomey, D. R., Hooft, E. E., & Wilcock, W. S. (2016). Segmentation of mid-ocean ridges attributed to oblique mantle divergence. *Nature Geoscience*, *9*(8), 636.

1.0 Introduction

Since the discovery that Earth's mid-ocean ridge system is divided into segments (Schouten et al., 1985; Macdonald et al., 1988; Sempéré et al., 1990) a wealth of observations have shown that there are systematic, along-axis variations in tectonic and magmatic processes (Macdonald et al., 1988; Langmuir et al., 1986; Kent et al., 2000; Carbotte et al., 2015). Between transform faults, the boundaries of ridge segments are defined by long-lived, non-transform tectonic offsets or second-order ridge crest discontinuities (Macdonald et al., 1988; Sempéré et al., 1990; Figure 1) that often occur at axial depth maxima and that migrate along the plate boundary. These second-order discontinuities include overlapping spreading centres (OSCs) at fast- and intermediate-spreading rates, and oblique shear zones at slow-spreading rates. The origin of non-transform tectonic offsets and their relations to segment-scale magmatic processes remains actively debated (Schouten et al., 1985; Macdonald et al., 1988; Kent et al., 2000; Carbotte et al., 2015; Lonsdale, 1989; Carbotte et al., 2004; Toomey et al., 2007).

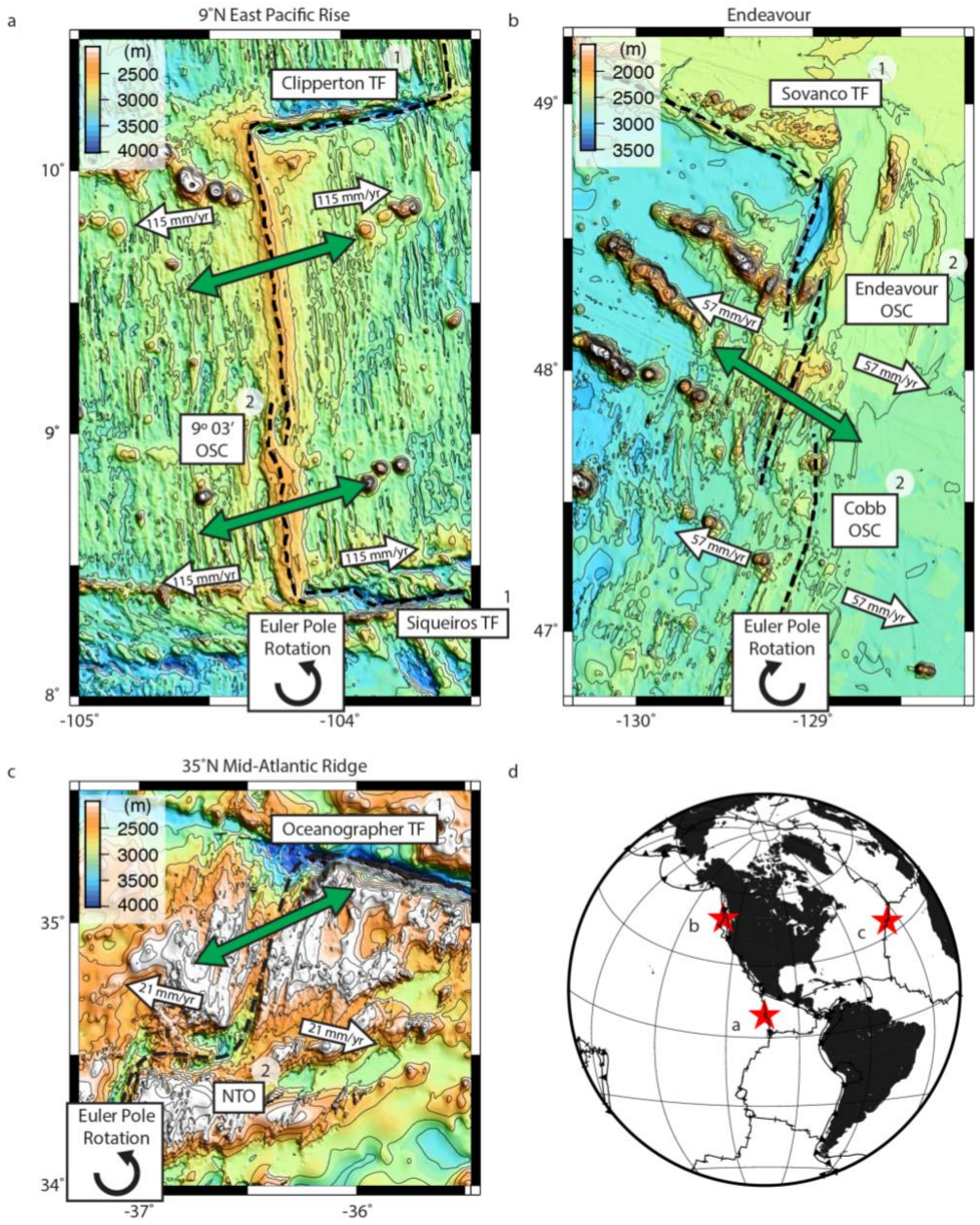

Figure 1. Tectonic segmentation of fast-, intermediate-, and slow-spreading ridges. Bathymetric maps of (a) the East Pacific Rise; (b) the Endeavour region of the JdFR; and (c) the Mid-Atlantic Ridge. Dashed lines show plate boundaries. Transform faults (TF), overlapping spreading centres (OSC), and non-transform offsets (NTO) are labeled; numbers indicate order of a tectonic discontinuity (Macdonald et al., 1988). White arrows show the spreading direction and full-spreading rate (Gripp & Gordon, 2002). Green arrows indicate azimuth of seismic anisotropy for the EPR (Toomey et al., 2007), JdFR (this study), and MAR (Dunn et al., 2005). Recent rotations in the Euler pole of each plate system (Pockalny et al., 1997; Sloan & Patriat, 1992; Wilson, 1988) are indicated. (d) Map showing regional location of ridge segments (red stars).

The prevailing hypothesis for segmentation of spreading centres attributes second-order offsets to variations in magma supply from the upwelling mantle. In this

view, segment centres overly sites of increased melt supply and magma is redistributed along axis at crustal or mantle depths toward magma-starved segment ends (Schouten et al., 1985; Macdonald et al., 1988; Carbotte et al., 2004; Bell & Buck, 1992). Alternatively, competing hypotheses suggest that changes in the plate-spreading direction are related to the formation of tectonic offsets (Lonsdale, 1989) and to a misalignment between sub-ridge mantle and crustal processes (Toomey et al., 2007). Here, we seismically image the geometry of mantle flow and the distribution of shallow mantle melt beneath the intermediate-spreading Endeavour segment of the Juan de Fuca Ridge (JdFR). We synthesize our results with observations from other spreading environments to identify the mechanisms responsible for tectonic and magmatic segmentation of the mid-ocean ridge system.

2.0 Experiment Geometry and Tomographic Imaging

Figure 2 shows the location of seismic sources and receivers used to construct our tomographic model of the shallow mantle beneath the Endeavour segment of the JdFR. We use arrival times of seismic energy refracted beneath the Mohorovičić (Moho) discontinuity (Pn arrivals) to image the upper 4 km of the mantle within an area extending 20 km by 100 km in the cross- and along-axis directions, respectively. Over 5000 Pn arrivals provide excellent sampling of mantle structure and previous studies (Weekly et al., 2014; Soule et al., 2016) provide a three-dimensional starting model of crustal velocity and thickness (see Appendix A).

The Pn data plotted by azimuth show a $\cos 2\theta$-pattern, which is indicative of azimuthal seismic anisotropy (Figure 3). The azimuth of the fast-axis of mantle anisotropy is $122° \pm 1°$ and the magnitude is $4.7\% \pm 0.4\%$ (see Appendix A). The

azimuth of anisotropy is rotated 12° clockwise from the predicted plate-spreading direction (Gripp & Gordon, 2002). Examination of subsets of Pn data do not show evidence for along-axis variations in anisotropic structure (see Appendix A).

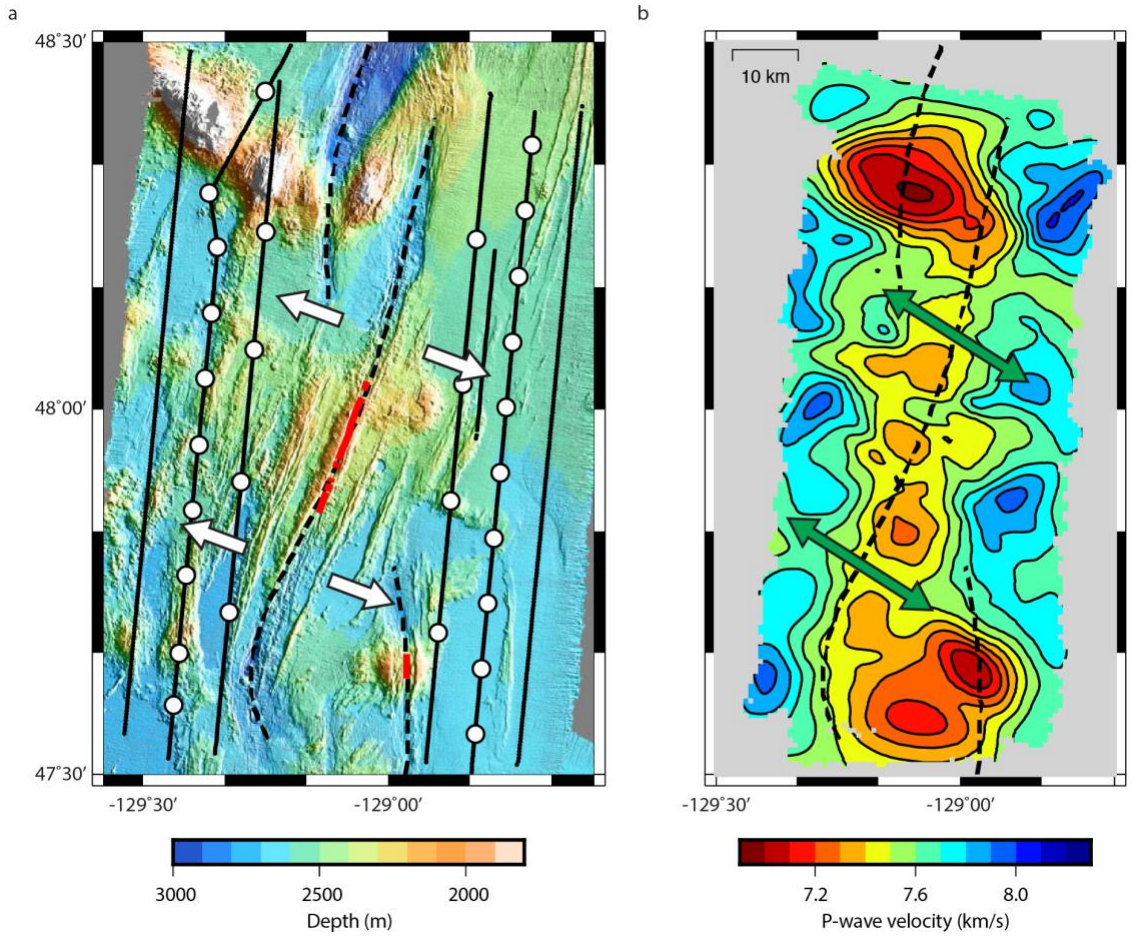

Figure 2. Location and geometry of the ETOMO experiment and tomographic image of the mantle velocity structure. (a) Bathymetric map of the Endeavour Ridge. Black dots and white circles show the location of seismic sources and receivers, respectively (see Appendix A). The white arrows indicate the plate-spreading direction (Gripp & Gordon, 2002). The location of the crustal axial magma lens is shown in red (Carbotte et al., 2006). (b) Tomographic image of the mantle P-wave velocity structure at 7.8 km depth beneath the seafloor; contour interval is 0.1 km/s. Green arrows indicate the azimuth of seismic anisotropy. Dashed lines identify the plate boundary.

Our preferred tomographic solution is shown in Figure 2b; Appendix A section discusses model resolution, sensitivity, and trade-offs. The isotropic component of mantle velocity is anomalously low along the entire length of the Endeavour segment. However, the trend of the mantle low-velocity zone (MLVZ) does not follow the Endeavour ridge

axis, nor is it rotated clockwise with respect the ridge segment (i.e., perpendicular to the fast-axis of mantle anisotropy), but instead connects the OSCs. Remarkably, both the cross-axis width and amplitude of the MLVZ are largest beneath the segment-bounding Cobb and Endeavour OSCs. Beneath the Cobb OSC the MLVZ is ~30 km in diameter, centred west of the eastern spreading limb, and the lowest mantle velocities (~7.1 km/s) are beneath the eastern rift. At the Endeavour OSC, a 30-km-wide MLVZ extends across both spreading limbs with the lowest velocities (~7.1 km/s) concentrated beneath the western rift. By contrast, the MLVZ beneath the main Endeavour ridge, where a nearly continuous crustal axial magma lens has been identified (Carbotte et al., 2006), is a narrower (~15 km), more linear feature characterized by slightly higher velocities (~7.4 km/s). Three local minima punctuate the central MLVZ at intervals of ~15 km. The southern- and northern-most of these minima are located ~5 km off axis.

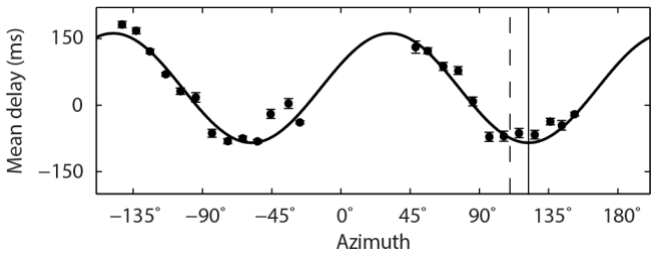

Figure 3. Mean Pn delay times versus azimuth. Delays are calculated relative to an isotropic mantle (7.6 km/s), binned at 10° intervals, and corrected to 40 km range (see Appendix A). Error bars show the 95% confidence interval in the mean delay time as determined by a Student's t-test. The solid line is the best-fit cos2θ-curve. The azimuth of seismic anisotropy is 122° ± 1° (solid vertical line), which is rotated 12° clockwise from the plate-spreading direction (vertical dashed line; Gripp & Gordon, 2002). The anisotropic magnitude is 4.7% ± 0.4%.

3.0 Mantle Flow and Melt Distribution at Endeavour

The anisotropic component of our model constrains the segment-scale geometry of uppermost mantle flow. This is because seismic anisotropy in the mantle is dominated by the lattice-preferred orientation of olivine crystals (Ismaïl & Mainprice, 1998). In response to strain induced by gradients in the mantle flow field, the crystallographic a-axis of olivine (the fast-axis of P-wave propagation) aligns parallel to the direction of

maximum shear (Zhang & Karato, 1995). Because mantle divergence generates large shear strains (Blackman & Kendall, 2002), we infer that the azimuth of seismic anisotropy parallels the mantle divergence direction, which is skewed 12° clockwise from the plate-spreading direction. Furthermore, the observed cos2θ-pattern (Figure 3) is consistent with a two-dimensional flow field and does not suggest segment-scale, three-dimensional flow consistent with diapiric upwelling (Dunn et al., 2000).

The isotropic component of our model constrains the thermal structure and distribution of melt beneath the Endeavour segment. To explain the magnitude of the MLVZ with thermal perturbations alone requires unrealistically large temperature anomalies (see Appendix A). The seismic velocity reduction unaccounted for by a likely thermal anomaly is consistent with <2% partial melt beneath the segment centre and 1 to 5% beneath the OSCs (see Appendix A). Given the seismic wavelength of Pn, the partially molten regions must extend several kilometres beneath the Moho, though the details of melt geometry are not constrained by our data. We infer that the MLVZ defines the segment-scale geometry of the shallow mantle magmatic system.

Our results indicate the greatest volumes of mantle melt are currently beneath the second-order tectonic discontinuities. The observed seismic velocities are consistent with as much as 90 km^3 of melt within the upper 4 km of the mantle beneath each OSC (see Appendix A). In comparison, we estimate up to 40 km^3 of melt is present within the upper 4 km of the mantle beneath the non-overlapping portion of the Endeavour ridge or less than half that present beneath either OSC. Several studies suggest the inferred segment-scale melt distribution is not related to nearby seamount chains (see Appendix A). In contrast to the estimated melt volumes, crustal thickness along the Endeavour

segment, which constrains the time-integrated magma supply, is greatest at the segment centre (Soule et al., 2016; Carbotte et al., 2008). To reconcile the current distribution of mantle melt with the time-averaged supply, we infer that mantle melt is efficiently extracted beneath the segment centre and that greater amounts of melt are stored within the mantle beneath tectonic offsets. Additional evidence supporting this inference is discussed below.

We note that the MLVZ does not align with the Endeavour ridge axis, nor is it perpendicular to the mantle divergence direction as is the case for the fast-spreading EPR (Toomey et al., 2007). Instead, the MLVZ lies sub-parallel to the regional, N-S trend of the northern JdFR, a result consistent with the focusing of shallow mantle melt beneath the youngest and thinnest lithosphere (Sparks & Parmentier, 1991). Indeed, as discussed below, cross- and along-axis variations in thermal structure appear to be the primary factor influencing the segment-scale distribution of magma at both sub-Moho and crustal depths.

4.0 Tectonic Segmentation of Mid-Ocean Ridges

Seismic studies from fast- (Toomey et al., 2007), intermediate- (this study), and slow-spreading (Dunn et al., 2005) centres reveal a remarkable characteristic of the mid-ocean ridge system: A systematic skew between the plate- and mantle-divergence directions, where the magnitude of skew increases as spreading rate decreases (Figure 4). Furthermore, for each region studied, the skew of mantle divergence is in the same direction as, and ahead of, recent changes in the spreading direction (Figure 1). Along both the 9°N EPR and 35°N MAR segments, the mantle flow field is rotated in an anticlockwise sense and the associated Euler poles have progressed anticlockwise over

the last several million years (Pockalny et al., 1997; Sloan & Patriat, 1992). Similarly, we find that mantle flow beneath the Endeavour is skewed clockwise and the Pacific-JdF plate boundary has been reorganizing clockwise over the last ~10 Ma (Wilson, 1988). These observations indicate that sub-ridge mantle dynamics are not solely a passive response to overlying plate motion. On the basis of these results, we assume that current plate-spreading directions are lagging behind a more rapidly evolving asthenospheric flow field, and that this lag increases with decreasing spreading rate (Figure 4).

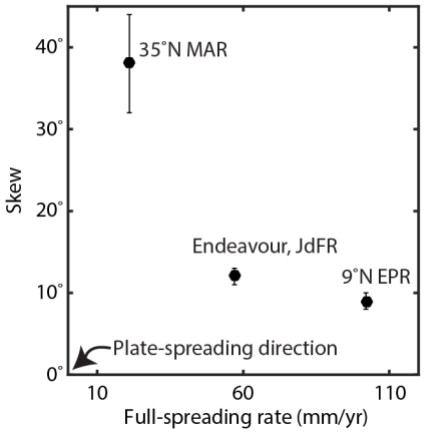

Figure 4. Skew of mantle anisotropy by spreading rate. The magnitude of the skew between mantle anisotropy and the predicted plate-spreading direction (Gripp & Gordon, 2002) is plotted by spreading rate; uncertainties are defined by the standard error in the weighted least-squares fit to Pn travel-time residuals from each experiment. Observations from the EPR and MAR are taken from Toomey et al. (2007) and Dunn et al. (2005), respectively.

We propose that skew between asthenospheric flow and plate motions generates a drag force on the base of oceanic lithosphere that contributes to changes in spreading direction and the formation of second-order tectonic discontinuities. Basal shear stresses may be small, but they can amount to a significant force when integrated over a substantial area (~$10^{14\text{-}16}$ N assuming strain rates of 10^{-15} s^{-1}, asthenosphere viscosity of 10^{19} Pa s, and plate area of $10^{10\text{-}12}$ m^2). In support of this view, shear wave splitting observations made at sites throughout the JdF plate are consistent with a clockwise rotation of asthenospheric flow relative to absolute plate motion (Bodmer et al., 2015). A skewed mantle flow field would generate transtensional stresses at the ridge. We thus suggest that ridge segments and second-order tectonic offsets are analogous to the

formation of transtensional cracks. In a transtensional stress regime, left- or right-stepping offsets will form in right- or left-lateral shear, respectively (Pollard et al., 1982). For numerous second-order discontinuities across a range of spreading rates — including the sections of the EPR, JdFR, and MAR discussed here — the formation and geometry of segment offsets correlate with recent changes in spreading direction (Morgan & Sandwell, 1994). We hypothesize that these changes in spreading direction are in part a response to skew between plate motions and mantle flow and that the work required to reorient transpressive oceanic transform faults limits the rate at which spreading directions can change (Toomey et al., 2007). For a given spreading rate, a range of skew magnitudes may be present depending on the tectonic history and geometry of bounding first-order discontinuities. However, since transform faults occur more frequently along more slowly spreading regions of the mid-ocean ridge system, we predict that the magnitude of skew will, on average, increase with decreasing spreading rate.

5.0 Magmatic Segmentation of Mid-Ocean Ridges

Tomographic imaging of the topmost mantle from fast- and intermediate-spreading ridges reveals a second remarkable characteristic of the mid-ocean ridge system: Second-order tectonic offsets are sites of increased storage of shallow mantle melt over relatively broad areas. At the Endeavour segment both the cross-axis width and magnitude of the MLVZ are greatest beneath the segment-bounding OSCs (Figure 2b). Similarly, tomographic results from the EPR reveal a MLVZ that is both more pronounced and laterally extensive beneath the 9˚03’N OSC (Toomey et al., 2007). These observations cannot be attributed to an increase in magma supply. This is because geophysical studies show that second-order offsets along the EPR (Barth & Mutter, 1996;

Canales et al., 2003) and the JdFR (Soule et al., 2016; Marjanović et al., 2011) are regions of normal or decreased crustal thickness. In addition, isotopic variations in axial basalts from the 9°03'N OSC show no evidence for variations in extents of melting near the discontinuity (Wanless et al., 2012).

We propose a model for the magmatic segmentation of fast- and intermediate-spreading centres based on the hypothesis that the segment-scale characteristics of the shallow mantle and crustal magmatic systems are governed by the pattern of rifting and resulting near-axis thermal structure (Figure 5); the implications of our model for slow-spreading ridges are discussed below. Away from the influence of hot spots, we assume that the production of mantle melt is uniform at the scale of second-order ridge segments (Hooft et al., 2000), including their non-transform discontinuities, and that melt ascends toward the base of young lithosphere, where it is focused by sloping isotherms (Sparks & Parmentier, 1991). In between tectonic offsets — where plate separation is accommodated by a single rift — mantle melts are focused toward a discrete, well-defined plate boundary (Figures 5a-b). Here, magma is more frequently injected into the rift and hydrothermal processes shape a narrow crustal magmatic system (Dunn et al., 2000), the depth of which depends on spreading rate and the efficiency of advective heat removal (Morgan & Chen, 1993). In contrast, near second-order tectonic offsets (Figures 5a, c) the available mantle-derived melts are distributed between overlapping spreading limbs. This dispersal of a fixed amount of heat results in a deeper crustal magmatic system and a broader region of elevated temperatures at both lower crustal and shallow mantle depths. We assert that these conditions result in less efficient delivery of melt to mid-crustal reservoirs and the preferential retention of melt for longer periods of time at

mantle depths. The consequences of longer magma residence times beneath second-order discontinuities are several, including increased magmatic differentiation at higher pressures, decreased crustal thickness beneath tectonic discontinuities, and the generation of a denser crustal unit (Figure 5a; Toomey & Hooft, 2008). Such trends are well documented along the mid-ocean ridge system (Langmuir et al., 1986; Soule et al., 2016; Barth & Mutter, 1996; Canales et al., 2003; Marjanović et al., 2011; Wanless et al., 2012; Toomey & Hooft, 2008; Sinton et al., 1983).

Our model of magmatic segmentation, coupled with the mechanics of OSC propagation, also explains the occurrence of relatively thick, dense crust behind the wake of a propagating discontinuity (Figure 5a; Barth & Mutter, 1996; Canales et al., 2003; Marjanović et al., 2011; Toomey & Hooft, 2008). Previous studies indicate that OSC propagation is not continuous, but occurs in discrete jumps, with the propagating limb rapidly lengthening and curving inward toward the basin while the failing limb is rafted off axis or recedes (Macdonald et al., 1985; Shoberg & Stein, 1994; Cormier et al., 1996). Thus, the advancing limb will tap an additional source of mantle melt, one that has been trapped between overlapping spreading limbs and undergone greater amounts of differentiation at sub-Moho pressures. As a result, relatively thick and dense crust will be generated immediately behind the wake of a propagating OSC (Figure 5a).

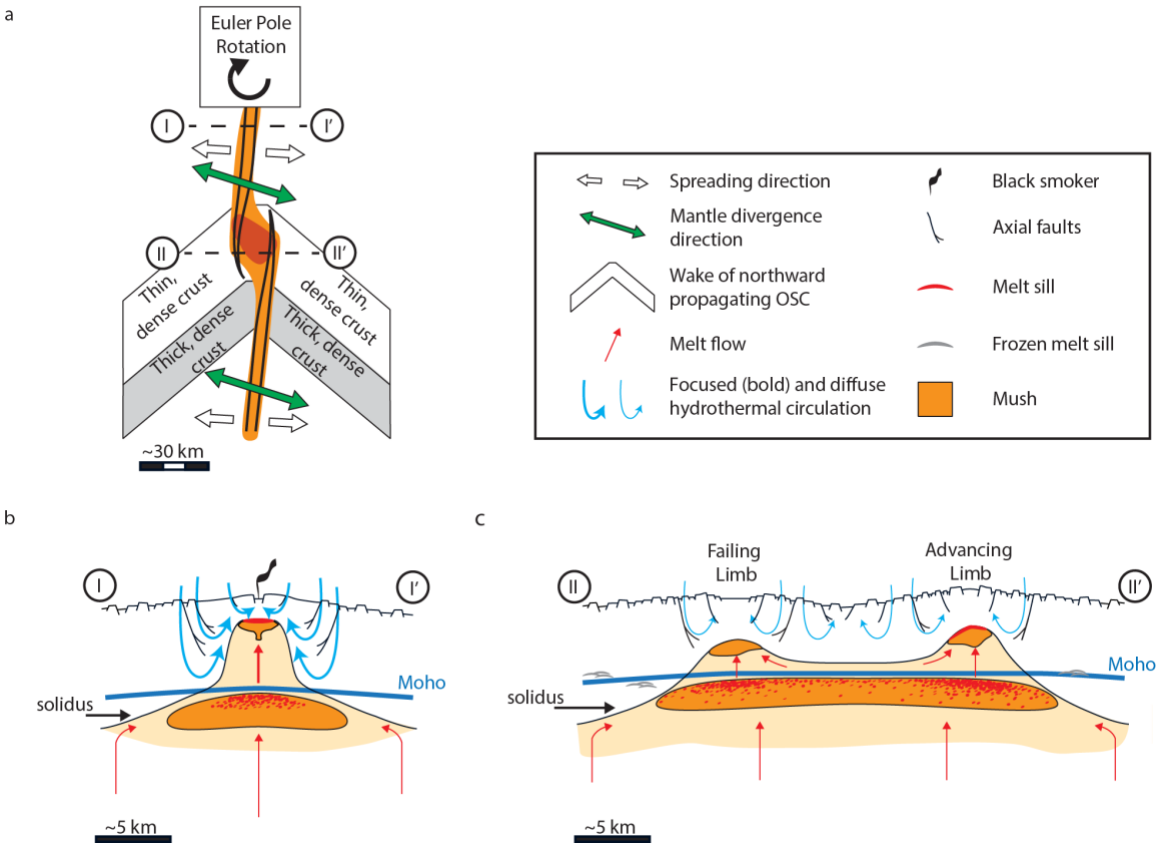

Figure 5. Proposed model of magmatic segmentation for fast- and intermediate spreading ridges. (a) Map view of second-order ridge segments and predictions for the geometry of mantle flow, distribution of shallow mantle melt, and patterns in crustal structure. Dashed lines show the cross-sections in (b) and (c). (b; modified from Toomey et al., 2007)**,** Rise-perpendicular section away from a second-order, tectonic discontinuity. (c) Rise-perpendicular section across a second-order OSC; see text for discussion. Red stippling denotes regions of increased melt fraction. Seafloor relief and thickness of melt sills are exaggerated.

A number of studies are consistent with our assertion that mantle melt is preferentially stored and broadly distributed beneath second-order discontinuities. Seismic imaging of crustal structure along the EPR (Bazin et al., 2003) and Lau Spreading Centre (Dunn et al., 2013) identify anomalously broad axial magmatic systems spanning OSCs, similar to that depicted in Figure 5c. Multi-channel seismic imaging experiments from both the Lau Basin (Collier & Sinha, 1992) and the EPR (Kent et al., 1993) also reveal that widespread crustal melt lenses are characteristic of these OSCs. In contrast, away from tectonic discontinuities crustal magmatic systems are confined to relatively narrow regions centred beneath the plate boundary (Dunn et al., 2000; 2013)

and these systems are capped by relatively narrow axial magma lenses (Figure 5b; Collier & Sinha, 1992; Kent et al., 1993). We attribute the observed increase in the width of crustal magmatic systems near second-order offsets to vertical transport of magma from laterally extensive regions of melt accumulation at shallow mantle depths. The identification of frozen sub-Moho magma lenses found in association with migrating offsets on the JdFR (Nedimović et al., 2005) and the prevalence of Moho-depth melt sills near the 9°03'N OSC on the EPR (Crawford & Webb, 2002) further supports our interpretation that second-order discontinuities are sites of enhanced mantle melt storage. The maximum depth extent of the inferred region of melt storage must extend for several kilometres given the seismic wavelength of Pn phases. Deeper mantle imaging (10-30 km sub-Moho) of multiple non-transform discontinuities along the Lau Spreading Centre reveals that the melt production region is uninterrupted across multiple ridge offsets (Zha et al., 2014). Assuming these results are characteristic of other spreading centres, we conclude that the retention of mantle melt beneath second-order offsets occurs within the top few kilometres of the mantle.

For slow-spreading ridges our model of magmatic segmentation also predicts that the distribution of shallow mantle melt is influenced by the geometry of tectonic segmentation. As spreading rate decreases the morphologic expression of second-order offsets changes from OSCs to oblique shear zones or non-transform offsets (Figure 1) and the near-axis thermal structure will differ significantly. For example, the increased age offset at the ends of slow-spreading segments results in a thicker axial lithosphere and significant variations in the predicted along-axis mantle temperature (Neumann & Forsyth, 1993). Thickened axial lithosphere will also inhibit the extraction of mantle

melts (Cannat, 1996) and promote the migration of melt towards segment centres where the lithosphere is predicted to be thinnest (Magde & Sparks, 1997). Consequently, along-axis variations in crustal thickness are pronounced with the thickest crust located mid-segment (Dunn et al., 2005; Hooft et al., 2000).

Between second-order tectonic discontinuities the results of seismic studies show that as the spreading rate decreases the distribution of shallow mantle melt is increasingly influenced by the segment-scale thermal structure of newly formed lithosphere. At the fast-spreading EPR, where cross- and along-axis variations in thermal structure are least pronounced for the global ridge system, both the azimuth of seismic anisotropy relative to the spreading direction and the trend of the MLVZ with respect to the rise axis are skewed coherently by similar amounts (Toomey et al., 2007). Furthermore, centres of mantle melt delivery are spaced at intervals of ~25 km (Toomey et al., 2007) and frequently occur midway between volcanic or third-order discontinuities (Macdonald et al., 1988; Langmuir et al., 1986; Toomey et al., 2007; White et al., 2002). At the EPR, the cross-axis offset between a centre of mantle melt delivery and the rise axis also correlates with the intensity of rise crest volcanic, hydrothermal, and tectonic activity (Toomey et al., 2007) and the distal ends of third-order segments may be associated with a decrease in the efficiency of mantle melt extraction (Aghaei et al., 2014).

In contrast, a coherent skew of both seismic anisotropy and the MLVZ — and by inference the direction of mantle divergence and the segment-scale shallow mantle magmatic system — is not present beneath either the JdFR or the MAR (Dunn et al., 2005). Instead, in each instance the mantle divergence direction is skewed with respect to the plate-spreading direction, but the segment-scale trend of the MLVZ is either sub-

parallel to that of the youngest and thinnest lithosphere (JdFR) or preferentially localized beneath segment centres where lithosphere is also predicted to be thinnest (MAR; Dunn et al., 2005; Hooft et al., 2000; Cannat, 1996). These results suggest that three-dimensional, segment-scale variations in the thickness of near ridge lithosphere governs the distribution of shallow mantle melt. We note that third-order segmentation is poorly defined at the Endeavour segment (Karsten et al., 1990) and not identifiable along the MAR (Carbotte et al., 2015). We speculate that only in regions where along- and cross-axis variations in near ridge lithospheric structure are minimal (e.g., EPR), will there be a relation between centres of mantle magma supply and third-order segmentation.

Detailed geophysical studies of individual spreading segments support a new view of the mid-ocean ridge system in which skewed asthenospheric flow contributes to plate boundary reorganization. The resulting changes in relative plate motion are accommodated through the formation and migration of tectonic offsets. These tectonic discontinuities in turn perturb the axial thermal structure thus defining shallow mantle and crustal magmatic segmentation. This view stands in contrast to the long-standing hypothesis that mid-ocean ridge morphology reflects variations in mantle magma supply from a passively driven asthenosphere. Our results have several implications for ridge dynamics. At the scale of individual spreading segments, seismic images of the uppermost mantle indicate crustal production is not solely a function of melt availability. Rather, the dynamics of lithospheric rifting ultimately control the transfer of mass between Earth's interior and the seafloor. On the global scale, our results indicate that tectonic segmentation across spreading rates shares a common origin related to evolving patterns of asthenospheric flow. In this view, second-order tectonic discontinuities result

from the transmission of viscous stresses from the asthenosphere to the lithosphere. We speculate that the variability in the lengths of second-order ridge segments and the geometry of their bounding offsets may reflect changes in the strength of axial lithosphere as a function of spreading rate. Furthermore, we attribute the origin of skewed asthenospheric flow beneath ridges to the global mantle flow field, which is largely driven by sinking of oceanic lithosphere at subduction zones.

6.0 Bridge

Chapter II presented evidence for a systematic misalignment between the direction of plate and mantle divergence that may exist globally beneath the mid-ocean ridge system. Observations from fast-, intermediate-, and slow-spreading ridge segments indicate that the orientation of mantle flow is rotated ahead of recent changes in plate motion and is in effect contributing to changes plate velocity. Models of mantle upwelling and the development of crystal preferred orientation in olivine predict that mantle anisotropy created beneath the ridge is frozen into the lithosphere as material is transported off axis thus preserving the paleo-geometry of mantle flow. In Chapter III, I test whether the clockwise rotation in mantle flow inferred beneath the northern JdF ridge has persisted over the last ~9 Myr by measuring the average anisotropic fabric of the JdF plate interior. During this interval, the JdF plate motion has been rotating clockwise in a hot-spot reference frame. The results prove inconclusive. I find evidence that, contrary to model predictions, shallow mantle anisotropy reorganizes off-axis to more closely align with absolute plate motion before freezing into the lithosphere. The pattern of flow at the paleo-spreading center is obscured.

CHAPTER III

SHALLOW MANTLE ANISOTROPY BENEATH THE JUAN DE FUCA PLATE

From VanderBeek, B. P., & Toomey, D. R. (2017). Shallow mantle anisotropy beneath the Juan de Fuca plate. *Geophysical Research Letters*, *44*(22).

1.0 Introduction

The time-integrated deformation of the upper oceanic mantle is recorded by the lattice preferred orientation (LPO) of olivine crystals. Olivine LPO produces a directional dependence to seismic wave speeds that is used to infer patterns in mantle flow (Nicolas & Christensen, 1987; Becker et al., 2006; Karato et al., 2008). The seismic anisotropic fabric of the oceanic mantle lithosphere has long been interpreted as the frozen-in signal of passive mantle upwelling beneath mid-ocean ridges (Hess, 1964; Francis, 1969; Morris et al., 1969; Nicolas & Violette, 1982; Gaherty et al., 2004; Song & Kim, 2012; Becker et al., 2014; Lin et al., 2016). In this view, the divergence of mantle material beneath the ridge axis aligns the fast propagation direction of olivine in the direction of spreading. This alignment is presumed to be frozen into the lithosphere with little subsequent deformation off-axis. However, significant misalignment between the orientation of frozen-in lithospheric anisotropy and the direction of spreading (hereafter referred to as 'skew') exists globally (e.g. Becker et al., 2014). We present seismic evidence that skewed mantle anisotropic fabric exists within ~10 km of the Mohorovičić discontinuity (Moho) beneath the Juan de Fuca (JdF) plate. We suggest that deformation at shallow mantle depths continues away from the plate boundary and acts to reorient olivine LPO to more closely align with the ambient mantle flow direction. This result has

implications for the development of mineral fabrics and interpretation of seismic anisotropy in the oceanic lithosphere.

2.0 Data and Methods

We use the arrivals times of Pn phases (seismic energy scattered through the lithosphere) generated by regional earthquakes to image uppermost mantle anisotropy at the scale of the JdF plate. Seismic data are recorded on the vertical channels of the year-three deployment of Cascadia Initiative ocean bottom seismometers (OBSs) and a complementary array of OBSs located along the Blanco Transform Fault (Figure 1; Toomey et al., 2014). The year-three array provides complete coverage of the JdF plate as well as the necessary coverage of the Blanco Transform region to accurately relocate Blanco events. Our data set comprises 757 Pn arrival times from 35 Blanco earthquakes (Figure 1) with reported magnitudes between 2.8 and 5.1. All seismic records were acquired through the Incorporated Research Institutions for Seismology (IRIS).

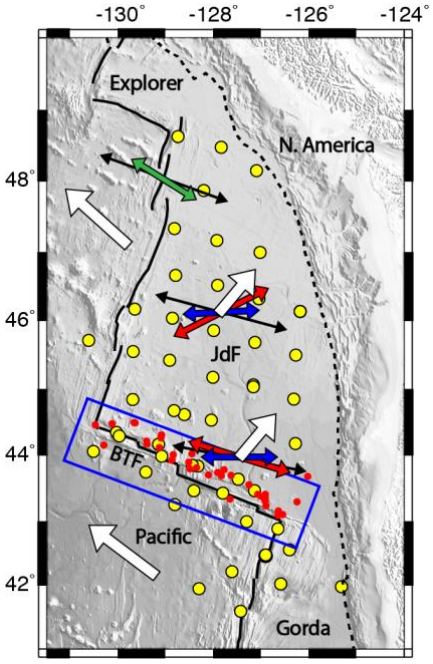

Figure 1. Bathymetric map of the study area with the locations of OBSs (yellow circles) and catalogued earthquake locations (red circles) used in our analysis. Blue arrows show the orientation of Pn anisotropy beneath the JdF plate interior and in the Blanco Transform Fault region (BTF; outlined by blue box) measured in this study. The orientation of mantle anisotropy from Pn travel-times measured beneath the northern JdF Ridge (green arrow; VanderBeek et al., 2016) and from SKS splits measured beneath the plate interior and the BTF region (red arrows; Bodmer et al., 2015) are also shown. White and black arrows parallel Pacific and JdF APM and JdF-Pacific RPM, respectively. The solid and dashed black lines identify the JdF Ridge-transform system and the Cascadia subduction zone, respectively.

The Pn waveforms (Figure 2a-b) are characterized by high frequency content (>10 Hz) and a gradual increase in amplitude over ~1 s followed by a long and complex coda that decays slowly after many 10's of seconds (Shito et al., 2013). The emergent nature of the Pn phase makes accurately and consistently picking onset times challenging. Therefore, we employ an automated picking method like that of Shintaku et al. (2014) in which a linear profile is fit to the smoothed logarithm of the bandpass filtered (5-10 Hz) seismograms. This method takes advantage of the prominent ramp-up in amplitude observed at the arrival of Pn (Figure 2c-d). The onset of this ramp is taken as a proxy for the true first arrival time. Our picking procedure is illustrated in Figure 2 and described in detail in Appendix B, Text S1. All data are visually inspected, checked for picking errors, and prescribed user-defined relative uncertainties.

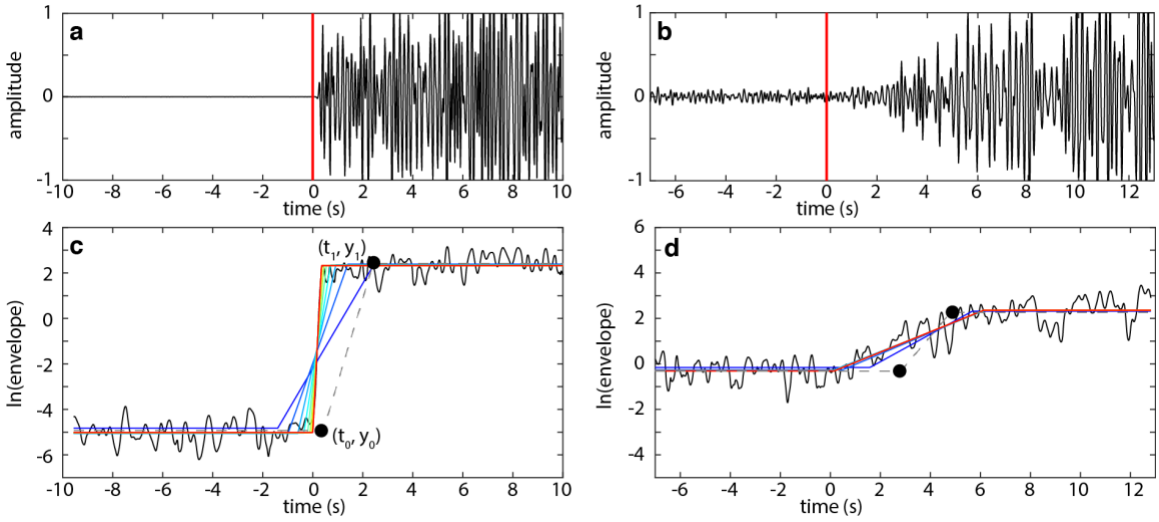

Figure 2. (a) Impulsive and (b) emergent Pn waveforms recorded on the vertical channel of Cascadia Initiative OBSs. Both arrivals originated from the same earthquake and propagate at similar azimuths. The impulsive arrival was recorded at a range of 102 km while the emergent waveform was recorded at a range of 221 km. The red bars fall on the auto-picked arrival time which is aligned on 0 s. In (c) and (d) we plot the smoothed natural log of the above seismograms. The Pn arrival time is identified by fitting a linear profile as defined by the parameters t_0, y_0, t_1, and y_1 identified in (c). The result from the first iteration of our auto-picker is shown by the blue line while the final (tenth) iteration is shown in red. The dashed grey line identifies the initial linear profile. See Appendix B, Text S1 for further discussion.

We use Pn arrival times to perform a weighted least-squares inversion for earthquake epicentral parameters and plate-scale mantle anisotropic velocity. For the

forward problem, ray theoretical travel-times are predicted analytically assuming a constant source depth and a two-layer velocity model. Based on the centroid depth distributions presented by Braunmiller and Nábělek (2008), we prescribe all earthquakes a depth of 6 km beneath the seafloor. We assume a constant 6 km thick crust with a velocity of 6 km/s. These values are representative of the mean JdF plate crustal structure presented by Horning et al. (2016). Predicted travel-times are adjusted for sediment thickness variations which can be pronounced (upwards of 1000 m; Divins, 2003; Ruan et al., 2014; Bell et al., 2015). Where available, the sediment thickness beneath each station is taken from the surface wave study of Bell et al. (2015), otherwise values are interpolated from the sediment thickness map of Divins (2003). The travel-time through the sediment column is calculated assuming a vertical ray path. The P-wave velocity profile is derived from the measured shear velocity structure of Cascadia sediments (Ruan et al., 2014) and P-to-S-wave speed ratios for marine sediments (Hamilton, 1979). We also include damped station static terms in our inversion for epicentral parameters such that adjustments to the *a priori* corrections are allowed but large deviations from the initial corrections are penalized.

Upper mantle azimuthal anisotropy is well-described by a periodic function consisting of 2θ and 4θ terms (Backus, 1965; Morris et al., 1969; Becker, 2006). However, in our analysis of Pn anisotropy we find that the 4θ terms are not required to fit the data. Therefore, in our estimates of mantle anisotropy we chose to fit a function of the form

$$V = \alpha_0 + \alpha_1 \cos(2\theta) + \alpha_2 \sin(2\theta) \qquad (1)$$

to azimuthal variations in mantle velocities derived from Pn travel-time residuals. In Equation 1 'θ' is the source-receiver azimuth, 'α_0' is the mean mantle velocity, and 'α_1' and 'α_2' control the magnitude and orientation of anisotropy. To minimize the effects of isotropic heterogeneity on our estimate of mantle anisotropy, we bin the mantle velocities as a function of azimuth at 20° intervals. Errors in the mean velocity for each bin are estimated using a Student's t-test with a 95% confidence interval and are used to weight the least-squares fit of Equation 1 to the data.

3.0 Results

In our investigation of upper mantle anisotropy, we allow for two anisotropic domains (see Appendix B, Text S2); (1) the Blanco transform region consisting of all Pn arrivals recorded by stations located within 180 km of Blanco events (Appendix B, Figure S1a) and (2) the plate interior domain consisting of all Pn arrivals with ray paths that are confined to the JdF plate (Appendix B, Figure S1b). We jointly invert for the epicentral and anisotropic parameters using the Blanco domain dataset. Our preferred relocation solution is shown in Figure 3. We find that the cataloged earthquake locations are systematically shifted northeast of the Blanco Transform Fault by ~30 km. These results agree with those from the more detailed seismicity study of Braunmiller and Nábělek (2008). The revised locations correlate well with tectonically active segments of the Blanco Transform Fault (Embly & Wilson, 1992). The Blanco dataset is best characterized by 4.8% ± 0.2% velocity anisotropy with a fast-axis azimuth of 90º ± 6º and mean mantle velocity of 7.85 km/s ± 0.03 km/s. Using our preferred relocation solution (Figure 3), azimuthal variations in mantle velocities derived from the JdF plate interior dataset show a clear cos2θ-pattern with a magnitude of 4.6% ± 0.4% and fast-

axis azimuth of 87º ± 3º (Figure 4a). The mean mantle velocity is 7.85 km/s ± 0.02 km/s. The errors reported reflect the 1σ-uncertainty as determined via grid-search (Appendix B, Figure S2). The weighted root mean square of the travel-time residuals for the Blanco and plate interior datasets are 195 ms and 416 ms (variance reduction of 99.8% and 61.2% with respect to the starting models), respectively (Appendix B, Text S3; Figures S3). For comparison, passive source Pn tomography studies (e.g., Hearn, 1991; Pei et al., 2007) typically fit travel-time data to >700 ms, albeit such studies are on a larger scale and conducted in tectonically more complex continental regions. See Appendix B, Text S3 for further discussion of the models. As discussed in Appendix B, Text S3, our preferred solution is stable with respect to our choice of inversion parameters, the crustal velocity model, sediment thickness variations, source depth, station statics (Appendix B, Figure S4), and potential influence of 2D velocity heterogeneity (Appendix B, Figure S5) caused by variations in mantle temperature (Karato, 1993).

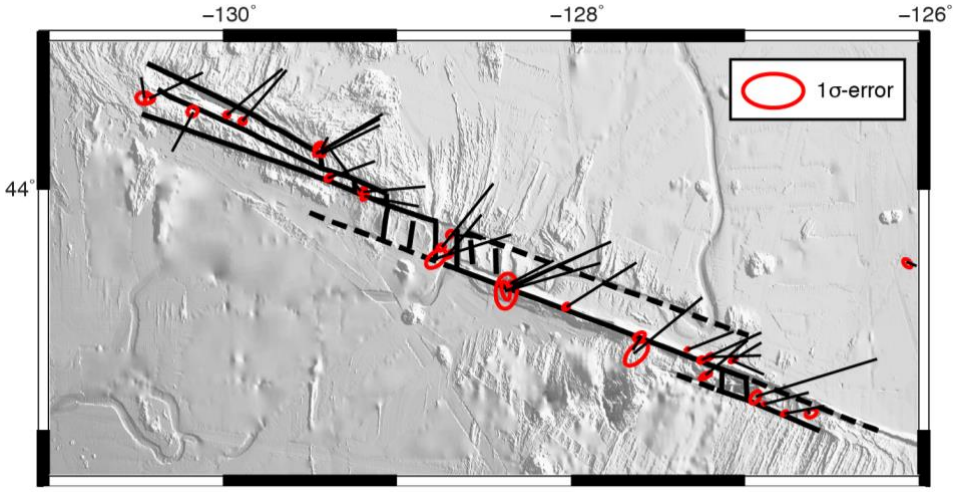

Figure 3. Map of the relocated Blanco events. Red ellipses outline the 1σ uncertainty contour in the event positions and are determined via a grid-search over perturbations to the preferred epicenter locations using an F-test (see Appendix B, Text S3). Black quivers point back to the initial catalogued earthquake locations. Solid black lines identify currently active lengths of the plate boundary and the dashed black line identifies inactive sections of the Blanco Transform Fault (Embley & Wilson, 1992).

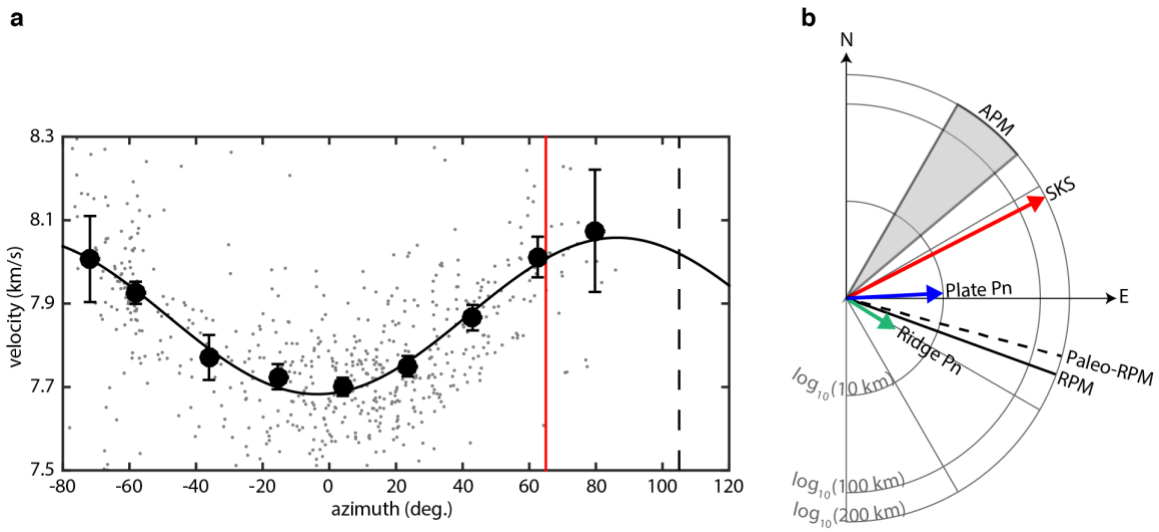

Figure 4. (a) Mantle velocities estimated from the plate interior travel-times plotted as a function of ray azimuth. Mantle velocities are binned at 20° intervals (grey points are non-binned measurements). The error bars show the 95% confidence interval in each bin as determined by a Student's t-test. The solid line is the best-fit $\cos 2\theta$-curve. The best-fit azimuth of seismic anisotropy is 87° ± 3°. The mean mantle velocity and percent anisotropy is 7.85 km/s ± 0.05 km/s and 4.7% ± 0.2%, respectively. Uncertainties are estimated via a grid-search (see Appendix B, Text S3). The dashed black and red lines show the mean paleo-spreading direction (Riddihough, 1984) and the plate interior fast SKS polarization direction (Bodmer et al., 2015), respectively. (b) The fast-axis orientation of mantle anisotropy measured beneath the northern JdF Ridge (green arrow; VanderBeek et al., 2016) and the JdF plate interior from Pn travel-times (blue arrow) and SKS splits (red arrow; Bodmer et al., 2015). The length of each arrow correlates with the approximate depth sensitivity of each measurement (log scale). The grey region encompasses the range in orientations of JdF APM over the last ~7 Myr in a hotspot reference frame (Riddihough, 1984). Solid and dashed black lines show the present and past orientations of Pacific-JdF RPM, respectively.

Remarkably, neither the Blanco nor the plate interior data subsets record a mantle anisotropic fabric that aligns with the mean paleo-spreading direction (Riddihough, 1984; Wilson, 1988) sampled (101º and 105º, respectively; see Appendix B, Text S4). Instead, the fast propagation directions are skewed 11º (Blanco domain) and 18º (plate interior domain) counterclockwise from past Pacific-JdF relative plate motion (RPM). Given the frequency (5-10Hz) and range (~200 km) of the Pn arrivals used in this study, the anisotropic signals recovered reflect mantle structure shallower than ~10 km beneath the Moho (Zhang et al., 2007).

4.0 Discussion

We synthesize our plate-average Pn anisotropy measurement with previous studies of seismic anisotropy beneath the JdF Ridge (VanderBeek et al., 2016) and across the JdF plate (Bodmer et al., 2015; Martin-Short et al., 2015). These complementary observations allow us to infer possible scenarios for the depth- and age-dependence of mantle anisotropy. Using Pn arrival times from an active source seismic experiment located on the northern JdF Ridge, VanderBeek et al. (2016) mapped the topmost mantle (<4 km beneath the Moho) seismic anisotropic fabric at young seafloor ages (0 to ~770 kyr). They found 4.7% ± 0.4% mantle anisotropy with a fast propagation direction rotated 12º ± 1º clockwise from JdF-Pacific RPM (Figure 1, 4b). Analysis of SKS splits (Bodmer et al., 2015; Martin-Short et al., 2015) show that the depth-averaged (seafloor to ~100-200 km) orientation of mantle anisotropy abruptly transitions from a poorly-defined pattern beneath the spreading center to a coherent orientation that is sub-parallel to JdF absolute plate motion (APM) within 50-100 km of the plate boundary (Figure 1, 4b). Notably, Bodmer et al. (2015) find that SKS splitting orientations beneath the plate interior are systematically rotated ~25º clockwise from APM (Figure 4b).

Our plate-average Pn anisotropy measurement records a fabric that strikes between these observations and trends counterclockwise to the paleo-spreading direction, toward JdF APM (Figure 4b). This plate-averaged anisotropy reflects mantle structure at depths up to ~2x greater than the sensitivity of the ridge Pn observation and at considerably shallower depths than the sensitivity of SKS splits (Figure 4b). Following from these observations, we infer that mantle anisotropic fabrics created within ~10 km of the Moho beneath the ridge realign toward the SKS fast polarization direction as they

are transported off-axis. Alternatively, the counterclockwise rotation of plate-averaged Pn anisotropy with respect to JdF-Pacific RPM could have been generated by deformation beneath the ridge without further off-axis modification. However, this suggestion is inconsistent with the JdF Ridge measurement which exhibits the opposite sense of rotation (Figure 4b; VanderBeek et al., 2016). Therefore, we favor the former interpretation that topmost mantle anisotropy reorganizes before being frozen into the lithosphere.

Our preferred interpretation is consistent with the mechanisms of deformation thought to be active in the oceanic mantle. It is well established that seismic anisotropy in the oceanic mantle results from olivine LPO (Hess, 1964; Nicolas & Violette, 1982; Nicolas & Christensen, 1987; Zhang & Karato, 1995; Becker et al., 2006; Karato et al., 2008). At lithospheric depths, this fabric is typically attributed to the frozen-in signal of corner flow at the paleo-spreading center (Francis, 1969; Morris et al., 1969; Nicolas & Violette, 1982; Gaherty et al., 2004; Song & Kim, 2012; Becker et al., 2014; Lin et al., 2016), where the divergence of mantle material is expected to align the seismically fast-axis of P-wave propagation in olivine (the crystallographic a-axis) in the direction of spreading (Ribe, 1989; Blackman & Kendall, 2002). Away from a spreading center, upper mantle deformation is thought to be dominated by the differential motion between the plate and deeper mantle. This is supported by numerical modeling (Tommasi et al., 1998; Rümpker et al. 1999), SKS splitting observations (Wolfe & Solomon 1998; Bodmer et al., 2015; Martin-Short et al., 2015), and surface wave tomography studies (Becker et al., 2014 and references therein) that show that the fast polarization directions of seismic waves align sub-parallel to predicted APMs. At some depth and distance from

the ridge, the mantle flow field, and consequently the anisotropic fabric, should transition between a deformational regime dominated by RPM near a spreading center to one dominated by APM beneath older oceanic lithosphere. We suggest that the plate-averaged Pn anisotropy signal records the occurrence of this transition within the topmost mantle beneath the JdF plate.

Our interpretation implies that topmost mantle anisotropy is influenced by both the paleo-RPM at the spreading center and the paleo-APM of the plate to which the mantle material is accreted. This requires that gradients in the mantle flow field exist at shallow depths as the plate ages such that olivine LPO continues to evolve. The half-space cooling model predicts that the upper 10 km of the mantle will be incorporated into the lithosphere between ~0.5 Myr and ~2.5 Myr. If we assume that deformation due to the motion of the JdF plate (N40ºE at 19 km/Myr; Gripp & Gordon, 2002) is accommodated via simple shear that is evenly distributed over a 100 km-thick asthenospheric channel, then mantle within 10 km of the Moho will have accumulated between 0.10 and 0.47 strain before being frozen into the lithosphere. If deformation is more concentrated toward the top of the asthenosphere, the accumulated strain would be greater.

Our estimate of off-axis strain accumulation is appreciable in comparison to strains required for olivine fabric development. Field (Warren et al., 2008), experimental (Boneh & Skemer, 2014), and numerical (Boneh et al., 2015) studies show that well-defined olivine LPO may reorganize at strains < ~1 when pre-existing fabrics are exposed to a new deformational regime (e.g. a change from RPM- to APM-influenced deformation as discussed here). Additionally, the coherent alignment of SKS splits

subparallel to JdF APM within 50-100 km of the ridge (Bodmer et al., 2015) suggest that strain accumulation in the upper mantle is sufficient to create seismically detectable fabrics within 1.8-3.8 Myr (assuming a half-spreading rate of 28 km/Myr; Gripp & Gordon, 2002). Thus, it seems plausible that partial realignment of topmost mantle mineral fabrics may occur before this material is incorporated into the lithosphere. In general, for ridges migrating obliquely to their spreading direction, we may expect seismic anisotropy in older oceanic lithosphere to rarely align with paleo-spreading directions.

Seismic anisotropy measurements in the oceanic lithosphere away from spreading centers yields many observations of skew between the seismically fast propagation and paleo-spreading directions (Morris et al., 1969; Raitt et al., 1969; Shearer & Orcutt 1986; Shintaku et al., 2014; Takeo et al., 2016). While the magnitude of skew observed in these studies is typically >10° and exceeds the measurement error, its significance is not always discussed. Larger scale lithospheric imaging (i.e. averaged over the upper 50 km of the mantle) from global surface wave tomography studies reveals that the magnitude of skew in the oceans is on average 25° (Becker et al., 2014 and references therein). Furthermore, the degree of skew varies geographically and correlates negatively with spreading rate (Becker et al., 2014). Such non-random variations in the misfit between paleo-spreading orientations and seismic anisotropic structure likely hold geodynamic significance. We infer that the globally observed patterns in skew may be related to the misalignment between spreading directions and absolute plate velocities, which vary in both time and space (Williams et al., 2016). Comparison of shallow mantle anisotropy

measurements with paleo-spreading directions and paleo-APM models could provide a first-order test of this hypothesis.

With a magnitude of 4.6%, the percent anisotropy beneath the JdF plate falls between values characteristic of slow- (3-4%) and fast-spreading (6-7%) environments (Gaherty et al., 2004; Toomey et al., 2007; Song & Kim, 2012; Shintaku et al., 2014; Takeo et al., 2016). We speculate that the positive correlation between spreading rate and percent mantle anisotropy may be related to the partial off-axis realignment of olivine LPO. Recent numerical (Boneh et al., 2015) and experimental (Boneh & Skemer, 2014) studies demonstrate that when pre-existing olivine fabrics begin to reorganize (i.e. strains < 1) due to a change in deformation geometry, the resulting fabric may experience transient states characterized by weaker mineral alignment. Therefore, if olivine LPO in the uppermost mantle begins to realign toward APM off-axis but cooling acts to limit the total strain accumulation, then we expect that less vertically coherent fabrics and weaker azimuthal anisotropy may result as spreading rate decreases. This mechanism is distinct from, but not mutually exclusive to, the hypothesis that the dip of olivine a-axes from horizontal control the magnitude of anisotropy as a function of spreading rate (e.g., Ribe, 1989; Gaherty et al., 2004; Song & Kim, 2012). We note that the work of Boneh and Skemer (2014) and Boneh et al. (2015) mainly explores deformation under axial compression rather than simple shear and different geometries of deformation may yield a different textural evolution. Further studies of oceanic lithosphere anisotropy, the influence of deformation history on olivine LPO development, and the effects of ridge migration in three-dimensions will be required to better understand the spreading rate and age dependence of seismic anisotropy.

Unlike the Pn anisotropic structure beneath the plate interior, the clockwise skew of SKS splits with respect to JdF APM (Bodmer et al., 2015) and of near-ridge Pn anisotropy (VanderBeek et al., 2016) with respect to JdF-Pacific RPM cannot be explained through plate motions alone. In both locations, the seismically inferred directions of mantle flow are rotated ahead of recent clockwise changes in JdF plate velocity (Figure 4b; Riddihough, 1984; Wilson, 1988). One explanation is that the present-day JdF plate motion is lagging behind a more rapidly evolving mantle flow field; see VanderBeek et al. (2016) for discussion. In this case, flow in the mantle may actively be driving changes in plate velocity (Toomey et al., 2007; VanderBeek et al., 2016). This situation may not be unique to Cascadia. There is emerging evidence that skewed mantle seismic anisotropy patterns are a common phenomenon within the oceanic mantle (Dunn et al., 2005; Toomey et al., 2007; VanderBeek et al., 2016; Lin et al., 2016). It remains to be understood to what extent mantle flow actively drives, as opposed to passively resists, overlying tectonic processes.

5.0 Conclusion

It is often assumed that seismic anisotropy in the topmost oceanic mantle reflects the upwelling and divergence of mantle material beneath the ridge axis with little subsequent deformation as the plate ages. However, our observations of Pn anisotropy beneath the JdF plate suggest that mantle deformation within ~10 km of the Moho may persist away from the spreading center causing olivine LPO to align from RPM toward APM. Thus, Pn anisotropy measurements may record both paleo-RPM and paleo-APM. The extent to which the uppermost mantle anisotropic fabric realigns toward APM will largely depend on the rheologic evolution of the upper mantle with time. Therefore,

measurements of Pn anisotropy may provide a useful constraint on the development of mineral fabrics and rheologic properties of the uppermost mantle in future geodynamic models.

6.0 Bridge

Chapter III investigated the anisotropic structure of the JdF plate interior but did not resolve spatial variations in mantle structure. In Chapter IV, I extend the tomographic imaging method used in Chapter II to include the inversion of local earthquake arrival times for hypocentral parameters and velocity heterogeneity. The method is used to study the temporal evolution of the JdF plate and fragmenting Gorda plate. The importance of conductive cooling versus mantle alteration by fracturing and hydration in controlling plate velocities is discussed.

CHAPTER IV

PN TOMOGRAPHY OF THE JUAN DE FUCA AND GORDA PLATES: IMPLICATIONS FOR MANTLE DEFORMATION AND HYDRATION IN THE OCEANIC LITHOSHPERE

This chapter is in preparation for publication with Douglas R. Toomey. I performed all the data analysis and wrote the text. Douglas R. Toomey provided input on my interpretation of the results and provided edits on my initial draft of this chapter.

1.0 Introduction

Water is recycled back into Earth's mantle primarily along the global subduction system where it is released from the sinking lithosphere through a series of dehydration reactions (e.g., Faccenda, 2014). Owing to the large water storage capacity and stability of hydrated mantle phases (most notably serpentine), the mantle lithosphere is potentially the largest (by volume) water reservoir for subducted fluids and a primary source for fluid delivery to sub-arc depths (Hacker et al. 2003a; Faccenda, 2014; Abers et al., 2017). Mantle-hosted fluids expelled from the descending plate may contribute to the hydration of the mantle wedge thus influencing the seismic behavior of the plate interface (e.g., Peacock & Hyndman, 1999) and the production of melts that supply arc volcanism (van Keken et al., 2004; Walowski et al., 2015). Fluid release from subducting slabs is also implicated in the generation of intraslab earthquakes (Hacker et al., 2003b; Korenaga, 2017). Despite the significance of water storage in oceanic slabs to a number of geodynamic processes, the volume of water in the mantle remains poorly constrained with estimates ranging from dry to 4 wt. % (Faccenda, 2014; Canales et al., 2017). Even less is known about the spatial and temporal variations in plate hydration and the

relationship of such heterogeneity to arc-parallel changes in tectonic and magmatic processes. This is in part due to a lack of seafloor instrumentation. Constraints on the physical state of oceanic lithosphere come primarily from 2D reflection/refraction profiles (e.g., Lizarralde et al., 2004; Shillington et al., 2015; Horning et al., 2016; Canales et al., 2017) and a small number of 3D seismic deployments over geographically limited areas (e.g., Dunn et al., 2005; Toomey et al., 2007; VanderBeek et al., 2016). Available observations suggest that the hydration state of the oceanic plate prior to subduction is highly heterogeneous and is shaped by its tectonic history (Horning et al., 2016; Paulatto et al., 2017; Han et al., 2018). The Cascadia Intiative (CI) experiment (Toomey et al., 2014; Figure 1a) provides a unique opportunity to study the evolution of an entire oceanic plate from accretion to subduction. Here we use the arrival times of local earthquake P-waves guided through the mantle lithosphere (Pn phase) and recorded by CI seismometers to investigate the thermal evolution and physical properties of the uppermost mantle offshore Cascadia.

The Cascadia subduction system is the archetype of a warm-slab subduction zone. Prior to subduction, the plate remains <10 Myr old which has lead to the inference of a largely dry lithosphere particularly at sub-Moho depths where elevated temperatures limit the depth extent of brittle deformation. Indeed, recent estimates of JdF mantle hydration from 2D refraction imaging indicate less than 0.25 wt% H2O within the uppermost 1 km of mantle (Horning et al., 2016; Canales et al., 2017). A relatively dry subducting slab is also consistent with a general lack of deep intraslab seismicity (McCrory et al., 2012) and eruption of dry arc magmas (Ruscitto et al., 2010; Walowski et al., 2015). However, two sources for locally enhanced water storage have been recognized with potential

implications for seismicity and volcanism in Cascadia. These are the V-shaped propagator wakes that extend across the JdF plate and the pervasive faulting within the Gorda Deformation Zone (GDZ; Figure 1). The propagator wakes are more heavily fractured regions of seafloor formed between non-transform offsets along the mid-ocean ridge (Wilson et al., 1984). As heavily tectonized features, they may provide a greater density of pathways for fluid circulation resulting in local hydration anomalies that may influence subduction zone procsses (Han et al., 2016; Horning et al., 2016; Han et al., 2018). Abundant seismicity and deformed seafloor magnetic and basement lineations (Figure 1) has lead to the speculation that the GDZ may also be a lithospheric hydration anomaly (Nedimović et al., 2009; Walowski et al., 2015; Canales et al., 2017). Extensive hydration of the Gorda lithosphere could explain the compositions of southern Cascade arc magmas, which Walowiski et al. (2015) suggests are sourced from slab melting assisted by a wet (2 wt. % H_2O) slab mantle.

In Cascadia, available constraints on the physical properties of the oceanic mantle lithosphere are spatially limited and exist only for the JdF plate (e.g., Horning et al., 2016; Canales et al., 2017). Thus, it is unclear whether propagator wakes represent plate-wide hydration features and how deformation of the young Gorda plate manifests at sub-Moho depths. To address these issues, we present images of P-wave velocity of the mantle lithosphere offshore Cascadia. Our seismic images suggest that propagator wakes are not spatially uniform zones of low P-wave speeds (Vp) and thus alteration inferred from previous studies is likely heterogeneous within these features. We find that, despite extensive faulting within the GDZ, mantle P-wave speeds beneath Gorda are remarkably consistent with a conductively cooling lithosphere and thus do not require pervasive

hydration of the uppermost mantle. Limited deformation at mantle depths is supported by seismic anisotropy measurements that show the fast-direction of P-wave propagation rotates in concert with the magnetic anomaly lineations. This rotation may be explained by local plate kinematics without internal deformation.

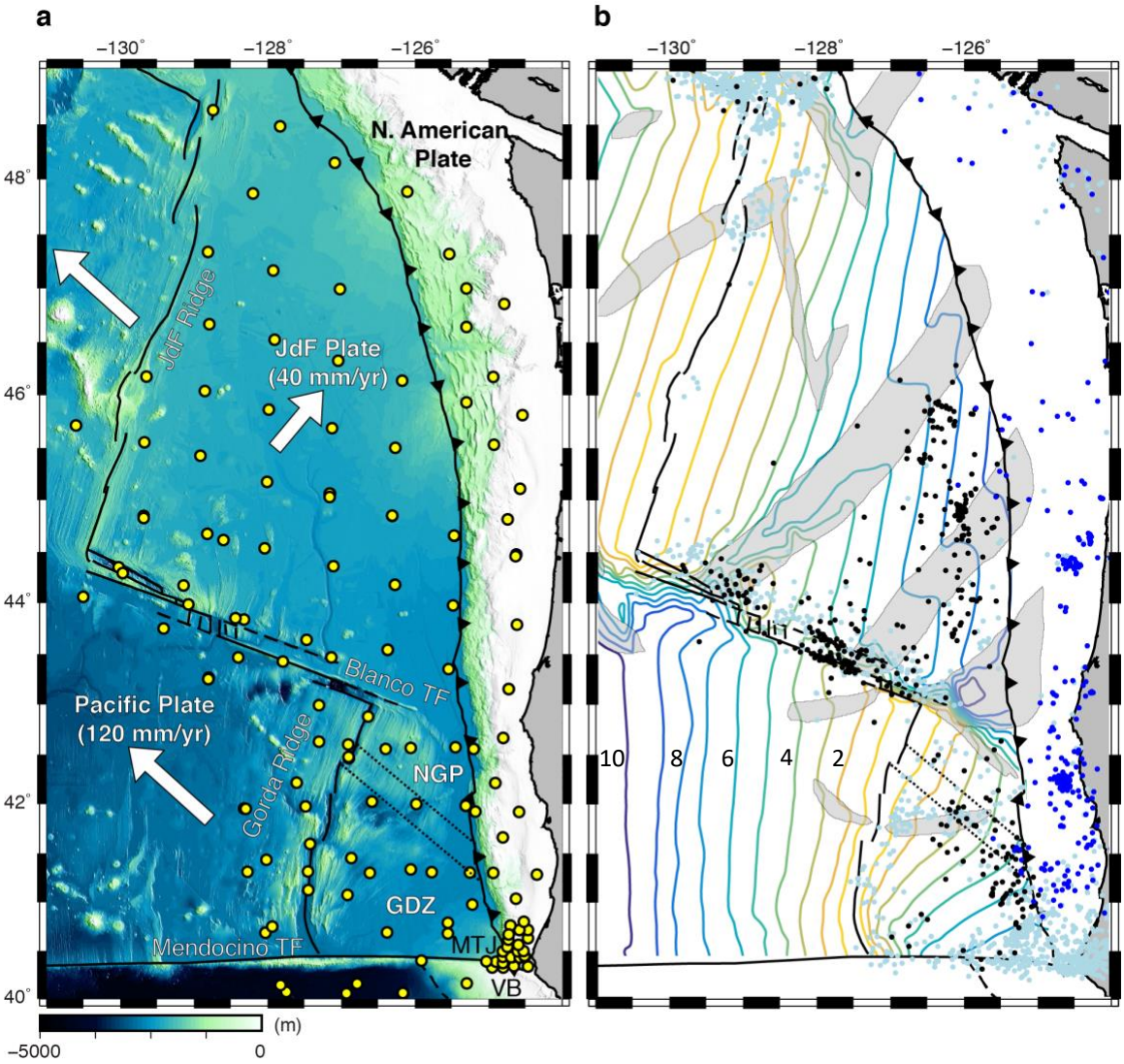

Figure 1. (a) The location of CI OBSs (yellow circles) used in this study are plotted over bathymetry. Bold white arrows define absolute plate velocities (DeMetset al., 2010). Geologic features are labeled. (b) Age of the oceanic lithosphere from Wilson (1993) is contoured in 1 Myr intervals and overlaid by seismicity recorded during the CI 4-year deployment. Epicenters published by the USGS, ISC, USArray Network Facility, and PNSN are plotted as light gray dots. Offshore microseismicity and Cascadia subduction zone related events are shown as blue and black points, respectively (Stone et al., 2018). Transparent gray bands outline regions of oceanic lithosphere disrupted by propagating ridge offsets (Wilson, 1993). Active ridge segments and transform faults are shown as black lines (Embly & Wilson, 1992). Toothed line shows the Cascadia subduction zone. Inactive plate boundaries are shown by dashed black lines. Dotted lines shows the inferred boundary between the rigidly behaving NGP and internally deforming GDZ from Wilson (1989).

2.0 Geologic Setting

Offshore of North America's Pacific northwest, the last remnants of the Farallon plate are subducting beneath North America (Figure 1). New oceanic lithosphere is being accreted primarily along two spreading systems, the Gorda Ridge in southern Cascadia and the JdF Ridge to the north which are separated by the Blanco Transform Fault (TF); the Mendocino TF defines the boundary between the Gorda region and Pacific plate. While the Gorda lithosphere is often considered separate from the JdF plate, there is no single fault that defines their boundary. There is an abrupt transition from undeformed to deformed seafloor and magnetic lineations that strikes northwest-southeast (Figure 1). We refer to oceanic lithosphere south of this line as the GDZ. For ease of reference, we refer to oceanic lithosphere north of the GDZ and south of the Blanco TF as the Northern Gorda plate (NGP) although this region may be considered (at least kinematically) as part of the JdF plate (Wilson, 1993). The proximity of the Gorda and JdF ridges to the North American plate boundary results in the subduction of some of the world's youngest (< 10 Myr) lithosphere. To the south, the Mendocino and San Andreas TFs intersect the Cascadia subduction zone to form the kinematically unstable Mendocino Triple Junction (MTJ) which is migrating northward leaving in its wake a slabless gap (Dickinson & Snyder, 1979; Furlong & Schwartz, 2004).

The unique plate boundary configuration in southern Cascadia results in extensive deformation of the Gorda lithosphere. The east-west trending Mendocino TF is kinematically inconsistent with the relative motion of the Pacific and JdF plates which currently diverge at an orientation of ~110° and full rate of 56 mm/yr (Riddihough, 1984; Wilson, 1989). This geometry results in north-south compression that appears to be

distributed across the the GDZ. As evidenced by the sinuous pattern of magnetic (Wilson, 1989; 1993) and basement lineations (Dziak et al., 2001) and abundant intra-plate seismicity (Fox et al., 2004; Dziak et al., 2011), deformation is distributed throughout the GDZ with little to no deformation extending westward onto the Pacific plate. Deformation within the GDZ initiated due to a clockwise change in Pacific-JdF RPM at ~5 Myr followed by a decrease in spreading rate at ~3 Myr (Wilson 1986; 1989).

A number of models have been proposed to explain the space problem created by the plate boundary geometry in southern Cascadia. These models often invoke large-scale right-lateral strike-slip faults that facilitate clockwise rotation of rigid blocks (e.g. review by Stoddard et al., 1991; Gulick et al., 2001). However, analysis of focal mechanism and high-resolution bathymetry suggest that the Gorda plate is deforming non-rigidly through flexural slip along ridge normal faults that have been reactivated as left-lateral strike-slip faults (Chaytor et al., 2004). Furthermore, seafloor fabrics tend to vary smoothly throughout the Gorda plate without any distinct right-lateral offsets (Dziak et al., 2001; Chaytor et al., 2004). Compression across the Mendocino TF may also result in flexural folding of the lithosphere as suggested by northwest-southeast trending linear basins (Dziak et al., 2001; Figure 1a). This folding may extend into the subducted Gorda slab which appears to be buckling under northern California (McCrory et al., 2012). Alternatively, the prominent northern linear basin near the GDZ-NGP boundary may be related to a right-lateral shear zone at depth, which Wilson (1989) speculated gives rise to the kinked seafloor fabric and magnetic anomalies at the GDZ-NGP boundary. At asthenospheric depths, Bodmer et al. (2015) interpret shear wave splitting parallel to Pacific-JdF RPM as evidence that upper mantle deformation beneath the Gorda region is

controlled by the relative motion of the surrounding plates rather than by simple shear induced by the motion of the Gorda lithosphere over the asthenosphere. The style of deformation at shallower mantle depths and its relationship to overlying brittle crustal deformation and deeper mantle flow patterns remains unclear.

In contrast to the GDZ, the JdF plate behaves rigidly with seismicity concentrated primarily along the JdF ridge, Blanco TF, and outer rise (Figure 1b). Unlike the GDZ, shear wave splitting measurements beneath the JdF plate interior (Bodmer et al., 2015; Martin-Short et al., 2015) align sub-parallel to overlying plate motion. The JdF plate is not without tectonic complexities. Several large V-shaped propagator wakes disrupt the seafloor age progression (Figure 1b) as well as the structure of the lithosphere. Active source studies have identified anomalously slow crustal and uppermost mantle velocities beneath seafloor disrupted by migrating ridge offsets interpreted as regions of increased plate hydration (Weekly et al., 2014; Soule et al., 2016; Han et al., 2016; Horning et al., 2016). In reflection studies, propagator wakes often appear as regions of anomalous crustal and mantle reflectivity (Nedimović et al., 2005; Han et al., 2016; 2018). Crust formed within and near tectonic offsets may also be compositionally distinct as suggested by generally more evolved basalt compositions (Sinton et al., 1983; Wanless et al., 2012) and denser crust (Toomey & Hooft, 2008; Marjanović et al., 2011). The Blanco TF may have inherited similar structures as it was formed via the amalgamation of multiple southward propagating tectonic offsets at ~6 Myr (Embly & Wilson, 1992; Wilson, 1993). The spatial and depth extent to which tectonic offsets influence plate structure is largely unknown as their structure is primarily constrained by 2D reflection/refraction profiles.

While the spreading rates along the JdF and N. Gorda ridge are similar, the JdF ridge is characterized by an axial high with a narrow and shallow axial graben while the Gorda ridge has a slow-spreading morphology defined by a deep axial valley (Hooft & Detrick, 1995). Spreading rate varies substantially along the Gorda ridge from ~56 mm/yr at the northern end to ~20 mm/yr at the intersection with the Mendocino TF (Riddihough, 1984; Wilson, 1993). Accompanying this decrease in spreading rate is an increase in the width and depth of the axial valley. The entire Gorda ridge is characterized by compositionally diverse but generally enriched basalt compositions erupted from isolated and small volume lava flows (Davis & Clague, 1987; Chadwick et al., 1998; Davis et al., 2008). Despite surficial evidence of limited magma input, body (Byrnes et al., 2017) and surface wave (Bell et al., 2016) tomography reveals a broad region of low shear-wave velocity (Vs) in the upper 200 km of the mantle that is located near the Gorda Ridge and extends across the Gorda plate. The Gorda upper mantle is also a region of high seismic attenuation (Eilon & Abers, 2017). The reduced Vs and high attenuation has been attributed to the presence of low degrees (~0.5-2%) of partial melt (Byrnes et al., 2017; Eilon & Abers, 2017). It is unknown how an apparently broad region of mantle upwelling and melting relates to a seemingly melt-poor axial magmatic system or influences the evolution of the Gorda lithosphere.

3.0 Data and Methods

3.1 Data and Arrival Time Measurement

We measure P-wave arrivals times from local earthquakes recorded by Cascadia Initiative ocean bottom seismometers (OBSs) and by two complimentary arrays of OBSs covering the Blanco TF and the Gorda Plate (Figure 1a; Toomey et al., 2014). We use

Cascadia Initiative data from deployment years 2-4 (July 2012 - August 2013; August 2013 - July 2014; July 2014 - October 2015). The distribution of OBSs from the year 1 deployment (July 2011 - July 2012) do not provide adequate coverage of the Blanco Transform Fault or Gorda region—the main centers of seismicity—for earthquake relocation. All seismic records were acquired through the Incorporated Research Institutions for Seismology Data Management Center (IRIS-DMC). Events analyzed in this study were selected from catalogs published by the United States Geological Survey (USGS), International Seismological Center (ISC), USArray Network Facility, and the Pacific Northwest Seismic Network (PNSN).

Over the operational period of the OBS deployments, a total of 831 events located within the experiment footprint were identified in the aforementioned catalogs (Figure 1b). Reported magnitudes vary between 1.57 and 6.9. The majority of these events cluster around the MTJ. Seismicity is clearly concentrated within the southern half of the study region. While offshore northern Cascadia is seismically active, particularly near the Explorer plate (Dziak, 2006), much of this seismicity is located outside the seismic array and, consequently, not considered in the present analysis.

Clear P arrivals are recorded at distances up to 600 km. We consider the majority of these arrivals to be Pn given the waveform characteristics, though some close-range arrivals are likely crustal P-wave refractions. The Pn phase is distinguishable by its high frequency content (3-30 Hz), typically emergent onset, long complex coda, and a move-out velocity around 8 km/s. Scattering, likely from elongate lithospheric heterogeneities, in combination with sediment and water column reverberations generates an emergent waveform with a coda that decays slowly over many 10's of seconds (Sereno & Orcutt,

1985; Kennett & Furumura, 2013; 2015). Scattering near the source region may also obscure the polarity of the Pn onset. These characteristics make accurately and consistently picking Pn arrival times difficult. Therefore, we adopt the automatic picking algorithm designed for Pn by Shintaku et al. (2014). The algorithm fits a linear profile to the smoothed natural logarithm of a bandpass filtered seismogram (see Figure 2 in Chapter III). The method takes advantage of the prominent ramp-up in amplitude associated with the Pn arrival and the onset of this ramp is taken as a proxy for the arrival time. All arrival times are picked in the 5-10 Hz frequency band on the vertical OBS channel and assigned a relative error based on the signal-to-noise ratio. Further details of the automated picking algorithm and its application to Cascadia Initiative data are discussed in Chapter III and Appendix B.

Our automatic picking procedure identified 17,531 potential P arrivals from 749 events. Similar to previous Pn tomography studies (e.g., Hearn et al., 1991), these data were subject to the following quality control process. Automatic picks were rejected if (1) the range exceeded 600 km, (2) the signal-to-noise ratio was below 5, (3) the residual after a linear move-out correction exceeded 6.5 s, (4) the pick was identified on a station recording fewer than 5 arrivals, (5) the pick was associated with an event recorded by fewer than 5 stations. The range cut-off was chosen based on visual inspection of the data quality. The signal to noise ratio was calculated using a 1 s window before and after the auto-picked arrival time. The linear move-out correction was estimated from a straight-line fit to all the data that met selection criteria 1-2. The 6.5 s buffer following the move-out correction was chosen such that good data was not rejected due to hypocentral errors

in the cataloged event locations which may exceed 40 km. The resulting dataset contains 10,894 P arrivals from 614 events.

While we relocated all 614 events in our final auto-picked dataset, only 125 well-recorded events that reflect the spatial distribution of seismicity in the study region are used for tomographic imaging (Figure 2). A total of 2,862 P arrivals were manually identified for these 125 events and assigned user-defined uncertainties; 757 of these arrivals were previously analyzed by VanderBeek and Toomey (2017; see Chapter III). This data subset provides good spatial coverage of southern Cascadia and adequate coverage of the JdF plate for tomographic analysis. We note that the inclusion of the remaining events does not substantially improve data coverage.

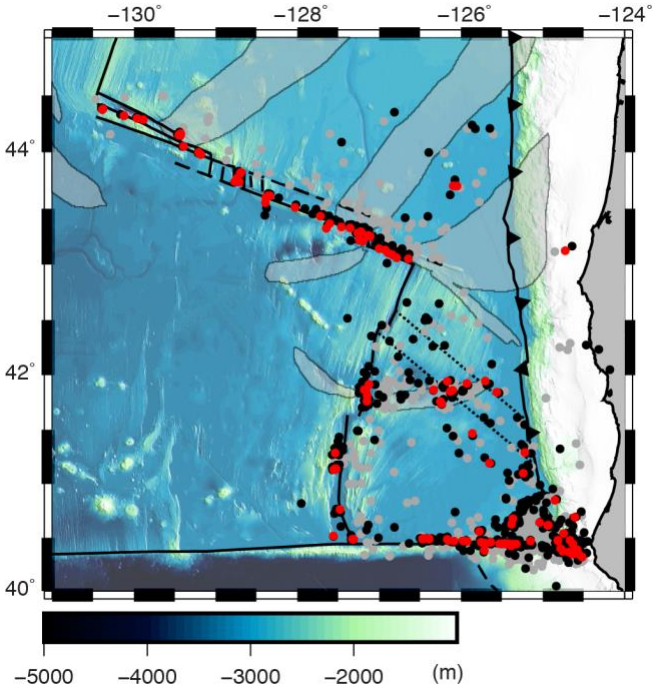

Figure 2. The cataloged epicenters of all earthquakes relocated in this study are shown as gray points. Our updated epicenters are shown in black. Red points identify the subset of sources used in our tomographic analysis.

3.2 Anisotropic Tomographic Method

We invert our P arrival time measurements for earthquake hypocentral parameters, anisotropic slowness (i.e. inverse of velocity) parameters, and station static terms. Details of the tomographic method are provided in Toomey et al. (1994) and Dunn et al. (2005). Here, we only briefly summarize the method and note that we have updated the tomographic algorithm to include equations for hypocentral parameters on a cartesian grid (e.g., Thurber, 1983). Seismic ray paths and corresponding travel-times are predicted through a 3D model parameterized in terms of anisotropic slowness using Dijkstra's algorithm (Dijkstra, 1959; Moser, 1991); the travel-time calculation explicitly includes topography. The error in the predicted arrival-time is linearly related to perturbations in the model parameters. Because the resulting system of equations is often underdetermined and ill-posed, additional regularization equations are added that act to minimize the magnitude of model perturbations and require model perturbations to be spatially smooth. We seek a solution that simultaneously minimizes the euclidean norm of the travel-time residuals, model perturbation vector, and the spatial roughness of the model perturbation vector. Specifically, we seek to minimize a function of the form

$$s^2 = \Delta t' C_d^{-1} \Delta t + \delta_m \Delta m' C_m^{-1} \Delta m + \lambda \Delta m' C_h^{-1} \Delta m + \mu \Delta m' C_v^{-1} \Delta m + \delta_h \Delta h' \Delta h + \delta_s \Delta s' \Delta s \quad (1)$$

where Δt is a vector containing the arrival time residuals; C_d is a diagonal data variance matrix defined by the squared arrival time uncertainties; Δm is the model perturbational vector for the isotropic and anisotropic slowness parameters; Δh and Δs are the hypocentral and station static perturbational vectors; C_m is a diagonal matrix containing the *a priori* model variance; C_v and C_h are matrices that apply vertical and horizontal smoothing to each model parameter; $\delta_{m,h,s}$, λ, and μ are weighting parameters that

control the importance of damping and vertical and horizontal smoothing constraints relative to the data misfit. Individual damping constants are chosen for the isotropic, anisotropic, hypocentral, and station static parameters while separate smoothing constants are chosen for isotropic and anisotropic model parameters. In Equation 1, $\Delta m, \Delta h,$ or Δs may be defined for either the current iteration or the sum of all previous iterations. If the former, the solution minimizes the magnitude of the perturbations for the current iteration and is referred to as a creeping strategy. If the latter, the solution minimizes perturbations with respect to the starting model and is referred to as a jumping strategy. The solution to Equation 1 is found via the LSQR algorithm (Paige & Saunders, 1982). The problem is non-linear in that updates to the model parameters modify the predicted ray paths which require a new system of equations to be computed. Therefore, multiple iterations of the forward and inverse problems are performed until changes in the arrival time residuals become negligible.

Seismic anisotropy in the oceanic lithosphere and upper mantle is well-approximated by a hexagonally anisotropic material with a single symmetry axis in the horizontal plane. Provided that the magnitude of anisotropy is less than ~20%, the azimuthal dependence of P-wave speeds in such a medium may be approximated as a periodic function of 2θ- and 4θ-terms (e.g. Backus, 1965; Morris et al., 1969), specifically,

$$Vp = \alpha_0 + \alpha_1 \cos(2\theta) + \alpha_2 \sin(2\theta) + \alpha_3 \cos(4\theta) + \alpha_4 \sin(4\theta) \quad (2)$$

where θ is the ray azimuth, α_0 is the azimuthally averaged P-wave speed, and α_{1-4} control the orientation and magnitude of the 2θ- and 4θ-variations. This representation is valid for seismic anisotropy resulting from olivine CPO (Nicolas & Christensen, 1987;

Ismaïl & Mainprice, 1998; Becker et al., 2006) or the alignment of small (with respect to the seismic wavelength) fractures or joints (Hudson, 1981; Crampin, 1993). Our tomographic algorithm solves only for the coefficients that modulate the 2θ-variations (see Dunn et al., 2005). This simplification is warranted considering that the 2θ-terms typically dominate azimuthal velocity variations observed within the oceanic crust (Shearer & Orcutt, 1985; Dunn & Toomey, 2001; Weekly et al., 2014) and upper mantle (Morris et al., 1969; Shearer & Orcutt, 1985; Becker et al., 2006; VanderBeek & Toomey, 2017) and, as discussed in Section 4.3, we find no evidence for significant 4θ-terms.

3.3 Starting Model and Inversion Parameters

The starting slowness model is defined on a cartesian grid with uniform 1 km spacing and consists of four domains. (1) Seaward of the trench, we use a 1D oceanic crustal velocity profile derived from a seismic refraction experiment at the Endeavour ridge (Weekly et al., 2014; Soule et al., 2016) and assume a constant crustal thickness of 6 km consistent with estimates from seismic reflection imaging (Han et al., 2016; Horning et al., 2016). (2) Landward of the trench, we prescribe a 1D velocity model representative of accretionary wedge structure in Cascadia (Yuan et al., 1994) that transitions to the 1D oceanic crustal velocity profile at the top of the subducting slab, the depth of which is taken from McCrory et al. (2012). (3) South of the Mendocino TF, we define the Vizcaino Block—an accretionary prism complex captured by the Pacific Plate (Figure 1)—based on the boundaries and 1D velocity profile described in Leitner et al. (1998). (4) The mantle is prescribed a constant P-wave speed of 7.8 km/s. We assume that the fast direction of mantle anisotropy parallels the paleo-spreading direction except

beneath the JdF plate interior where VanderBeek and Toomey (2017) measured an orientation that is rotated on average ~18° counterclockwise from the paleo-spreading direction. Paleo-spreading directions are identified from magnetic lineations (Riddihough, 1984; Wilson, 1993). Based on prior studies (VanderBeek et al., 2016; VanderBeek & Toomey, 2017), we assume the peak-to-peak magnitude of mantle anisotropy is everywhere 5%; the crust is assumed isotropic. Because our model does not accurately capture sediment thickness variations, which may exceed 2 km, we compute sediment delays with respect to our starting model and apply these as station statics. Where available, sediment thickness values beneath each station are taken from the surface wave study of Bell et al. (2015); otherwise, values are interpolated from the sediment thickness maps of Gardner et al. (1993) and Divins (2003). The cataloged source depths for offshore events vary from a few kilometers to > 20 km and have large errors. Considering such large depth variations in relatively young oceanic lithosphere to be unlikely, we initially prescribe all events a depth of 6 km beneath the top of the oceanic crust. This value was chosen based on the centroid depth distributions presented by Braunmiller and Nábělek (2008) for Blanco events.

The parameters used in the construction of our preferred tomographic solution are presented in Table 1 and briefly justified below. The sensitivity of our preferred solution to details in the starting model and choice of inversion parameters is discussed more fully in Section 4.5. Perturbational nodes for isotropic and anisotropic parameters are spaced every 10 km in the x- and y-directions. This spacing was chosen as it is comparable to the width of the first Fresnel zone for a 10 Hz P-wave propagating in a 7.8 km/s medium recorded at a range of 150 km (the mean range of the P-wave arrivals measured in this

study). A finer 1 km vertical spacing was used to limit the mapping of mantle perturbations to crustal depths.

Table 1: Inversion parameters adopted for our preferred solution.

Parameter	Value	Description
δ_u	5	Slowness damping
λ_u	1000	Horizontal slowness smoothing
μ_u	10000	Vertical slowness smoothing
δ_a	50	Anisotropy damping
λ_a	1000	Horizontal anisotropy smoothing
μ_a	10000	Vertical anisotropy smoothing
δ_e	1	Epicenter damping
δ_z	10	Source depth damping
δ_s	150	Station static damping

Because initial arrival-time residuals are dominated by relocation errors, we adopt a two-stage inversion procedure. We first invert for hypocentral parameters and station statics using our starting model. While damping of the hypocentral parameters is not strictly necessary given that we only include events recorded by 5 or more stations, we impose a relatively small damping value of 1 to limit the magnitude of the perturbations on each iteration (i.e. creeping strategy). This approach also enforces the linear approximation assumed in the inversion without biasing the results toward the starting locations. We define damping constants for epicentral and depth parameters separately. Alone, P-wave arrivals provide a poor constraint on source depth, thus, we penalize depth perturbations more heavily ($\delta = 10$). Next, we jointly invert for isotropic, anisotropic, hypocentral, and station static parameters using the source locations from the previous step. A creeping strategy is employed for isotropic and hypocentral parameters while a jumping strategy is used for anisotropic and station static perturbations. The primary purpose for including station statics in our inversions is to account for shallow structure that is not resolved in our slowness model. Sediment thickness variations are likely to be

the most significant source of arrival time variations. Accordingly, we chose a static damping value that yields perturbations with an RMS of 100 ms which is equivalent to the travel-time anomaly for a ~200 m change in sediment thickness.

4.0 Results

4.1 Earthquake Relocations

Our preferred earthquake relocations are shown in Figure 2 and were solved for using our preferred tomographic model (see Section 4.2). As with previous studies (Stoddard & Woods, 1990; Braunmiller & Nábělek, 2008), we find that the cataloged locations—derived from land-based seismic recordings—are systematically shifted east to northeast of major plate boundaries. With respect to the cataloged locations, our revised epicenters more closely follow the Gorda ridge and the Blanco and Mendocino TFs. Gorda ridge events tend to cluster near bends and offsets in the ridge axis. Intraplate events in our dataset occur primarily near the GDZ-NGP boundary. Near the MTJ, our relocated events more clearly outline a wedge-shaped pattern of seismicity that may represent the boundaries of an accreting slice of Gorda lithosphere. We estimate the 1σ errors in the epicentral locations of events used for tomographic imaging via grid-search through our preferred velocity model.

4.2 Isotropic Structure

Our preferred reconstruction of isotropic heterogeneity is shown in Figure 3 at 8 km beneath the seafloor. At this depth, structure west of the Cascadia trench is located 1-2 km beneath the Moho while structure east of the trench is located within the subducting oceanic crust and base of the accretionary wedge. We note that as a consequence of vertical smoothing, our solution does not depend on depth and 8 km is where we have the

densest ray coverage. On average, P-wave speeds beneath the JdF plate and Gorda region generally increase with increasing plate age. However, in detail there are a number of velocity anomalies that do not follow a simple velocity-age relationship.

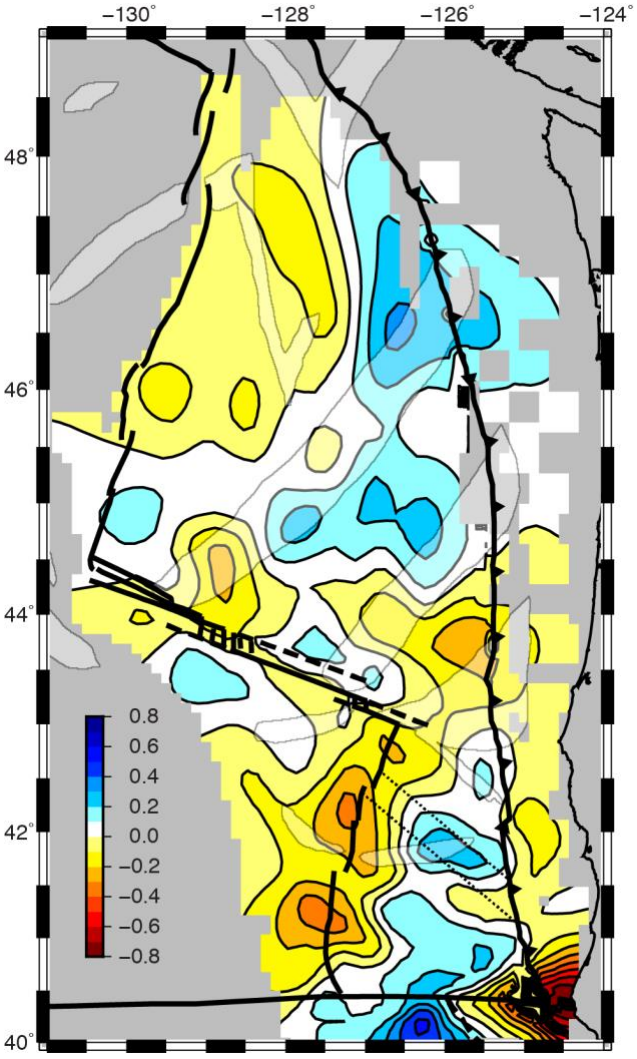

Figure 3. Velocity anomalies in our preferred tomographic solution at 8 km beneath the seafloor are contoured at 0.1 km/s intervals. Note that structure west of the trench (toothed line) is located ~2 km beneath the oceanic Moho while structure east of the trench is near the base of the accretionary wedge/ top of the oceanic crust. Areas without ray coverage are shown in gray.

Beneath the central and northern JdF plate, mantle P-wave speeds are 7.6-7.8 km/s at plate ages <5 Myr. We note that our resolution beneath the JdF ridge is limited and that the magnitude of velocity anomalies in this region are likely poorly-recovered

(see Section 4.5). At plate ages >5 Myr, Vp increase to 7.8-8.1 km/s. Velocity trends are qualitatively consistent with those observed in recent plate-wide 2D reflection/refraction profiles. Specifically, we recover a reduction in P-wave speeds near the propagator wake at ~45.5°N, 127.5°W and seaward of the trench between 45.7°N and 46.3°N similar to that observed in the velocity profiles presented by Horning et al. (2016) and Canales et al. (2017), respectively. However, the magnitude of the velocity reduction is not as great as observed in the higher resolution active-source studies. In contrast, the southern JdF plate immediately north of the Blanco TF does not exhibit as clear an age progression. In fact, some of lowest mantle P-wave speeds (~7.5 km/s) are observed within the oldest (> 8 Myr) lithosphere located at ~43.5°N, 125.5°W between two large propagator wakes. We also recover low seismic velocities beneath the terminus of a large propagator wake at 44.5°N, 128.5°W. Prior active source studies in Cascadia have found the mantle beneath pseudofaults (Horning et al., 2016; Canales et al., 2017) and the mid-ocean ridge offsets that form them (VanderBeek et al., 2016) to be anomalously slow. While we find reduced mantle velocities beneath some pseudofaults, they do not appear as uniformly slow features in our images.

Despite surficial evidence of extensive deformation, P-wave speeds beneath the Gorda interior are comparable to and generally faster than JdF mantle of similar age. Excluding the MTJ, the lowest seismic velocities (~7.5 km/s) are located beneath the Gorda ridge and are found occupying two irregularly shaped regions beneath the southern and central ridge segments. The southern ridge low velocity zone terminates at the intersection with the Mendocino TF across which velocities increase to 7.9-8.2 km/s. A similar increase in velocity is not observed at the intersection with the Blanco TF. The

low velocities recovered beneath the Gorda Ridge tend to streak out over the Pacific plate where we have limited azimuthal ray coverage. Lastly we note that the largest reductions in P-wave velocities observed in the study area are beneath the MTJ. This result is consistent with previous body-wave imaging in Cascadia using land-based arrays (Chen et al., 2015). However, our resolution landward of the deformation front is limited and constrained primarily by vertically traveling rays.

4.3 Anisotropic Structure

In Figure 4, we present the anisotropic structure of the Gorda plate at 8 km beneath the seafloor. Synthetic tests demonstrate that the limited distribution of sources within the JdF plate does not allow us to resolve spatial variations in seismic anisotropy north of the Blanco TF (Section 4.5). Consequently, north of the Blanco TF the anisotropic structure remains largely unchanged from the starting model and we focus our attention on the Gorda plate where there is nearly 360° ray coverage.

We observe an abrupt ~20° clockwise rotation in the orientation of the seismically fast propagation direction south of the GDZ-NGP boundary. This rotation coincides with the transition from undeformed to deformed magnetic and seafloor basement lineations (Figure 1 and 4). Throughout the Gorda region, the seismically fast propagation direction appears to rotate in concert with the magnetic anomaly pattern. This rotation is not observed in the immediate vicinity of the Mendocino TF where fast-axis orientations are subparallel to the fault trend as defined in the starting model. The change in the orientation of anisotropy south of the GDZ-NGP boundary is accompanied by a decrease in the magnitude of anisotropy from 6-9% in northern Gorda to 2-4% in southwest Gorda. While anisotropic magnitudes of 6-9% are more commonly associated with

oceanic lithosphere created at fast-spreading ridges (Toomey et al., 2007; Kodaira et al., 2014; Shintaku et al., 2014), they do agree with recent measurements made from active-source surveys on the JdF plate interior (Canales et al., 2017). In contrast, values of 2-4% are more comparable to seismic anisotropy created at slow-spreading environments (Gaherty et al., 2004; Dunn et al., 2005).

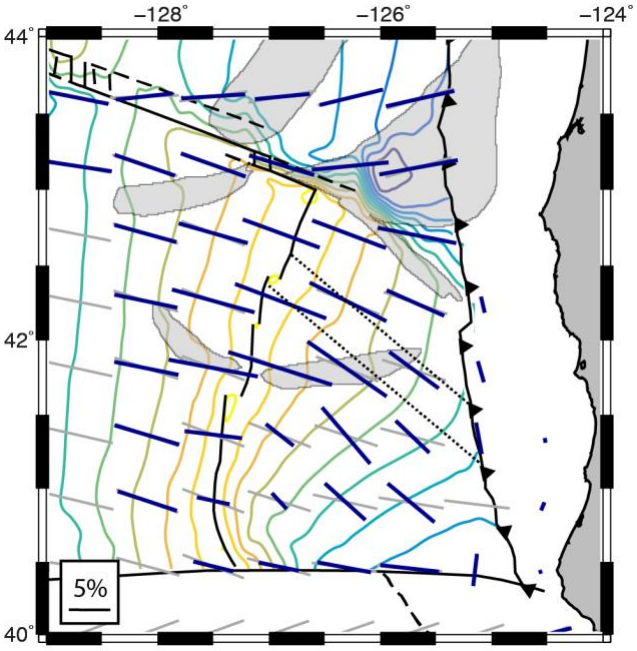

Figure 4. The orientation anisotropy recovered in our preferred solution is shown by bold blue bars where there is ray coverage. Gray bars show the orientation of anisotropy in our starting model. The length of the bars is scaled by the magnitude of anisotropy.

To assess our assumption that azimuthal variations in P-wave velocity are dominated by the 2θ terms in Equation 2, we made a second estimate of mantle anisotropy by mapping arrival-time residuals directly to perturbations in mantle velocity (Figure 5). Using the source locations from our preferred solution (Figure 2), we calculate arrival-time residuals with respect to our starting slowness model and map these residuals (Δt) directly to mantle slowness perturbations (Δu) following the equation $\Delta t = \Delta u r$ where, in this case, r is the horizontal distance the Pn ray path travelled through the

mantle. The perturbations are then applied to the constant mantle slowness assumed in the starting model and converted to velocity. We bin the velocity estimates in 20° intervals, estimate the standard error in each bin using a Student's t-test (95% confidence level), and fit Equation 2 to the binned velocities using weighted least-squares. Only arrivals recorded at ranges exceeding 50 km are considered in this analysis. At these ranges, the majority of the ray path is located within the mantle and thus primarily reflects mantle structure. We note that fitting the raw data or fitting smaller bin intervals does not change the recovered anisotropic signal beyond the estimated errors. We explored anisotropic models with and without the 4θ terms and variations in mantle anisotropy observed in geographic subsets of the data (Figure 5).

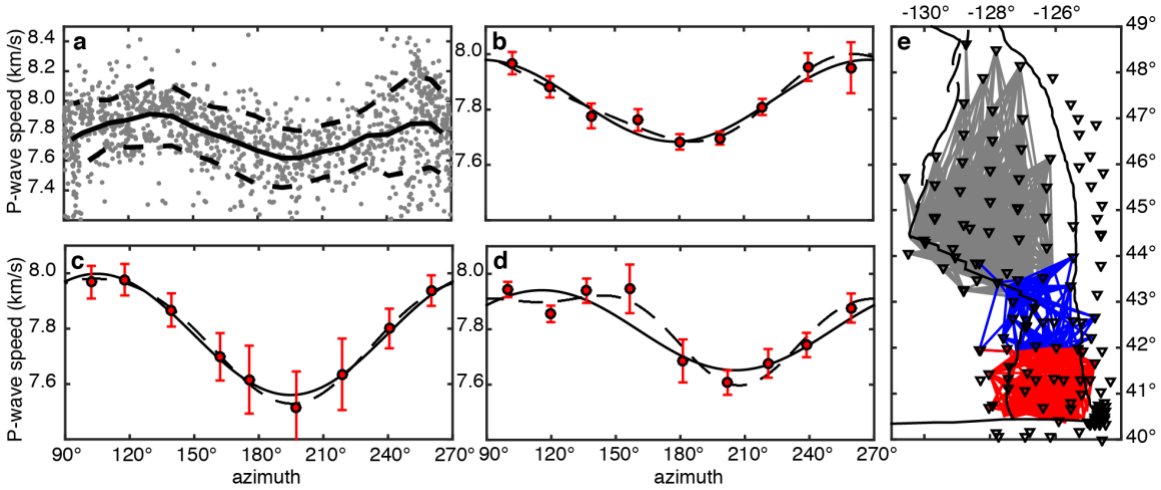

Figure 5. (a) P-wave mantle velocities estimated from arrival time residuals calculated with respect to an isotropic velocity model are plotted as a function of ray azimuth. Black line is a running average of the estimated velocities calculated in 20° overlapping (50%) intervals. The dashed black line shows the standard deviation in each interval. We plot the mean mantle velocities in 20° bins using residuals associated with ray paths confined to (b) the JdF plate interior, (c) the NGP, and (d) the GDZ. These ray paths are illustrated in e. In b-d, error bars show the 95% confidence interval in each bin estimated from a Student's t-test. We fit Equation 2 with (dashed line) and without (solid line) the 4θ terms to the binned velocity estimates. The best-fit anisotropy parameters are listed in Table 2.

Consistent with our assumption, we find that the 4θ parameters do not reduce the variance of the azimuthal velocity variations at the 95% confidence level; the best-fit 2θ parameters values are listed in Table 2. As a whole, the data exhibit a clear 2θ variation

(Figure 5a). For the JdF plate data subset (Figure 5b,e), we recover peak-to-peak azimuthal velocity variations of 3.8% ± 1.5% with a fast-axis orientation and mean velocity of 88° ± 6° and 7.83 km/s ± 0.03 km/s, respectively (errors reported are the 95% confidence intervals derived from an analysis of variance). These estimates are within error of the anisotropic structure presented by VanderBeek and Toomey (2017). For the northern Gorda region (Figure 5c,e), we measure a larger anisotropic magnitude of 5.6% ± 0.7% oriented 105° ± 1° with a mean mantle velocity of 7.78 km/s ± 0.01 km/s. In comparison, the fast-propagation direction in southern Gorda is rotated more clockwise striking 116° ± 6° and has a reduced magnitude of 3.7% ± 1.9%. The mean mantle velocity in southern Gorda is 7.8 km/s ± 0.04 km/s. The potential influence of a 4θ term is most obvious in the southern Gorda data subset. However, inclusion of the 4θ parameters did not statistically improve the fit to the data. The regional averages reported above are consistent with the 2D variations in anisotropy present in our preferred solution (Figure 4).

Table 2: Anisotropy parameter values. Values obtained by fitting Equation 2 to data subsets are tabled with their 95% confidence intervals. The resulting magnitude of anisotropy (F) and fast-axis orientation (ϕ) are also listed.

Dataset	α_0 (km/s)	α_1 (km/s)	α_2 (km/s)	F (%)	ϕ (°)
JdF	7.83 ± 0.02	0.15 ± 0.03	-0.01 ± 0.02	3.8 ± 1.5	88 ± 6
N. Gorda	7.78 ± 0.01	0.19 ± 0.02	-0.11 ± 0.02	5.6 ± 0.7	105 ± 1
S. Gorda	7.80 ± 0.04	0.09 ± 0.05	-0.11 ± 0.05	3.7 ± 1.9	116 ± 6

4.4 Preferred Solution Data Fit

The travel-time residuals with respect to our preferred solution have a weighted root-mean-square (RMS) of 204 ms while the weighted RMS with respect to the starting model and cataloged earthquake locations is 2771 ms. To place these values in perspective, other passive source Pn tomography studies typically fit arrival time data to

>500 ms (Hearn et al. 1991; Pei et al., 2007; Buehler & Shearer, 2010). Local earthquake P-wave imaging generally yields solutions that more closely predict observed data with residual RMS near 100-300 ms (e.g. Zhao et al., 1992; Koulakov et al., 2011) while active source studies provide the highest resolution (residual RMS of 10-20 ms) of earth structure (e.g., Toomey et al., 2007; VanderBeek et al., 2016) using traditional travel-time tomography methods. Our initial source relocation is responsible for the greatest improvement in data fit which reduces the variance in the arrival time residuals by 99%. Subsequent inversion for isotropic and anisotropic heterogeneity further reduces the variance by 48%.

4.5 Solution Sensitivity and Resolution

In the selection of user-defined smoothing and damping parameters, we ran a number of inversions using both synthetic and actual data and assessed the resulting images, data residuals, and variance in the model perturbations. The values for our preferred solution are presented in Table 1 and reflect a trade-off between resolution and data fit. We found it prudent to more heavily damp anisotropic perturbations with respect to isotropic updates. Reducing the anisotropic damping resulted in azimuthal velocity variations that exceeded 11% without improving the data fit. Such high values are uncharacteristically large for oceanic mantle and so we chose the more conservative solution. We note that the recovered fast-propagation direction was independent of the chosen damping. Given the limited depth sensitivity of the Pn seismic phase, we also chose to more heavily smooth perturbations vertically such that the mantle structure did not exhibit strong depth variations.

To assess the importance of anisotropy in fitting our data set we considered purely isotropic solutions (isotropic starting model without inversion for anisotropic parameters) and models where spreading-aligned anisotropy was fixed throughout all iterations. Purely isotropic solutions both increased the magnitude of isotropic anomalies while worsening the data fit (weighted RMS of 218 ms). If spreading-aligned anisotropy is imposed on the starting model but held fixed through the inversion, we recover effectively identical isotropic solutions with respect to our preferred model with a slightly larger residual RMS (214 ms). This solution may provide a simpler alternative model but one that does not explain the rotated anisotropy signal observed in the data (Figure 5d) or provide any potentially new insights into lithospheric deformation beneath Gorda.

We explored the sensitivity of our results to the starting model. To assess whether absolute mantle velocities are well constrained and to identify any potential trade-offs between average mantle velocity and source origin times, we generated solutions using starting models with a 7.6 km/s and a 8.0 km/s mantle to compare with our preferred solution which used 7.8 km/s. Regardless of the starting mantle velocity model, we found that the inversion converged to nearly identical solutions. To investigate whether the recovered anisotropic parameters depended on the anisotropic starting model, we ran inversions with an initially isotropic mantle. We recovered similar fast-axis orientations beneath NGP and GDZ but at reduced magnitudes (2-4%) while north of the Blanco TF the solution remained effectively isotropic. Gorda isotropic structure is largely unmodified when using an isotropic starting model. However, we recover larger reductions in Vp beneath the JdF plate. We attribute the slower JdF plate velocities to the

primarily north-south oriented ray paths which are sampling the predicted slow mantle direction if anisotropy is present.

We performed inversions with synthetic data generated from known velocity models to evaluate the resolution of our dataset. For these resolution tests we use the same inversion parameters, data geometry, and starting model as our preferred solution and add normally distributed noise with a standard deviation of 200 ms to the synthetic arrival times. We use the earthquake locations (red events) presented in Figure 2 as the true source positions and the cataloged event locations as the starting positions. While a number of synthetic test were performed, we present the results from two that illustrate the spatial resolution of our dataset and demonstrate our ability to capture variations in the orientation of anisotropy and predicted thermal evolution of the lithosphere.

To estimate the spatial limits of our isotropic resolution we reconstruct sinusoidal checkerboard-patterned velocity anomalies. The true velocity model contained spreading-aligned anisotropy at mantle depths with a magnitude of 5%. The results for 100-km wide anomalies with amplitude of ± 0.25 km/s are presented in Figure 6. Anomalies at this scale are clearly resolvable by our dataset though resolution diminishes toward the northwest corner of the JdF plate. Perturbations to anisotropic parameters were allowed in this synthetic inversion. However, the magnitude of anisotropy changed by less than 0.5% with no significant changes in the fast-axis orientations indicating minimal trade-off between isotropic and anisotropic heterogeneity. Further checkerboard resolution tests indicate that our resolution rapidly decreases for smaller wavelength anomalies whose amplitude is adjusted to yield the same travel-time perturbations as the 100 km sinusoidal

checkerboard. In general, we conclude that heterogeneity with dimensions less than ~50 km should not be interpreted.

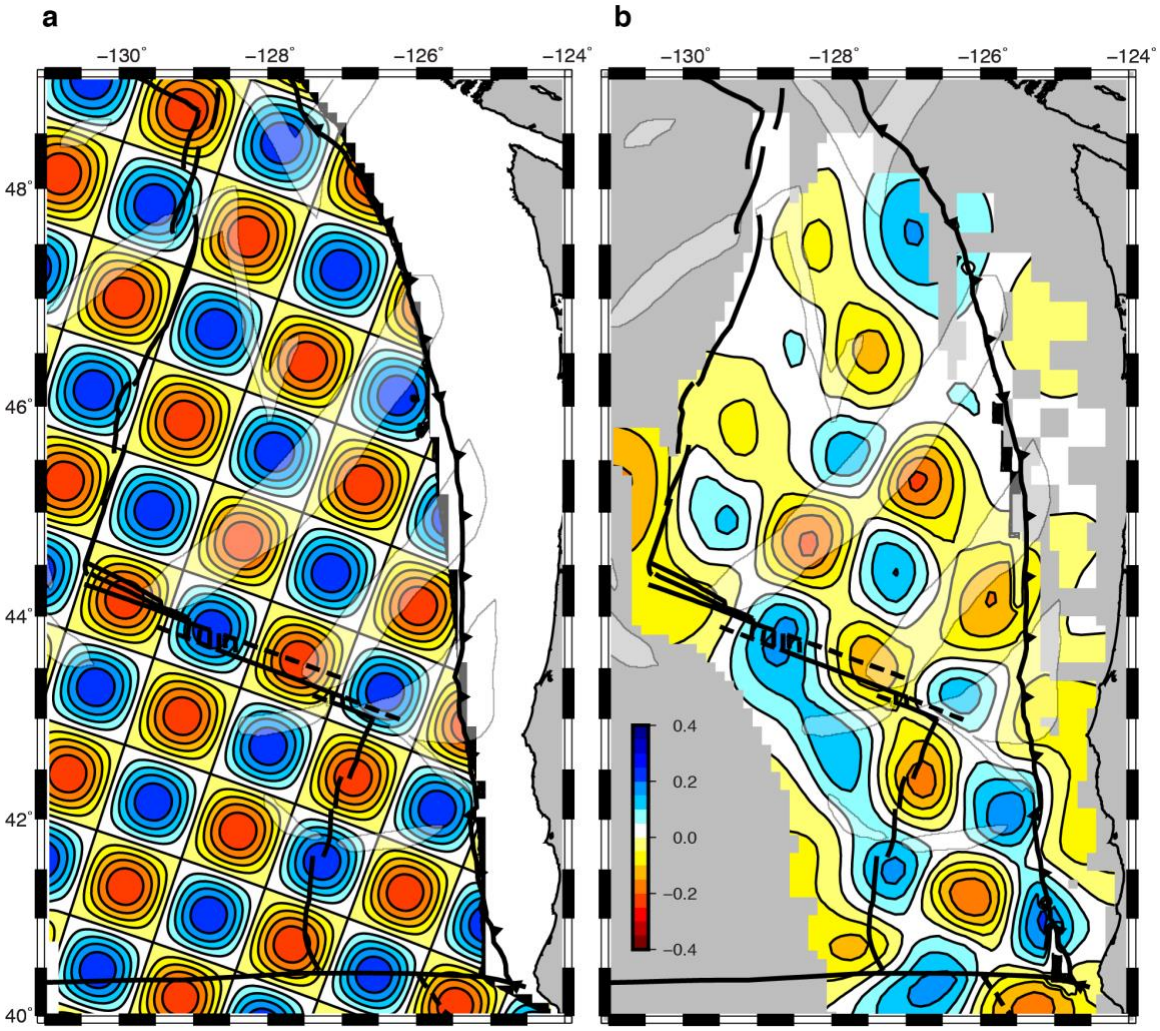

Figure 6. (a) Input and (b) recovered sinusoidal mantle velocity anomalies. Regions without ray coverage are masked in gray. Color scale for (a) is shown in (b). Contour interval is 0.05 km/s. Depth slices are shown at 8 km beneath the seafloor.

The primary goal of this study is to constrain how the seismic structure of the lithosphere evolves as a function of plate age and to determine how deformation of the Gorda plate affects the anisotropic velocity structure of the uppermost mantle. To this end, we constructed a synthetic model in which the mantle velocities varied in accordance with temperature predicted from a half-space cooling model (HSCM; Figure 7a) where temperature is mapped to Vp following Isaak (1992). The synthetic model

contained 5% mantle anisotropy aligned with the spreading direction. South of ~42° N, the orientation of anisotropy was rotated 25° clockwise of the spreading direction. Our recovery of this model is shown in Figure 7b.

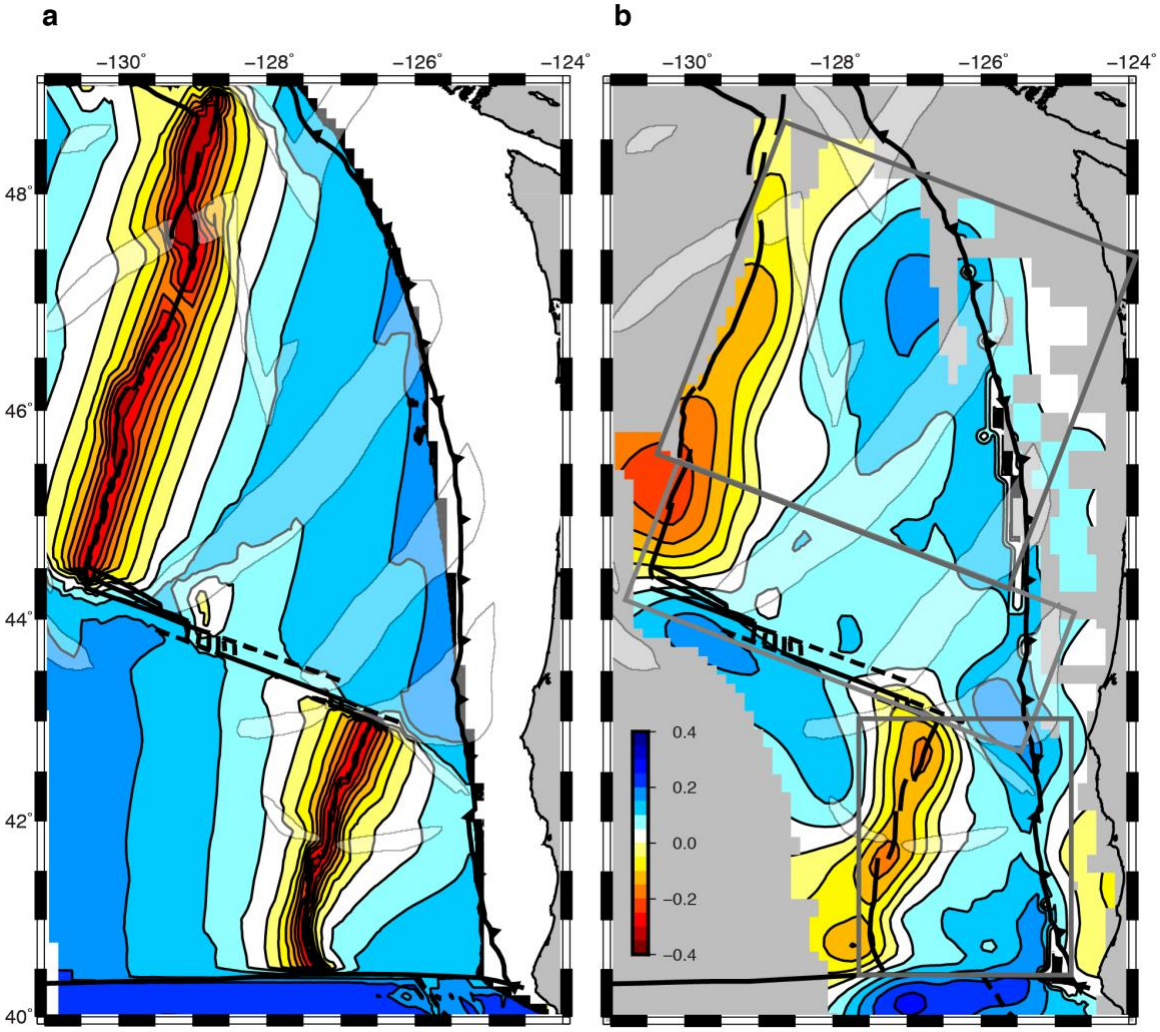

Figure 7. (a) Synthetic velocity model constructed by converting mantle temperatures predicted by a HSCM to P-wave velocity (see text for details). (b) Recovery of synthetic model shown in (a). Regions without ray coverage are masked in gray. The regions considered for the velocity-age plots shown in Figure 8 and 10 are outlined by dark grey boxes. Color scale for (a) is shown in (b). Contour interval is 0.05 km/s. Depth slices are shown at 8 km beneath the seafloor.

In Figure 8, we bin the recovered velocities as a function of age in 2 Myr intervals for the Gorda region, a 100 km-wide corridor that parallels and extends northward from the Blanco TF, and the northern JdF plate. We accurately recover the prescribed plate age dependence beneath the NGP and GDZ with the exception that P-wave speeds are on

average too fast at young plate ages (<2 Myr). The plate age trend is reasonably well recovered beneath the Blanco corridor and northern JdF plate although velocities are on average underestimated by ~0.05 km/s.

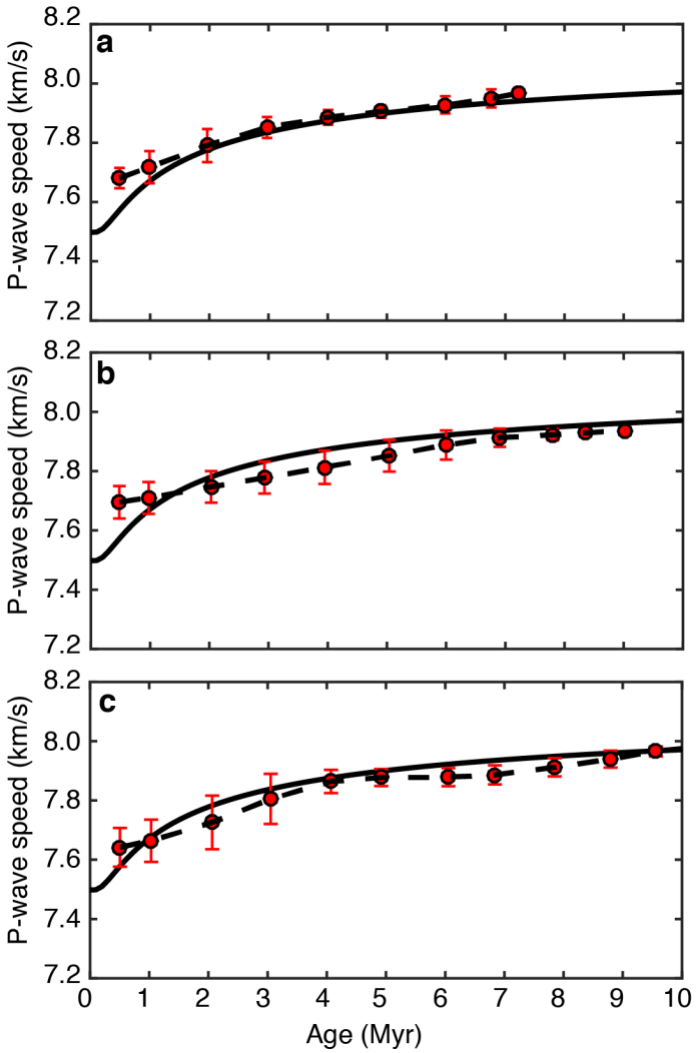

Figure 8. Recovered P-wave velocities in Figure 7b plotted as a function of plate age for model nodes located within the mantle beneath (a) the NGP and GDZ, (b) the northern JdF plate, and (c) the Blanco corridor. The map view extent of these regions are shown in Figure 7b. Velocities are averaged in 2 Myr intervals within each region (red points) and exclude nodes without ray coverage. The input velocity-age relationship is shown by the solid black line. Error bars show the standard deviation in each bin.

We recover the clockwise rotation in anisotropy beneath the Gorda region (Figure 9). However, we underestimate the rotation by ~5°-10°; the magnitude of anisotropy is

largely unchanged from the starting model. From these tests, we conclude that our dataset is capable of resolving an age dependent thermal structure and that deviations from such a trend likely represent true earth structure. Additionally, the change in anisotropy between the NGP and the GDZ in our preferred solution is a robust feature although the rotation may be underestimated.

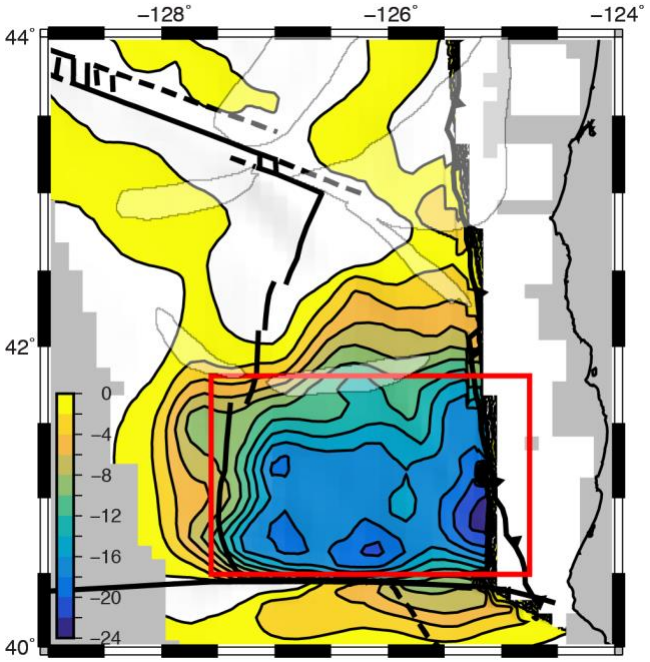

Figure 9. Recovery of a 25° clockwise rotation in the orientation of mantle anisotropy at 8 km beneath the seafloor. The fast-axis orientation of anisotropy recovered is contoured at 2° intervals. The true region of rotated anisotropy is shown by the red box.

5.0 Interpretation and Discussion of Tomographic Results

Our Pn seismic images provide a unique opportunity to investigate heterogeneity within the uppermost mantle across an entire oceanic plate. While Pn tomography studies of oceanic lithosphere have been carried out for decades (e.g., Raitt et al., 1963; Morris et al., 1969), they have typically been restricted to 2D active-source refraction/reflection profiles (e.g., Lizarralde et al., 2004; Gaherty et al., 2004; Horning et al., 2016) and/or are conducted over a geographically limited area (e.g., Dunn et al., 2005; Shintaku et al.,

2014; VanderBeek et al., 2016). The dominantly horizontal propagation paths and high frequency content of Pn waves helps fill a resolution gap in mantle imaging. Owing to the relatively low frequency content of seismic arrivals used in teleseismic body and surface wave studies, these data tend to vertically average structure over many 10's of kilometers. In comparison, the arrival times of Pn are sensitive to structure within a Fresnel volume around the geometrical ray path that has limited sensitivity to overlying crustal structure (Zhang et al., 2007). The maximum radius of the Fresnel volume can be approximated by $0.5\sqrt{RV_p/f}$ where *R* and *f* are the propagation distance and dominant frequency, respectively. Thus, the 5-10 Hz Pn waves traveling beneath the Moho recorded at 150 km (on average) considered in this study are sensitive to structure within the upper ~6 km of the mantle. We use our seismic images to evaluate the thermal evolution of the uppermost mantle and to make inferences on how deformation within Gorda extends beneath the Moho.

5.1 Isotropic Structure of Gorda and Juan de Fuca

In Figure 10 we plot the mean mantle velocity in our preferred solution at 8 km depth as a function of age for the Gorda and northern JdF plates and for a 100 km-wide corridor that extends northward from and parallels the Blanco TF; these regions are outlined in Fgure 7b. We compare our measured Vp values to those derived from a HSCM where mantle temperature is vertically averaged over 7-12 km depth (the approximate depth sensitivity of the Pn arrival times) and converted to Vp perturbations using the anharmonic temperature derivative for peridotite $\left(\frac{\partial \ln V_p}{\partial T} = -6.2 * 10^{-5}\ K^{-1}\right)$ measured by Isaak (1992). To define absolute Vp, we assume an isotropic mantle velocity of 8.155 km/s at 0 °C consistent with the average elastic properties of natural

peridotites (Ismaïl & Mainprice, 1998). For the thermal calculation, we assume a mantle temperature and thermal diffusivity of 1200 °C and 10^{-6} m^2/s, respectively.

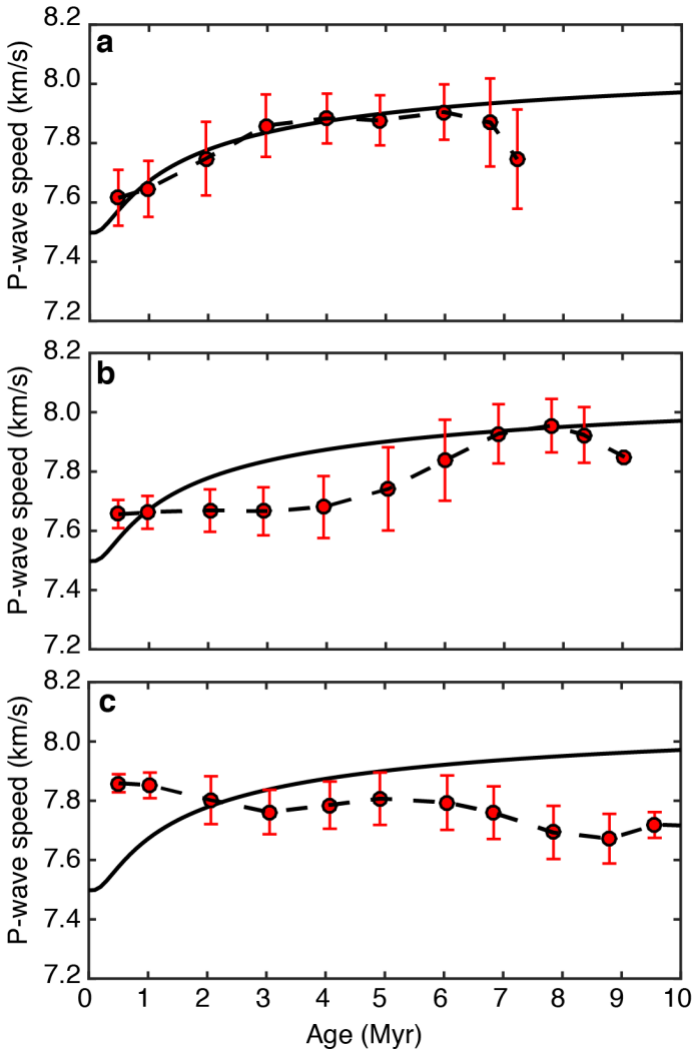

Figure 10. Mean mantle velocities in our preferred solution are plotted as a function of plate age for model nodes located beneath (a) the NGP and GDZ, (b) the northern JdF plate, and (c) the Blanco corridor. These regions are outlined in Figure 7b. Velocities are averaged in 2 Myr intervals within each region (red points) and exclude nodes without ray coverage. Error bars show the standard deviation in each bin. The predicted velocity-age relationship from a HSCM averaged over the upper 5 km of the mantle is shown by the solid black line.

The average seismic velocity structure of the Gorda mantle lithosphere is remarkably consistent with predictions from a HSCM (Figure 10a). This is perhaps surprising given the abundant evidence of faulting at the surface. If these faults extend

past the Moho, then we would expect to observe a strong decrease in seismic velocity due to a combination of increased porosity and mineral alteration (Hacker et al., 2003a; Miller & Lizarralde, 2016; Korenaga, 2017). Such velocity reductions are commonly observed in the outer-rise region of subduction zones where bend-related normal faults may penetrate many kilometers beneath the Moho (Faccenda et al., 2009; Ranero et al., 2009; Shillington et al., 2015; Han et al., 2016; 2018). In Cascadia, bend-related faulting is observed to extend 6-7 km beneath the Moho in ~8.5 Myr lithosphere (Han et al., 2016). If these depths coincide with the brittle-ductile transition, they imply a thermal limit to faulting of ~500 °C (estimated from a HSCM). The Gorda interior is ~4 Myr. At this age, a HSCM predicts the depth of the 500 °C isotherm to lie ~3 km beneath the Moho. This depth interval is well within the sensitivity of our Pn measurements. We conclude that pervasive deformation of the Gorda plate does not result in anomalous alteration or hydration of the uppermost ~6 km of the Gorda mantle. However, we cannot rule out the possibility of localized zones of mantle alteration that are near or below our limit of our resolution. Perhaps the NW-SE trending bands of 7.7-7.8 km/s mantle that interrupt the higher plate interior velocities (Figure 3) reflect such localization, though there are no crustal faults with this orientation (Dziak et al., 2001; Chaytor et al., 2004) to support this interpretation. The possibility also exists that mantle alteration is confined to the base of the Moho thereby having a limited influence on our Pn velocity measurements. Either situation implies volumetrically small extents of mantle alteration and, consequently, limited mantle water storage potential.

The most anomalous mantle velocities within the Gorda region are observed in the southeast corner near the MTJ where Vp is reduced to 7.5 km/s . The relatively low

velocities recorded in this region cause the Gorda age progression to deviate from the HSCM prediction beyond ~6 Myr (Figure 10a). Offshore seismic reflection profiles image overlapping wedges of oceanic crust within this region (Gulick et al., 1998). We interpret these velocitites to reflect thickened oceanic crust and intense faulting and fracturing throughout the Gorda lithosphere.

In contrast to the Gorda plate, mantle Vp within the northern JdF plate (Figure 10b) and Blanco corridor (Figure 10c) does not exhibit a clear age dependence. Beneath northern JdF, Vp remains relatively constant (7.6-7.7 km/s) over ~4 Myr before abruptly increasing to ~7.9 km/s. This behavior may reflect poor resolution of our dataset in northern Cascadia (Figure 6b). However, synthetic tests illustrate that our data is capable of better resolving a HSCM trend than is shown by our results (Figure 8). An alternative interpretation is that the attenuation structure of the lithosphere east of the JdF ridge is anomalously low and anelastic processes give rise to the decrease in velocity with respect to the HSCM prediction (Karato, 1993). We note that the abrupt increase in Pn velocities coincides with a similar increase in asthenospheric velocities (Bell et al., 2016; Byrnes et al., 2017) and attenuation (Eilon & Abers, 2017) suggesting that asthenospheric dynamics may influence the thermal evolution of the lithosphere.

The Vp-age trend beneath the Blanco corridor is even more anomalous and exhibits a general decrease in velocity with plate age. This behavior is largely the result of two 50-100 km-wide mantle low-velocity zones (MLVZs) located near the termini of large propagator wakes (Figure 3). The more eastern of these anomalies is also located within a zone of outer-rise seismicity and where the oceanic lithosphere is oldest (Figure 1b). We infer that the ends of propagator wakes on the JdF plate are zones of anomalous

mantle alteration. Given that the observed MLVZs occur beneath ~5 Myr and ~8.5 Myr seafloor, the most probable explanation is deep fracturing of the lithosphere facilitated by structural weaknesses inherited from rift propagation. Indeed, greater fracturing throughout the crust and possibly extending beneath the Moho is inferred from a number of seismic studies that image lithosphere modified by tectonic offsets (e.g. Canales et al., 2003; Weekly et al., 2014; Horning et al., 2016; Soule et al., 2016). The western MLVZ zone near 129°W is 0.2-0.3 km/s slower than the predicted velocity for unaltered mantle peridotite of the same age while the eastern most is reduced by 0.3-0.4 km/s. The magnitude of these anomalies could be explained by a small percentage of fluid-filled porosity (<0.5%) or a larger volume fraction of peridotite altered to serpentinite (<4%; Korenaga, 2017). Neglecting anelastic effects, a thermal anomaly exceeding 500 °C would be required to explain the same reduction in velocity. If anelastic effects are considered (Karato, 1993), a smaller thermal anomaly (< 100 °C) could explain the velocity reduction if the lithospheric seismic quality factor (Q) is < 100. We consider such high thermal anomalies and low Q values to be unlikely for oceanic lithosphere > 4 Myr old. On the JdF plate, 2D active source reflection profiles find reductions in mantle Vp of ~1 km/s beneath the two north-northeast trending propagator wakes. If such reductions in mantle velocity were spatially uniform along the entire trace of the propagator wakes and extended a few kilometers into the mantle section, then we should be able to resolve such features. However, this correlation is not observed. It seems unlikely that the reduced mantle Vp observed in the profiles of Horning et al. (2016) is purely happenstance given the large number of geophysical studies that have identified anomalous crustal and mantle structure associated with propagator wakes and the mid-

ocean ridge offsets that form them (e.g. Canales et al., 2003; Nedimović et al., 2005; Toomey & Hooft, 2008; Marjanović et al., 2011; VanderBeek et al., 2016; Han et al., 2016; 2018). Therefore, we interpret our seismic images as evidence that the depth to which lithospheric accretion is influenced by tectonic offsets is restricted to the shallowest ~1 km of the mantle. The exception may be the termini of propagator wakes. The reason for this, at least in southern JdF plate, maybe due to interactions between propagating rifts and the Blanco TF, which was itself formed via the merging of multiple smaller tectonic offsets (Wilson, 1988).

We interpret the two MLVZ beneath the Gorda Ridge as evidence for a segmented mantle magmatic system. Given their proximity to the plate boundary, the reduced velocities are most likely due to a combination of increased temperature and presence of partial melt resulting from mantle upwelling. If the reduced P-wave speeds are due solely to temperature, then using the anharmonic derivative from Isaak (1992) yields axial mantle temperatures of ~1300 °C. This temperature exceeds the dry mantle solidus (~1160 °C; Hirschmann et al., 2000) and implies the presence of partial melt. The temperature estimates above do not consider anelastic effects on the P-wave speed thermal dependence which may reduce the temperature perturbation required to explain the velocity anomaly (Karato, 1993). Generally, the oceanic lithosphere is regarded as a very low attenuating zone (e.g. Kennett et al., 2014; Takeuchi et al., 2017) and, consequently, anelasticity is predicted to have a small effect on the P-wave speed thermal dependence (Karato, 1993). The exception may be near spreading centers where temperatures are elevated (Kennett et al., 2014). Using the anelastic temperature derivatives presented in Karato (1993) with a Q factor representative of young oceanic

lithosphere (100), the MLVZs may be explained by axial mantle temperatures of ~850 °C and, thus, would not require partial melt. In either case, the Gorda ridge is punctuated by two zones of relatively elevated mantle temperatures with possibly low degrees of partial melt. The boundary between what we interpret as two magmatic centers coincides with a ~12 km right-stepping non-transform offset. We note that the temperature estimates are a minimum given that travel-time tomography will underestimate the magnitude of low velocity regions. Unfortunately, limited data coverage of the JdF ridge does not allow us to place constraints on the temperature and extent of melt within the axial mantle magmatic system in this region.

5.2 Gorda Anisotropy and Deformation

We interpret our Pn anisotropy observations beneath Gorda as a result of kinematic rotation of oceanic mantle lithosphere south of the GDZ-NGP boundary. Seismic anisotropy within the oceanic lithosphere is most commonly attributed to the frozen-in signal of corner flow beneath the paleo-spreading center where the divergence of mantle material aligns the crystallographic a-axes of olivine (the seismically fast propagation direction) in the direction of spreading (e.g. Blackman & Kendall, 2002). North of the GDZ-NGP boundary, the seismically fast axis of anisotropy is parallel to Pacific-JdF RPM consistent with a mid-ocean ridge origin. South of the GDZ-NGP boundary, we observe a ~20° clockwise rotation in the anisotropic fabric with respect to JdF-Pacific RPM or, equivalently, a ~40° clockwise rotation with respect to the east-west orientation of divergence along the southern Gorda Ridge. We suggest that the rotation in anisotropy is simply a kinematic response to along-axis changes in spreading rate (Figure 11). While the anisotropic structure could reflect the preferential alignment of small

(with respect to the seismic wavelength) fractures or faults (Crampin, 1993; Hudson, 1981) with or without an anisotropic mineral fabric, we consider this scenario unlikely for the following reasons. Pervasive faulting of the uppermost mantle would reduce P-wave speeds which is not observed. Anisotropy from aligned fractures results in a fast-propagation direction parallel to the fractures and faulting patterns on the surface are normal to the measured fast direction.

In Figure 11, we illustrate the predicted motion of slices of lithosphere if the plate divergence velocity at the Mendocino TF is 25 km/Myr and increases linearly to 55 km/Myr at ~42°N. The eastward fanning of these blocks is similar to that observed in the magnetic anomaly lineations (Figure 4) and acts to rotate seismic anisotropy generated beneath ridge. There is a clear space problem along the northern and southern boundaries of the GDZ where blocks overlap with adjacent lithosphere placing the GDZ in compression. At crustal depths, the predicted north-south compression appears to be accommodated by flexural slip along ridge-normal faults (Chaytor et al., 2004). It is unlikely that this style of deformation continues into the mantle considering that ridge normal faults are not observed to penetrate the Moho (Nedimović et al., 2009; Han et al., 2016) and, thus, there are no preexisting zones of weakness that would favor a flexural slip model. Additionally, we do not observe decreased P-wave speeds that would accompany pervasive mantle faulting. Instead, the relatively young Gorda lithosphere may exhibit more ductile behavior. In this case, north-short shortening may be accommodated by the extrusion of material to the east and west or perhaps by thickening of the mantle lithosphere near the boundaries of the GDZ.

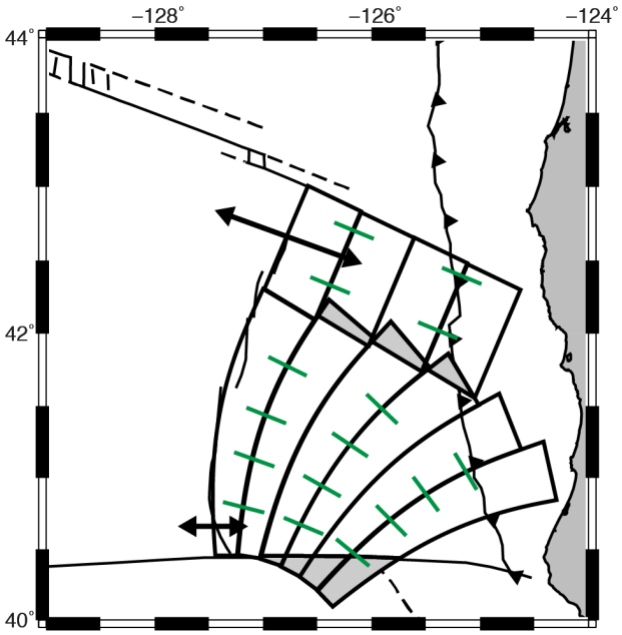

Figure 11. Cartoon illustrating the rotation of slices of mantle lithosphere due to a southward decrease in spreading rate along the central and southern Gorda Ridges. Double-headed arrows parallel the spreading direction and inferred orientation of anisotropy created beneath the ridge. Green bars show the progressive rotation of mantle anisotropy with the slices of lithosphere. Gray shaded regions highlight areas of convergence between the GDZ and adjacent plates. See text for discussion.

6.0 Conclusion

Using seismic data collected by the Cascadia Initiative experiment we have mapped the seismic velocity structure of the JdF plate system from accretion to subduction. We find anomalously slow mantle velocities along the southern edge of the JdF plate that do not exhibit a clear age progression as is predicted by conductive cooling models for the oceanic lithosphere. We attribute these velocity reductions to low degrees of mantle hydration that extends several kilometers beneath the Moho. We infer that the deformation that facilitated this hydration was driven by the interaction between propagating tectonic offsets and the Blanco TF. However, we do not find that propagator wakes are uniformly seismically slow features at mantle depths. If alteration of the

mantle underlying propagator wakes is present, as inferred from previous active-source studies, we infer that it must be restricted to the shallowest 1 km of the mantle. In contrast to the JdF plate, the velocity structure of the Gorda mantle is remarkably consistent with predictions from a HSCM despite surficial evidence of extensive faulting and deformation. Measurements of seismic anisotropy beneath Gorda reveals that mantle mineral fabrics generated beneath the ridge have been rotated such that the fast-direction of P-wave propagation aligns normal to the trend of deformed magnetic lineations. Given that isotropic P-wave speeds beneath Gorda are not anomalously slow, we infer that crustal deformation is decoupled from the motion of the underlying mantle.

7.0 Bridge

Chapters II-IV focused on the evolution of the uppermost mantle (i.e. within ~10 km of the Moho) from the ridge to the trench. In Chapter V, I consider the structure of the deeper (upper ~400 km) mantle offshore Cascadia. I propose a joint tomographic analysis of teleseismic body and surface wave data to constrain the geometry of mantle upwelling and melt production beneath the JdF and Gorda ridges. This chapter provides scientific motivation for the joint analysis and describes the method.

CHAPTER V

IMPROVED SEISMIC IMAGING OF MANTLE DYNAMICS OFFSHORE CASCADIA FROM THE JOINT INVERSION OF BODY AND SURFACE WAVES: MOTIVATION AND CHARACTERIZATION OF THE PROBLEM

1.0 Introduction and Motivation

A long-standing question in the study of mid-ocean ridge (MOR) dynamics is whether mantle upwelling is passive or active. In the passive model, the divergence of the overlying plates excites a corner-flow pattern that produces a broad (100's of kilometers) triangular-shaped region of mantle upwelling and melting centered beneath the plate boundary (e.g., Spiegelman & McKenzie, 1987). A purely plate driven flow field is 2D and symmetric about the ridge axis. Active flow models consider internal buoyancy forces, originating from retained melt and thermal or compositional heterogeneity (Scott & Stevenson, 1989; Buck & Su, 1989; Katz, 2010), on the externally driven flow geometry. Active models are capable of producing symmetry-breaking convective flow fields that vary both along and across axis and tend to produce narrower melting columns (Rabinowicz et al., 1993; Choblet & Parmentier, 2001; Katz, 2010). Ultimately, buoyancy-driven convection is sensitive to mantle viscosity and generally requires values below ~10^{19} Pa s (Choblet & Parmentier, 2001; Katz, 2010). The viscosity structure reflects the degree and distribution of partial melt and mantle temperature, chemistry, and grain size. Therefore, discerning the upwelling geometry beneath spreading segments can yield insights into fundamental mantle properties and has implications for the thermal evolution of young oceanic lithosphere.

The simplicity of the passive model and its ability to explain global MOR basalt systematics (Langmuir et al., 1992; Brown & White, 1994) has lead to its prominence. However, a growing number of geophysical observations seemingly require features of active upwelling models. The style of mantle upwelling beneath MORs is perhaps best characterized beneath the fast-spreading southern East Pacific Rise (EPR) near 18° S where the MELT (Forsyth et al., 1998) and GLIMPS (Harmon et al., 2004; 2006) experiments were deployed. Seismic (Harmon et al., 2009; Hammond & Toomey, 2003) and electromagnetic (Evans et al., 1999; Baba et al., 2006) imaging studies using MELT and GLIMPSE data identified a broad (up to ~200 km wide and equally deep) region of low-seismic velocities and high electrical conductivity generally interpreted as the MOR melt production region containing <1% interstitial melt. While a broad melt production region is generally consistent with a passive model, the inferred upwelling region is asymmetric about the ridge axis with greater degree of melting west of the plate boundary—a feature predicted by active flow models (e.g., Katz, 2010). The seismic anisotropic structure, which reflects the distribution of strain within the mantle and hence the flow field, is also asymmetric about the EPR (Wolfe & Solomon, 1998; Hammond & Toomey, 2003). The asymmetric mantle structure beneath the southern EPR has been attributed to the proximity of the ridge to the South Pacific Superswell. Models of plate-driven mantle upwelling subject to asymmetric boundary conditions (i.e. warmer temperatures west of the ridge and east-west oriented pressure gradient) may explain the observed asymmetries (Conder et al., 2002; Toomey et al., 2002) without invoking buoyancy. However, the abrupt increase in seismic velocity east of the EPR observed in Love (Dunn & Forsyth, 2003) and Rayleigh (Harmon et al., 2009) wave tomography

studies may indicate mantle downwelling on the eastern flank requiring a component of active flow. Observations of upper mantle structure in other spreading environments are limited. Along the northern EPR (~9° N), electromagnetic imaging suggests a passive upwelling regime as evidenced by a ~100 km deep triangular region of high conductivity flanked by a 60 km-thick resistive mantle (Key et al., 2013). However, at the same ridge segment the seismically inferred distribution of mantle melt and orientation of mantle flow at near-Moho depths are skewed with respect to the ridge axis trend and orientation of plate divergence, respectively (Toomey et al., 2007), suggesting flow is not solely responding to local plate divergence. A similar pattern of melt delivery to the base of the oceanic crust and rotated mantle flow field has also been inferred beneath the northern Juan de Fuca (JdF) ridge (VanderBeek et al., 2016). Furthermore, Rayleigh wave imaging of the upper mantle beneath incipient spreading segments in the Gulf of California find circular low seismic velocity zones that are located 10's to 100's of kilometers from the the plate boundary (Wang et al., 2009) and interpretted as convective upwellings. Determining the role of active mantle upwelling in the formation of oceanic lithosphere and the conditions necessary for its development requires continued investigation of upper mantle structure across a diverse sampling of MOR environments.

The recent Cascadia Initiative (CI) experiment (Toomey et al., 2014) provides a new opportunity to explore both across and along-axis variations in MOR dynamics in an intermediate spreading-rate environment. The offshore component of the CI experiment instrumented the entire JdF and Gorda plates with seismometers spaced 50-70 km apart. Similar to the southern EPR, tomographic imaging using teleseismic body (Byrnes et al., 2017) and Rayleigh (Bell et al., 2016) waves recorded by CI stations reveals a strongly

asymmetric region of mantle upwelling. Slow seismic velocities beneath the ridge transition to faster velocities beneath the JdF interior too rapidly to be explained by conductive cooling alone and researchers have invoked dynamic downwelling that abruptly solidifies regions of partial melt (Bell et al., 2016; Byrnes et al., 2017). The analysis of teleseismic body wave delay times and attenuation lead Eilon and Abers (2017) to propose a layered upwelling model for the JdF ridge. Motivated by the abrupt transition from a slow, highly attenuating axial region to a relatively fast, low attenuating plate interior and the present knowledge of mantle mineral physics, Eilon and Abers (2017) hypothesize a broad zone of deep (120 - 180 km) carbonated melting (Dasgupta et al., 2013) where melt fractions are < 0.01% and shear wave velocities (β) are reduced by ~0.1 km/s. Narrow buoyant upwelling occurs within the upper 60-180 km and result in low degrees of water-assisted melting between 60-120 km depth that also reduce β by ~0.1 km/s. Upon the removal of water at ~60 km depth, mantle viscosity may increase by many orders of magnitude (Hirth & Kohlstedt, 1996) inhibiting buoyant upwelling and give rise to a passive upwelling regime. Here, melt fractions increase toward the ridge axis and may vary between 0.2-2% reducing β by up to ~0.7 km/s.

While the model of Elion and Abers (2017) is consistent with the available constraints on mantle structure beneath the JdF plate it is non-unique and the details of mantle upwelling beneath the JdF ridge remain unclear. This is due to resolution issues inherent to the seismic imaging methods employed. The poor vertical resolution of body wave tomography results in uncertainty in the maximum depth extent of the axial low-velocity zone and the depth at which the inferred mantle downwelling occurs off-axis. Furthermore, teleseismic body waves only resolve relative velocity variations which

introduces greater uncertainty in inferring physical properties. By comparison, teleseismic Rayleigh wave images have better depth resolution and constrain absolute velocities but the long periods used in their construction result in poor lateral resolution that decays with increasing depth. Consequently, the relationship between the shallow (<75 km) axial low velocity imaged by Rayleigh waves to deeper earth structure and the presence of strong ridge-normal gradients in mantle velocity at depth are poorly constrained. The limitations of one of these imaging methods are the strengths of the other. In Chapter 5, I describe a methodology for the joint inversion of teleseismic Rayleigh and shear waves to generate higher resolution images of mantle dynamics offshore Cascadia. The depth sensitivity of surface waves combined with the superior lateral resolution of body waves will better constrain depth variations in, and off-axis evolution of, β structure. The improved images will allow a more rigorous assessment of models for MOR dynamics.

2.0 Comparison of Seismic Images

Before considering a joint analysis of different seismic phases, it is instructive to compare independently derived velocity models to highlight the discrepancies between solutions that may be resolved by integrating datasets. While a number of seismic imaging studies using CI data have been conducted (Tian et al., 2013; Gao, 2016; Hawley et al., 2016; Bodmer et al., 2018), I focus on the shear velocity models obtained from teleseismic shear (Byrnes et al., 2017) and Rayleigh (Bell et al., 2016) wave inversion (referred to as the Byrnes and Bell models, respectively). The complimentary sensitivities of these seismic phases to β structure holds promise for constructing higher resolution models through a joint analysis.

In Figure 1, I compare vertically averaged β anomalies recovered in the Byrnes and Bell models. The S-wave delays from Byrnes et al. (2017) have been re-inverted for β structure using the 3D starting model from Bell et al. (2016) to allow equal comparison (Figure 2a). The starting model was derived by converting temperatures predicted from a half-space cooling model to β following (Harmon et al., 2009) and accounts for both anharmonic and anelastic effects. The first-order structure of the two models are the same; a fast JdF plate interior abruptly transitions to relatively slower axial velocities more rapidly than can be explained by a half-space cooling model and the trend of this transition is rotated with respect to the ridge axis. As can be seen in cross-section (Figure 2; Profile location shown in Figure 1a), this structure persists throughout the upper 200 km of the body wave model where β changes on average by ~4% over ~100 km. A similarly strong gradient in β anomalies is observed in the upper ~50 km of the Bell model (Figure 1b and 2c) where upper mantle velocities increase away from the plate boundary by 5-8%. However, no ridge low-velocity anomalies are present. We note that the Bell model was constructed using fundamental mode Rayleigh waves with periods between 20 s and 125 s providing sensitivity to structure shallower than ~200 km depth. Therefore, the limited depth extent of the shallow velocity heterogeneity may not be entirely attributed to differences in depth resolution. Though the lateral variation in β in both models are similar, particularly at shallow depths, the body and Rayleigh wave models cannot be reconciled by simply shifting the mean of the body wave anomalies. The thinner and larger magnitude high-velocity perturbations in the Bell model are not sufficient to explain the body wave delay times. In Figure 3, I compare the mean S-wave station delays as measured by Byrnes et al. (2017) to those predicted through the Bell

model. The delays are adjusted for sediment thickness beneath each station. The predicted travel-time delays exhibit a similar spatial variation to those measured but the magnitude of this variation is under-predicted by approximately half.

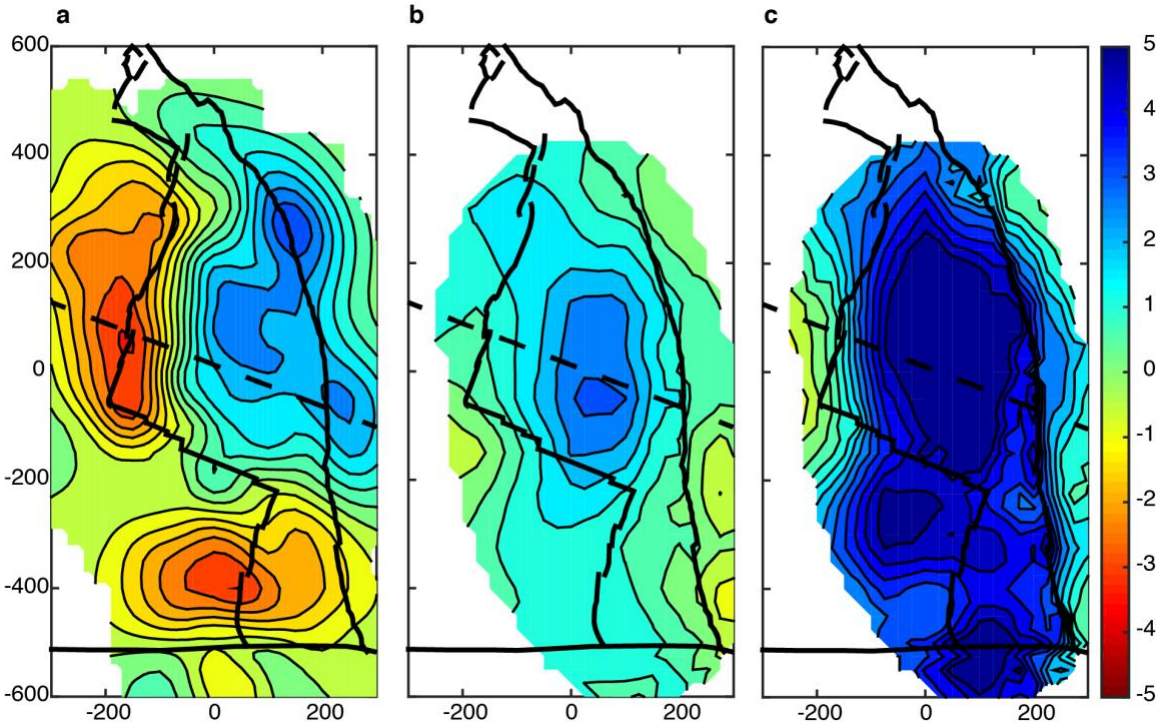

Figure 1: Shear wave velocity perturbations (%) beneath Cascadia as measured by teleseismic (a) S-waves (Byrnes et al., 2017) and (b-c) Rayleigh waves (Bell et al. 2016). Perturbations in a and b are averaged over the upper 200 km of the mantle. Panel c shows the average perturbations in the upper 50 km of the mantle as imaged by Rayleigh waves. Solid lines show the plate boundary. Dashed line identifies position of cross-sections shown in Figure 2.

The preceding comparison of body and Rayleigh wave derived β structure raises a number of questions concerning mantle processes beneath the JdF ridge. Over what depth interval does melting occur? Is melt present throughout the upper ~200 km as suggested by body wave analysis (Byrnes et al., 2017; Eilon & Abers, 2017) or restricted to a shallower asymmetric upwelling zone suggested by the surface wave imaging (Bell et al., 2016)? Does the large velocity gradient east of the ridge reflect active mantle downwelling? How does the magnitude of this velocity gradient vary with depth? The discrepancies between models may also offer insights into heterogeneity in seismic

anisotropy. The near vertically traveling teleseismic S-waves primarily reflect horizontally polarized shear velocity while Rayleigh waves are sensitive to vertically polarized shear velocity. Thus, differences between these models may reflect regional variations in the dip and azimuth of mantle anisotropy. For example, the deep axial low-velocity zone in the Byrnes model may appear slow relative to off-axis velocities if upwelling aligns the seismically fast-axis of olivine vertically beneath the plate boundary and mantle shear induced by the motion of the overlying plate aligns olivine fast-axes parallel to the horizontal plane beneath the plate interior. Frequency dependent attenuation (e.g., Yang et al., 2007; Eilon & Abers, 2017) may also generate inconsistencies between models. The longer period (20-125 s) Rayleigh waves relative to the shorter period (10 s) teleseismc S-waves may experience greater attenuation resulting in a frequency-dependent relationship between β and temperature (e.g., Stixrude & Lithgow-Bertello, 2005). While the the joint analysis of shear and Rayleigh waves may yield higher resolution images of upper mantle isotropic structure, identifying inconsistencies between these datasets can provide additional insights into the physical state of the upper mantle. In developing a joint inversion strategy, I begin by reviewing the data processing and equations relevant to the independent analysis of teleseismic body and surface waves.

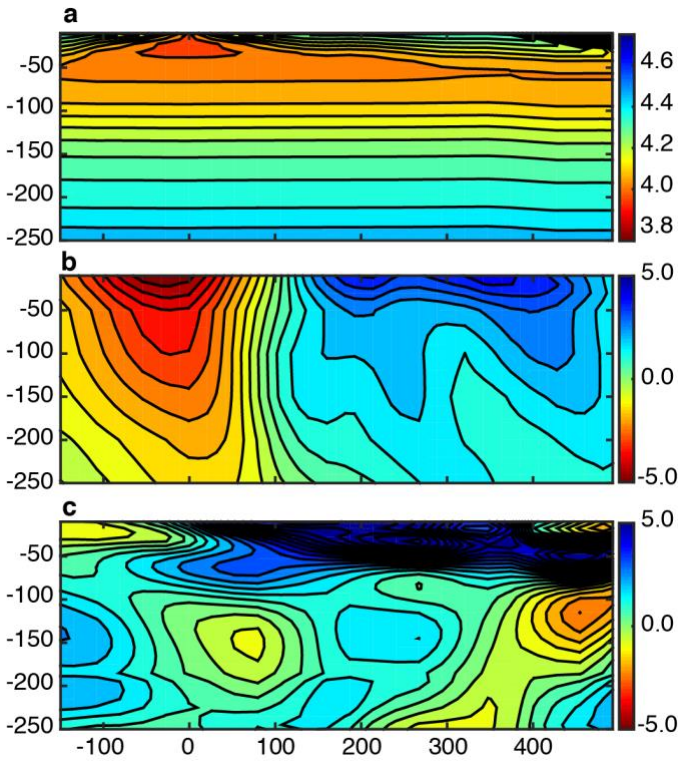

Figure 2: Cross sections through (a) the starting velocity model, (b) S-wave perturbational model, and (c) Rayleigh wave perturbational model along profile line shown in Figure 1. Percent perturbations are plotted with respect to model in a. The location of the JdF ridge is located at x = 0 km.

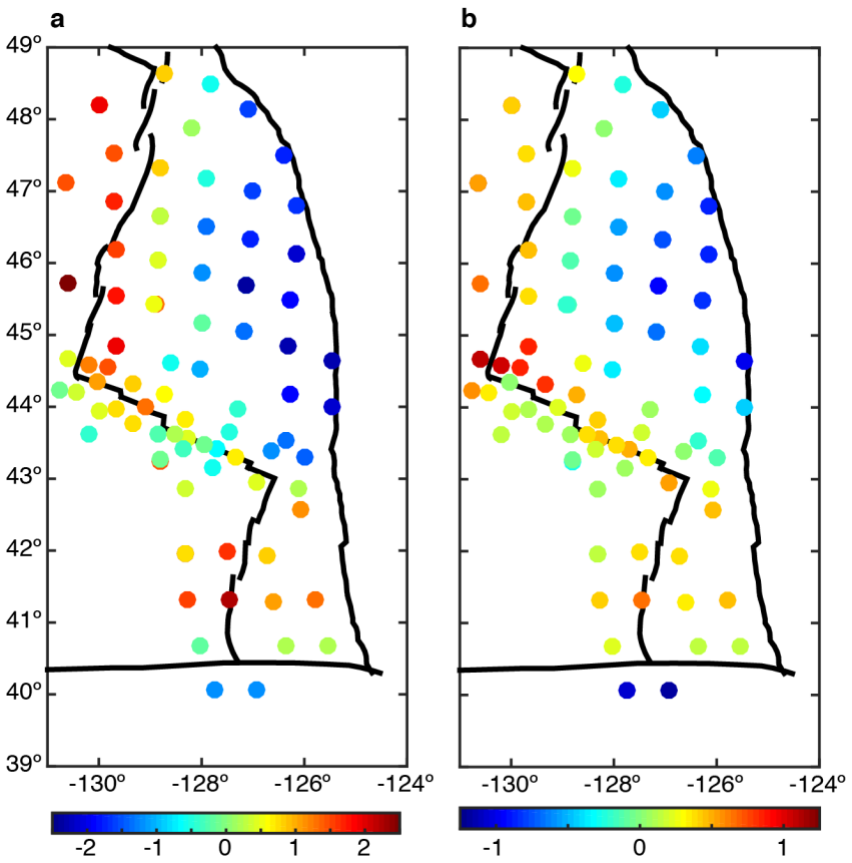

Figure 3: Mean station delays (a) measured by Byrnes et al. (2017) and (b) predicted through the shear wave velocity model of Bell et al. (2016). Predicted sediment delays beneath each station have been removed. Note the change in scale between a and b.

3.0 Body Wave Tomography

The inversion for seismic velocity variations from teleseismic body waves recorded by a regional seismic network begins with the measurement of relative arrival times (t). These are commonly obtained via the method of Vandecar and Crosson (1990) which involves computing the arrival time differences between station pairs for a single event through waveform cross-correlation and then solving for a set of relative arrival times. Explicitly, the difference in arrival between the ath and bth stations (d_{ab}) is given by

$$d_{ab} = t_a^p - t_b^p - \tau_{ab} \qquad (1)$$

where $t_{a,b}^{p}$ is a predicted arrival time, typically estimated from a radial earth velocity model but may also be an analyst pick, and τ_{ab} is the cross-correlation derived delay time between the ath and bth stations after aligning waveforms on their predicted arrival times. An estimate of the relative arrival times at each station for a given event is obtained by solving the following system of equations

$$t_a - t_b = d_{ab} \tag{2}$$

$$\sum_{a=1}^{N} t_a = 0 \tag{3}$$

Equation 3 forces the mean of the relative arrival times to zero and the sum is over the N stations that recorded the event. The zero-mean constraint removes the source origin time from the data. Thus, the relative arrival times are effectively relative travel-time variations.

A velocity model that explains the observed relative travel-times is found by minimizing the difference between observed and predicted data. The predicted travel-times are estimated using ray theory and Dijkstra's algorithm is used to find the shortest path through a model space discretized in terms of slowness (i.e. the inverse of velocity; Dijkstra, 1959; Moser, 1991). For teleseismic rays, the computation of travel-times proceeds in two steps. First, times to the edge of the imaging volume are calculated using a radial earth model. Next, travel-times are calculated from a single station to the model boundaries. The ray entry point is taken as the location on the model boundary where the sum of these to travel-time fields is at a minimum. Dijkstra's algorithm is used to find the shortest path between the entry point and a station. The predicted travel-time ($\tilde{t}$) is defined as

$$\tilde{t} = \tilde{t}^{1D} + \int_p u \, dp \tag{4}$$

where $\tilde{t}^{1D}$ is the travel-time through a radial earth model to the edge of the imaging volume; u is slowness, and the integral is over the discretized 3D ray path. As with the observed data, the predicted travel-times are demeaned for each event. Note that the resulting set of relative travel-time residuals, $\Delta t = t - \tilde{t}$, will have zero mean. Therefore, these data will tend to construct an image containing perturbations that also have a zero mean.

The travel-time residuals are inverted for slowness perturbations with respect to the starting model and station and event static terms. This amounts to solving the following system of equations which is typically under-determined and ill-posed,

$$\Delta t_{ij} = \frac{\partial t_{ij}}{\partial u_k} \Delta u_k + \Delta g_j + \Delta e_i \tag{5}$$

where Δt_{ij} is the relative travel-time residual for the ith event recorded by the jth station; Δu_k is the perturbation to the kth model node; Δg_j and Δe_i are station and event static perturbations, respectively. The partial derivative $\frac{\partial t_{ij}}{\partial u_k}$ is simply a weighted fraction of the ray path influenced by the kth slowness parameter. Under a ray theoretical (infinite frequency) approximation, $\frac{\partial t_{ij}}{\partial u_k}$ is non-zero only for slowness parameters along the ray path. However, the delay times measured via cross-correlation of finite-frequency waveforms are sensitive to velocity heterogeneity in a volume around the theoretical ray path (Marquering et al., 1999; Dahlen et al., 2000). Calculation of these sensitivity kernels is computationally demanding. Schmandt and Humphreys (2010) provide an efficient approximation for their estimation, namely

$$K^b \propto \sin\left(\pi\left[\frac{x_n}{R_F(x_p,\omega,D)}\right]^2\right) \quad (6)$$

where x_n is the ray-normal distance to a model node and R_F is the radius of the first Fresnel zone which varies as a function of distance along the ray measured from the station (x_p), frequency (ω), and epicentral distance (D). The value of R_F can be computed from the travel-time field and includes all potential propagation paths that yield travel-times that are within a quarter period of the shortest path (Spetzler & Snieder, 2001). The partial derivative $\frac{\partial t_{ij}}{\partial u_k}$ may be written,

$$\frac{\partial t_{ij}}{\partial u_k} = -K_k^b u_k^{-1} dx^3 \quad (7)$$

where K_k^b is the value of the sensitivity kernel at the kth model node and dx^3 is the volume represented by that model node. Figure 4a illustrates the approximate normalized sensitivity of a 10 s S-wave recorded at a distance of 90° to velocity heterogeneity. It is important to note that the finite-frequency sensitivity kernels are generally only implemented in the inverse problem in which case they effectively act as physically based smoothing constraints that help to regularize the inversion.

4.0 Rayleigh Wave Tomography

In contrast to body waves, surface waves travel laterally across an array and frequency-dependent phase delays between stations may be used to constrain absolute propagation velocities. The propagation velocity is a function of the compressional and shear wave speeds and density of the medium. Because surface waves are dispersive, the propagation velocity varies with frequency with lower frequencies being sensitive to structure at greater depths. These properties make surface wave tomography a valuable tool for constraining depth variations in the absolute velocity structure of the earth. I

briefly summarize the analysis of fundemental mode Rayleigh waves for the construction of phase velocity maps and then present the equations used to convert between phase and shear velocity.

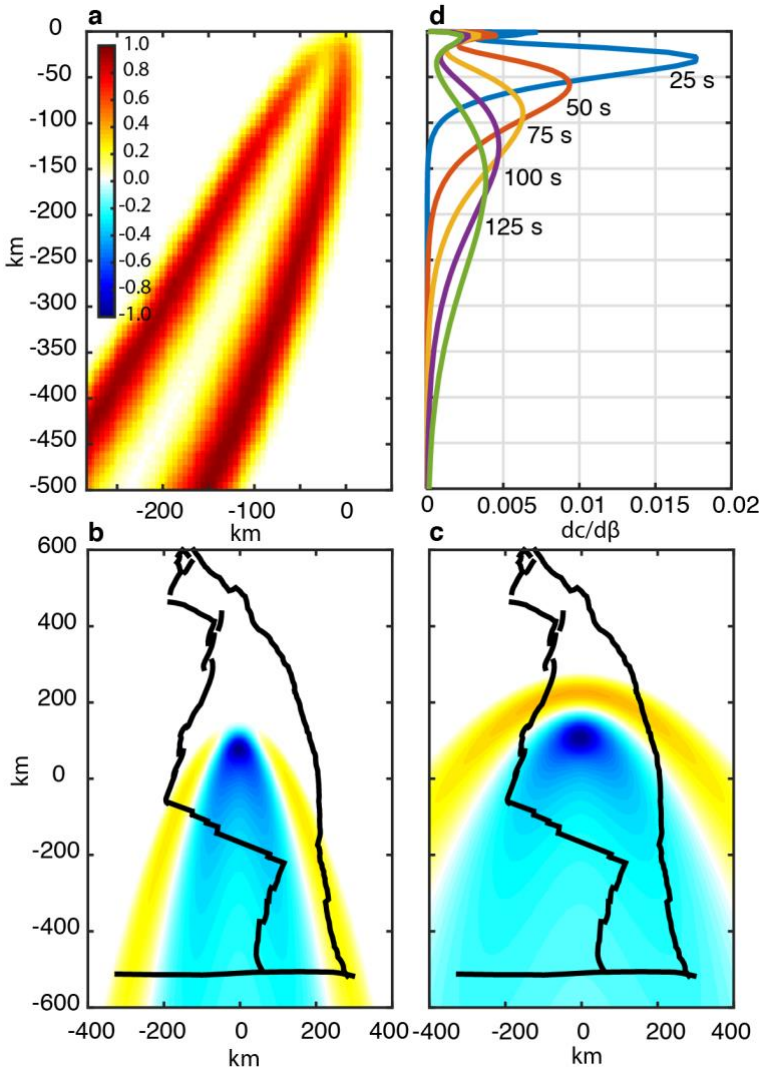

Figure 4: Comparison of approximate sensitivity kernels used in tomography. (a) Normalized sensitivity kernel for a 10 s S-wave recorded at a distance of 90°. Normalized phase sensitivity kernels to phase velocity heterogeneity for a (b) 25 s and (c) 100 s northward propagating Rayleigh wave with the JdF plate boundary shown for scale; colorscale in a. (d) 1D shear wave velocity sensitivity kernels for fundamental mode Rayleigh waves at periods between 25 s and 100 s.

A common approach to the analysis of surface waves is the two-plane wave method described by Forsyth and Li (2005). Teleseismic surface waves propagating

across a regional array are approximated as the sum of two plane waves with back azimuths that may deviate from the great-circle path adjoining the source and a receiver. The two-plane wave method approximates interference due to energy scattered along the propagation path (i.e. multipathing). The data measured are the phase and amplitude of windowed and narrow band filtered surface waves recorded across the seismic array for a given event. A solution for the amplitude, phase, and azimuth of the two plane waves that best fits the displacement estimated from the measured amplitude and phase is sought for each event. Variations in phase across the array depend upon the phase velocity along the propagation path. Thus, the best-fit solution produces maps of absolute phase velocity for each frequency band measured. Owing to the finite frequency content of the observations, perturbations in both the amplitude and phase reflect phase velocity heterogeneities in an area surrounding the propagation path (Zhou et al., 2004). To illustrate the lateral sensitivity of a teleseismic Rayleigh wave, I plot the phase sensitivity kernels for a 25 s and 100 s plane wave using the approximation of Yang and Forsyth (2006) in Figure 4b and 4c. Because of their long periods, teleseismic Rayleigh waves have a much broader region of sensitivity compared to body waves (Figure 4a). Greater uncertainty in phase measurements and broadening of the sensitivity kernels with increasing period limits the lateral resolution of regional-scale phase velocity heterogeneity (Yang & Forsyth, 2006).

The inversion of Rayleigh wave phase and amplitude data results in the construction of phase velocity maps at each period of observation. To convert the 2D phase velocity maps to a 3D model of shear wave velocity, a third inversion is required that relates these two parameters. This is often carried out as a series of 1D inversion for vertical β profiles which may be coupled through smoothing constraints (e.g.,

Villagomez et al., 2007). At a given coordinate within the 2D phase velocity map, a perturbation in phase velocity (Δc) at a specific frequency (ω) is linearly related to perturbations in compressional (α) and shear velocity and density (ρ) as a function of depth (z),

$$\Delta c(\omega) = \sum_{l=1}^{nz} h_l \left[\frac{\partial c(\omega)}{\partial \alpha(z_l)} \Delta\alpha(z_l) + \frac{\partial c(\omega)}{\partial \beta(z_l)} \Delta\beta(z_l) + \frac{\partial c(\omega)}{\partial \rho(z_l)} \Delta\rho(z_l) \right]. \quad (8)$$

Above, nz is the number of layers and h_l is their thickness. At the periods of interests (> 10 s), Rayleigh wave phase velocities are primarily sensitive to β. The sensitivity to ρ is approximatley an order of magnitude smaller than the sensitivity to β; the dependence on α can be compareable to β at shallow depths. An often used approximation to Equation 8 is

$$\Delta c(\omega) \approx \sum_{l=1}^{nz} h_l \left[\frac{\partial c(\omega)}{\partial \alpha(z_l)} \upsilon + \frac{\partial c(\omega)}{\partial \beta(z_l)} \right] \Delta\beta(z_l) \quad (9)$$

where υ is the ratio of α to β. The partial derivatives in Equations 8 and 9 are predicted using software that calulates normal model solutions for laterally homogeneous media (e.g., Saito, 1988). One-dimensional shear velocity sensitivity kernels for Rayleigh waves at periods between 25 s and 125 s are shown in Figure 4d. The peak depth sensitivity to β anomalies varies with period allowing vertical variations in β to be resolved. This is contrast to the relatively poor depth resolution of teleseismic body waves caused by their near vertical propagation paths (Figure 4a). The system of equations in Equation 9 is underdetermined and regularized by including additional equations that penalize the norm and roughness of the perturbations.

5.0 A Joint Inversion Approach

There are two general approaches to the joint analysis of body and surface wave data for 3D shear velocity structure. One method imposes the phase velocity observations as a constraint on the body wave tomography problem (e.g., Obrebski et al., 2011; Villagomez et al., 2014). The other approach uses the phase velocity maps to predict surface wave travel-times across an array. These predicted surface wave travel-times are then jointly inverted with body wave arrival times for shear wave slowness (e.g., West et al., 2004; Golos et al., 2018). I consider the simpler approach of inverting phase velocity observations with relative travel-times.

The joint inversion amounts to finding the best-fit solution to Equations 5 and 9. The data are the phase velocity maps and teleseismc relative travel-time observations. The inversion requires the parameterization of three models. A 3D ray tracing model is defined in terms of shear wave slowness (u) and is used to predict teleseismic travel-times. A 3D model of α, β, and ρ is defined on the same lateral grid as the phase velocity observations and is used to predict phase velocities and 1D sensitivity kernals. Because the phase velocities and their sensitivity kernels depend upon the details of shallow structure, a finer node spacing is used near the surface. The third model is the β perturbational model through which the surface wave and body wave models are coupled.

To yield a consistent parameterization, Equation 9 is redefined as a function of u by scaling it by $-u\beta^2$. Additional scaling of Equations 5 and 9 is required to account for differences between the number of observations and variance of the two datasets. I weight the equations according to,

$$w_n^B = \frac{p}{N\sigma_n^B};\ w_m^{SW} = \frac{(1-p)}{M\sigma_m^{SW}} \tag{10}$$

where w_n^B and w_m^{SW} are the weights applied to nth and mth equations relating travel-time and phase velocity residuals to model parameters, respectively; N and M are the total number of body and surface wave observations; $\sigma_{n,m}^{B,SW}$ is the estimated error for each observation, and p controls the relative weight between body and surface data. The linear system of equations relating data residuals to model parameters may be written as

$$\begin{bmatrix} \boldsymbol{W}^B \boldsymbol{G} \\ \boldsymbol{W}^{SW} \boldsymbol{A} \end{bmatrix} [\Delta m] = \begin{bmatrix} \boldsymbol{W}^B \Delta t \\ \boldsymbol{W}^{SW} \Delta c \end{bmatrix} \tag{11}$$

where $\boldsymbol{G}$ and $\boldsymbol{A}$ are partial derivative matrices obtained from Equations 5 and 9, respectively; Δm is the model perturbational vector; $\boldsymbol{W}^B$ and $\boldsymbol{W}^{SW}$ are matrices whose diagonals are given by the weights in Equation 10; Δt and Δc are vectors containing the travel-time and phase velocity residuals, respectively. Additional smoothing and damping constraints are added to the above system following Toomey et al. (1994) and a solution is found using the LSQR algorithm (Paige & Saunders, 1982). The resulting perturbations are applied to the body and surface wave models and additional iterations are performed until a convergence criteria is reached.

6.0 Synthetic Test

I use a synthetic experiment to demonstrate the improved resolution of the joint inversion strategy discussed in Section 5.0. I construct a mid-ocean ridge shear wave velocity model derived from temperatures predicted from a half-space cooling model following Harmon and Forsyth (2009). To this base model I add four velocity anomalies (Figure 5a). Two broad shallow zones defined by a 6% and 4% velocity reduction are added to represent a broad triangular dry melting region with greater melt retention at

shallow depths. Centered beneath the ridge is a narrower 100 km-wide region of 2% velocity reduction which represents a zone of focused upwelling that extends to 125 km depth. This anomaly is flanked by two 2% high velocity features meant to represent an abrupt increase in velocity due to downwelling. A 200 km-wide region of 2% velocity reduction extends from 125 to 200 km depth and represents a deep melting region. The synthetic model geometry is inspired by the conceptual model for the JdF ridge presented by Eilon and Abers (2017).

Travel-times and phase velocities are predicted for the sythetic model geometry.

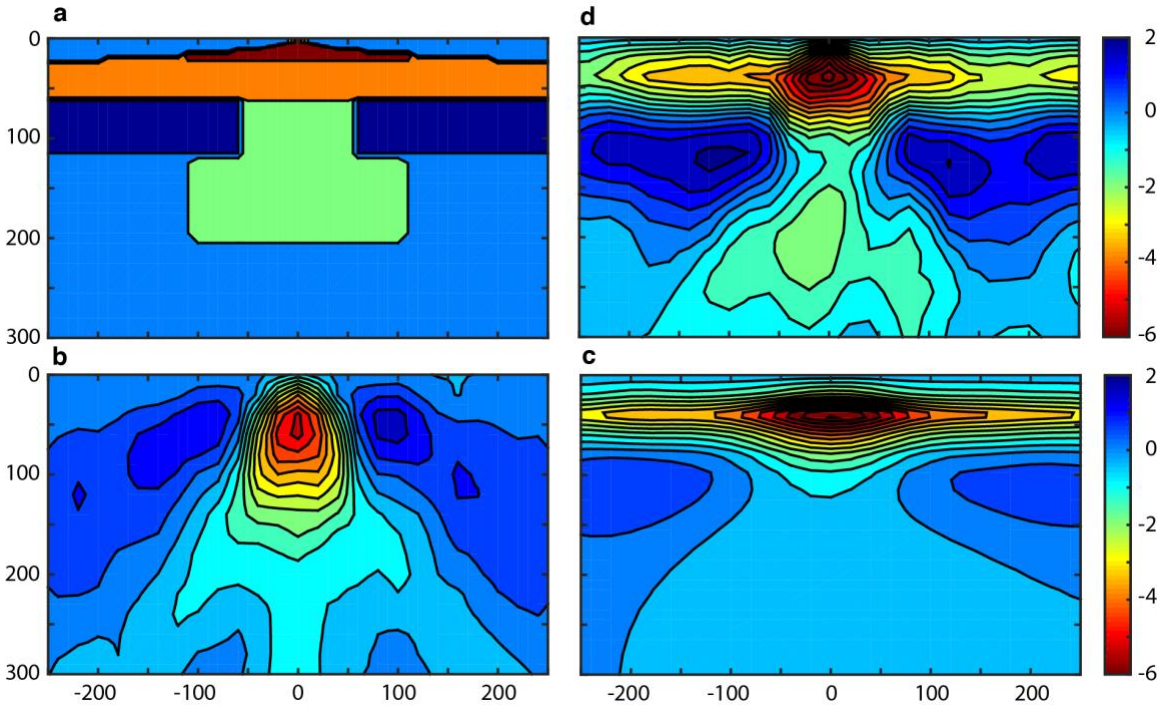

Figure 5: Synthetic inversion results. (a) The true distribution of shear wave velocity anomalies. The anomalies recovered by the inversion of synthetic S-wave delay times only and surface wave phase velocities only are shown in b and c, respectively. Results from the joint inversion of both datasets are shown in d. Color scale is in percent.

Stations recording synthetic teleseismic events are spaced every 50 km. The 100 synthetic events used are randomly distributed in azimuth and distance (range between 35° and 120°). Phase velocity maps are generated for 15 periods between 20 s and 125 s and are the same as those considered by Bell et al. (2016); the S-wave arrivals are

prescribed a central period of 10 s. Random errors drawn from normal distributions with standard deviations of 250 ms and 0.04 km/s are added to the predicted travel-times and phase velocities, respectively. These errors are comprable to those estimated in the studies of Bell et al. (2016) and Byrnes et al. (2017). To mimick the reduction in lateral resultion with increasing period, the phase velocity maps are smoothed with a Gaussian filter whose characteristic length is $0.25T\bar{C}(T)$ where $\bar{C}(T)$ is the mean phase velocity at period T. These data are inverted independently and jointly using the base model described above as a starting model. The perturbational model for all synthetic inversions had 20 km node spacing in the x-, y-, and z-directions. The weighting parameter in Equation 10 for the joint inversion is defined as 0.5.

The results of the synthetic tests are shown in Figure 5. The body wave-only results (Figure 5b) capture the narrowness of the deeper low velocity region with an amplitude that reflects the average of the low velocity zones beneath the ridge. Because the travel-time data only contain information on relative changes in velocity structure, the shallower and broader low velocity zone cannot be resolved. In comparison, the phase velocity-only results (Figure 5c) capture the shallow and broad low velocity feature and the average decrease in shallow velocity nearer the spreading center. While there is some resolution of the high velocity anomalies, the geometry of the deeper structure remains largely unresolved. As expected, the joint inversion yields the model that is most true to the input structure and captures the main features of the synthetic anomlies (Figure 5d). However, vertical smoothing causes the anomalies to appear slightly broader in depth. Using a perturbational model with finer vertical node spacing at shallow depths, where the Rayleigh wave sensitivity kernels are narrower, may help to resolve this issue.

7.0 Summary

Preliminary tests of jointly inverting body wave relative travel-times and Rayleigh wave phase velocities holds promise for improved imaging of mantle dynamics offshore Cascadia. If the geometry of mantle upwelling varies with depth beneath spreading centers, as has been recently proposed for the JdF ridge, body or surface wave tomography alone provides an incomplete image of mantle structure. Future work will more fully explore perturbational model parameterization and data weighting using synthetic data and models that reflect the CI experiment geometry. Following these synthetic tests, I will construct new seismic velocity models for offshore Cascadia by jointly inverting existing S-wave and Rayleigh wave datasets.

CHAPTER VI

CONCLUSION

This dissertation explored the evolution of the oceanic upper mantle from accretion to subduction within a single tectonic plate system. Seismic data collected across the JdF and Gorda plates has allowed me to construct the first images of the mantle axial magmatic system at an intermediate-spreading rate ridge segment and place new constraints on the scale of heterogeneity in the uppermost mantle. These results provide new perspectives on the geometry of mantle flow and plate accretionary processes beneath mid-ocean ridges and the structure of oceanic lithosphere. Beneath the northern JdF ridge, plate and mantle divergence directions were found to be misaligned with the orientation of mantle flow rotated ahead of recent changes in plate motion. A comparison with observations from other mid-ocean ridge segments suggests a similar pattern may be present globally. This lead to the speculation that stresses transmitted to the base of the lithosphere by oblique mantle flow may be a driving force for changes in plate motion and the formation of new spreading segments. Surficial indicators of magma supply along oceanic ridge segments were found to be anti-correlated with the volume of mantle melt present near the Moho. These observations indicate that the dynamics of rifting rather than mantle upwelling control along strike changes in crustal thickness, composition, and vigor of volcanic processes. Contrary to the common assumption that seismic anisotropy in the oceanic lithosphere reflects the frozen in signal of deformation at the Ridge, the JdF plate shows evidence that ductile deformation at near-Moho depths continues away from the plate boundary and acts to reorient mantle fabrics. Because the

anisotropy develops in response to viscous deformation, this result has implications for the rheologic evolution of young lithospheric mantle. Seismic velocity images of the JdF and Gorda mantle lithosphere demonstrate that faulting at the surface does not necessarily translate into deformation and alteration at sub-Moho depths. Mantle velocities beneath the extensively faulted and fragmenting Gorda plate exhibit an age-dependence that is remarkably consistent with predictions from a half-space cooling model. In contrast, JdF mantle velocities deviate notably from a simple cooling trend. Thus, along-strike variations in the physical state of the subducting slab cannot be interpreted from surface morphology on the incoming plate alone.

In all, this work highlights gaps in our understanding of lithosphere-asthenosphere dynamics and the need for continued exploration of the Earth's ocean basins. There exist a number of outstanding questions. What is the larger-scale pattern of mantle convection beneath oceanic plates and what is its influence on the evolution of the lithosphere? Why do seismic measures of mantle flow yield discrepancies between the motion of the lithosphere and asthenosphere? While the accumulation of melts beneath oceanic spreading centers may be explained via the thermal structure imposed by the rifting geometry, how are these shallow axial magmatic systems connected to the deeper melt production region? To address these questions, future work is aimed at integrating seismic datasets to improve images of Earth structure.

APPENDIX A

CHAPTER II SUPPORTING INFORMATION

Data and starting model

We use the arrival times of mantle refractions (Pn) that undershoot the ridge axis to tomographically image the uppermost mantle. These data are picked on the outermost shot lines and ocean-bottom seismometers (OBSs; each instrument is equipped with three orthogonal geophones and a hydrophone) that make up the Endeavour Tomography (ETOMO) experiment (Figure S1). The *R/V Marcus G. Langseth's* well-tuned airgun array provided an impulsive seismic source that allows us to pick Pn travel-times with low uncertainty. To further enhance data quality, we summed the vertical and hydrophone channels where good quality data was recorded on both components. A total of 5,528 handpicked Pn arrivals with a mean standard deviation of 11 ms are included in our tomographic inversion. The uncertainties were estimated visually based on the impulsiveness of the Pn arrival and the trace-to-trace coherency of waveforms. Additional sources of error affecting travel-time picks include source and receiver location uncertainties, instrument clock corrections, and uncertainties in bathymetry. These experimental errors are typically smaller than the picking error (Weekly et al., 2014; Barclay et al., 1998). To ensure only mantle refractions are included in our dataset, we only include picks with source-receiver offsets greater than 40 km. Figure S2 shows Pn arrivals and travel-time picks from the shot line and OBS identified in Figure S1.

Previous tomographic analysis of 96,156 crustal refractions (Pg; Weekly et al., 2014) and 22,577 Moho reflections (PmP; Soule et al., 2016) provides a 3D starting model of crustal velocity and thickness. These studies incorporated data from both the outer-most experimental grid and a denser grid of airgun shots and OBSs centred along the ridge axis (Figure S1). As a result, structure along the crustal legs of Pn ray paths is well constrained (Figure S3) and variations in Pn travel-times largely reflect mantle structure (Zhang et al., 2007).

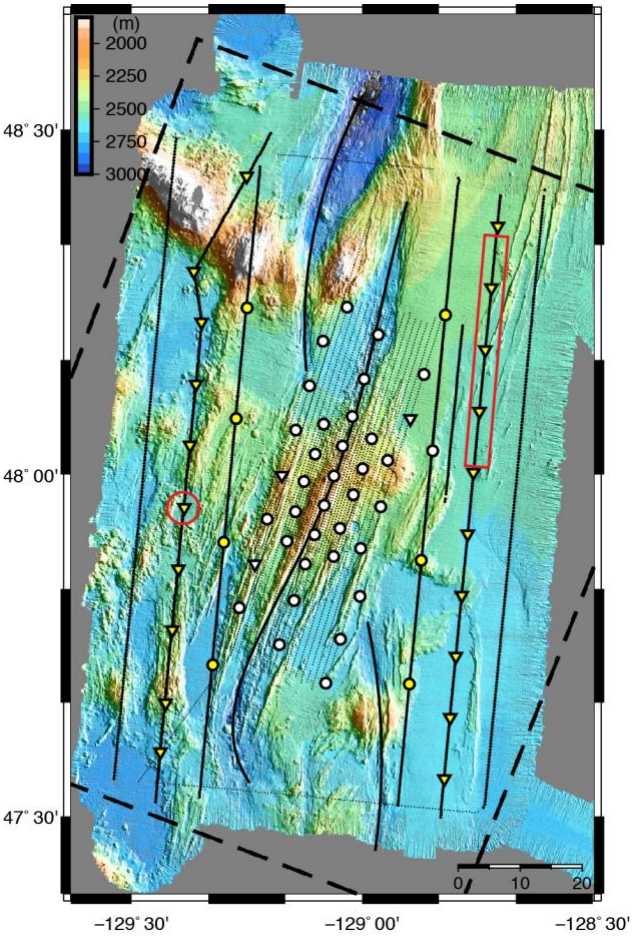

Figure S1. ETOMO experiment geometry and Endeavour ridge bathymetry. During the ETOMO experiment, 68 OBSs from the U.S. Ocean Bottom Seismograph Instrument Pool were deployed at 64 sites (triangles and circles identify instruments operated by Scripps Institution of Oceanography and Woods Hole Oceanographic Institution, respectively). Each instrument recorded over 5500 airgun shots from the 36-element, 6600-cubic-inch airgun array of the *R/V Marcus G. Langseth*, fired at intervals of 450 m (~210 s) along track lines (black dots). The bathymetry shown is that collected during the cruise with the R/V Marcus G. Langseth's EM122 multibeam system. The mantle structure is imaged using a subset of the OBSs (filled yellow symbols) and airgun shots (bold black points). The OBS and events for which waveforms are shown in Figure S2 are identified by the red circle and red rectangle, respectively. The dashed black line shows the map-view extent of the rectangular inversion volume. The thin black line identifies the Pacific-Juan de Fuca plate boundary.

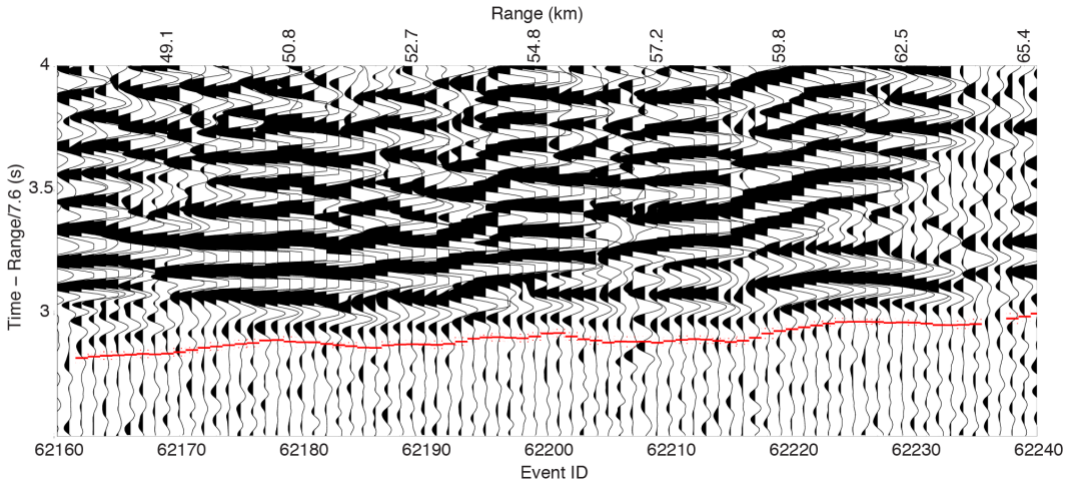

Figure S2. Example record section with Pn waveforms and travel-time picks. The Pn phase is identified (red bars with dotted lines show the travel-time picks and associated 1σ uncertainty) at shot-station offsets greater than 40 km. The station and events for which the waveforms are shown are identified in Figure S1. The data recorded on the vertical and hydrophone channels are stacked and band-pass filtered between 3 and 15 Hz and a reduction velocity of 7.6 km/s is applied.

Azimuthal anisotropy

We use azimuthal variations in Pn travel-time residuals to identify the segment-scale anisotropic structure. Weak upper mantle anisotropy is well-approximated by a hexagonal symmetry system with an axis of symmetry (the fast direction of P-wave propagation) oriented sub-parallel to the horizontal plane (Nicolas & Christensen, 1987; Becker et al., 2006). Under this approximation, P-wave velocity varies azimuthally as a periodic function of 2θ and 4θ terms,

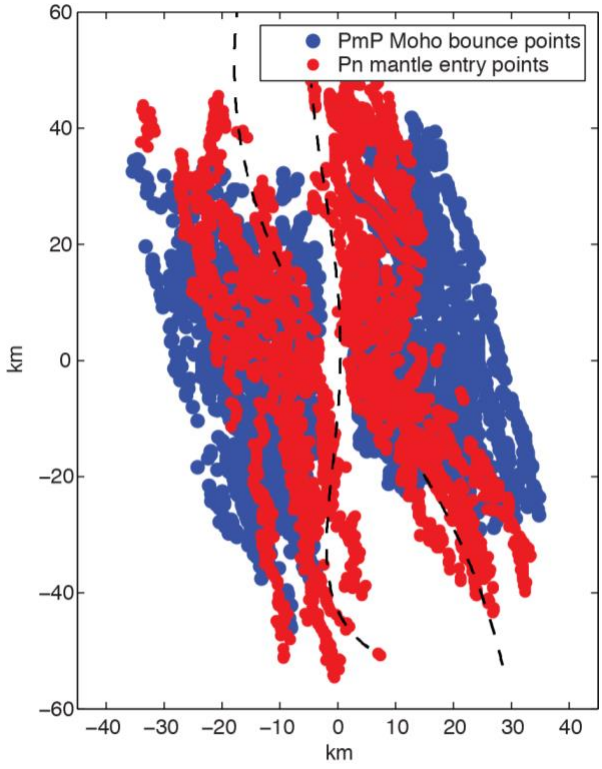

Figure S3. Crustal thickness constraints at Pn mantle entry points. Comparison of PmP Moho bounce points (blue dots; Soule et al., 2016) and Pn mantle entry points (red dots) shows that crustal thickness is well constrained along the crustal legs of Pn ray paths. The plate boundary is shown by the dashed black line.

where θ is the source-receiver azimuth with respect to the spreading direction (Backus, 1965; Shearer & Orcutt, 1986). Assuming a homogeneous mantle anisotropic structure, this gives rise to a sinusoidal pattern in arrival time delays (Δt), which can be parameterized as follows:

$$\Delta t = \alpha_0 + \alpha_1 \cos(2\theta) + \alpha_2 \sin(2\theta) + \alpha_3 \cos(4\theta) + \alpha_4 \sin(4\theta)$$

Where α_0 is the mean delay and α_1, α_2, α_3, and α_4 controls the magnitude and orientation of mantle anisotropy. The amplitude (A_n) and phase (ψ_n) of the 2θ ($n = 2$) and 4θ ($n = 4$) terms are defined as follows:

$$A_n = \sqrt{\alpha_{n-1}^2 + \alpha_n^2}$$

$$\psi_n = \text{atan}\left(\frac{\alpha_n}{\alpha_{n-1}}\right)$$

Standard errors (s_z) in the amplitude and phase are estimated using the Gaussian error propagation rule (Taylor, 1994):

$$s_z = \sqrt{\left(\frac{\partial z}{\partial \alpha_1} s_{\alpha_1}\right)^2 + \left(\frac{\partial z}{\partial \alpha_2} s_{\alpha_2}\right)^2}$$

where z is the amplitude or phase. In mantle rocks, the 4θ terms are predicted to be much smaller than the 2θ terms (Shearer & Orcutt, 1986) and so we choose to set α_3 and α_4 to zero. This choice is justified by our data. Attempting to fit all five free parameters does not significantly alter the magnitude or the fast-axis orientation relative to fitting only 2θ terms. This is because the amplitudes of the best-fit 4θ terms are an order of magnitude smaller than the 2θ terms. Furthermore, the standard errors in the α_3 and α_4 parameters are of the same order as the parameter values themselves indicating they are not required to fit our Pn dataset.

We determine the coefficients α_0, α_1, and α_2 using a weighted least-squares fit to the Pn travel-time residuals. Delays are calculated with respect to an isotropic, homogeneous (7.6 km/s) mantle and corrected to a common range (40 km) based on the mantle path length. To reduce the effects of isotropic heterogeneity in our estimate of anisotropy, we bin the Pn delays and fit the mean delay in each bin. Errors in the mean delay of each bin are estimated using a Student's t-test with a 95% confidence interval. These errors are used to weight the least-squares fit.

We made many estimates of anisotropy across a range of bin sizes and data subsets, all of which indicate clockwise rotation in the fast-direction of mantle anisotropy with respect to the plate-spreading direction (110°; Gripp & Gordon, 2002). We present two anisotropic models in Figures S4a-b. The first model includes all 5,528 Pn delays binned at 10° (Figure S4a) and has a best-fit fast-axis orientation of 127° ± 1° and a magnitude of 3.9% ± 0.5%; relative to the plate-spreading direction, the fast-axis is skewed clockwise by 17°. To remove potential complexities associated with the OSCs, where isotropic heterogeneity is particularly pronounced (Chapter II, Figure 2b), a second model is presented (Chapter II, Figure 3 and Figure S4b) in which we removed all Pn delays associated with ray paths that pass beneath overlapping portions of the ridge (a total of 1,232 delays are removed). This second anisotropic model has a best-fit orientation of 122° ± 1° and magnitude of 4.7% ± 0.4%; relative to the plate-spreading direction, the fast-axis is skewed clockwise by 12°. We note that a homogeneous anisotropic structure alone explains greater than 40% of the data variance, indicating that seismic anisotropy is a robust signal in our data. In addition to estimating mantle anisotropy by analysing travel-time delays, we also performed grid-search inversions

over various anisotropic models (see Model Sensitivity). These results are consistent with the anisotropic structure interpreted from azimuthal variations in Pn delays, in particular, the subset of Pn data that does not include paths beneath the OSCs. On the basis of these analyses, we imposed the anisotropic structure presented in Chapter II, Figure 3 and Figure S4b to construct our preferred tomographic solution.

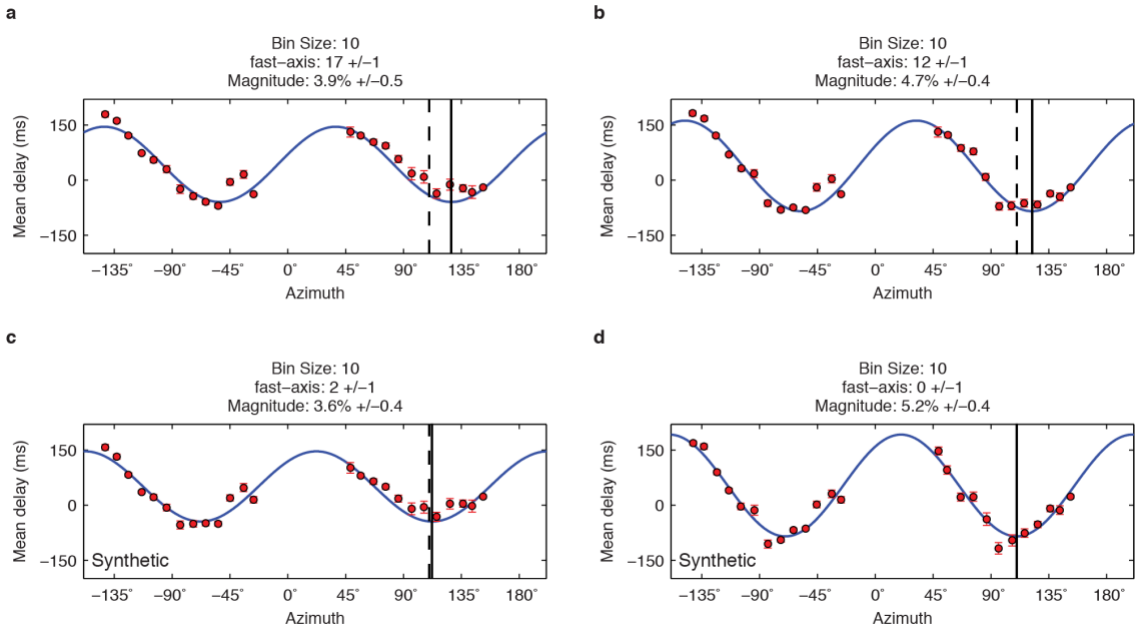

Figure S4. Anisotropic models recovered from measured and synthetic Pn delay times. The mantle seismic anisotropic structure is identified by least-squares fitting a cos2θ-curve (blue line) to mean Pn travel-time delays (red points) as a function of ray azimuth. Error bars show the 95% confidence interval in the mean delay time as determined by a Student's t-test. The best-fit orientation of the seismically fast-axis with respect to the plate-spreading direction (clockwise positive) and the magnitude of anisotropy for each curve are displayed at the top of each plot along with their standard errors. The vertical dashed and solid lines mark the spreading direction (110°; Gripp & Gordon, 2002) and the seismically fast-axis orientation, respectively. We make estimates of the mantle anisotropic structure using (a) all measured Pn delays and (b) a subset of the data in which delays associated with ray paths traveling beneath either OSC are removed. In (c) and (d), we show the recovery of anisotropic models from fitting synthetic Pn delays using the data geometry in (a) and (b), respectively. The synthetic data was calculated for an isotropic mantle structure taken from our preferred solution (Chapter II, Figure 2b) and 4% mantle anisotropy with the fast-axis oriented parallel to the plate-spreading direction (110°).

We also verified that our estimate of anisotropy is not an artefact of the Pn ray geometry or likely heterogeneity in the isotropic structure. To do this we created synthetic Pn travel-times for a model that included our preferred mantle isotropic structure (Chapter II, Figure 2b) and 4% mantle anisotropy with the fast-axis oriented

parallel to the plate-spreading direction (110°; Gripp & Gordon, 2002). Random noise with a standard deviation of 11 ms was added to the synthetic travel-times. We then determined the best-fit anisotropic model following the methods described above. Fitting all synthetic Pn delays, including those that sample the overlapping ridges, the best-fit anisotropic model has a fast-axis orientation of 112° ± 1° and a magnitude of 3.6% ± 0.4% (Figure S4c). The fast-axis orientation is slightly overestimated in the clockwise direction and the magnitude of anisotropy is within the standard error. Fitting only those synthetic Pn delays that travel beneath the non-overlapping sections of the Endeavour segment results in a best-fit fast-axis orientation of 110° ± 1° and magnitude of 5.2% ± 0.4% (Figure S4d). This subset of Pn delays accurately determines the fast-axis orientation but over predicts the magnitude by ~1%. We conclude from these tests that the anisotropic models predicted from fitting Pn travel-time residuals are not significantly influenced by likely heterogeneity in isotropic structure or ray path coverage.

Tomographic Procedure

We use an iterative tomographic technique in which travel-time residuals are inverted for 3D slowness (i.e. inverse of velocity) perturbations (Dunn et al., 2005; Toomey et al., 1994). Ray paths and travel-times are predicted using a shortest path algorithm (Moser, 1991). Ray tracing is performed on a 3D grid parameterized in terms of anisotropic slowness (Dunn et al., 2005) and includes seafloor topography (Toomey et al., 1994). Anisotropic slowness (u) is parameterized assuming a hexagonal symmetry system and is defined as:

$$u(\vec{r}) = \frac{u_{iso}(\vec{r})}{1 + A(\vec{r})\cos[2\theta(\vec{r})] + B(\vec{r})\sin[2\theta(\vec{r})]}$$

where u_{iso} is the isotropic slowness at position $\vec{r}$, θ is the ray azimuth measured from the x-axis, and A and B are scale terms that control the magnitude and orientation of the fast-axis of seismic anisotropy defined as $2\sqrt{A^2 + B^2}$ and $0.5\text{atan}(B/A)$, respectively. For the forward problem, we use a grid spacing of 200 m in the x-, y-, and z-directions. The inversion volume extends 90 km in the cross-axis direction, 120 km in the ridge-parallel direction, and 11 km beneath the seafloor (Figure S1).

The inverse problem is regularized with smoothing and damping constraints requiring the user to specify *a priori* smoothing parameters and model uncertainties. We chose to minimize a function of the form:

$$s^2 = \Delta t' C_d^{-1} \Delta t + \lambda_p (m_0 + \Delta m)' C_m^{-1} (m_0 + \Delta m)$$

$$+ \lambda_v (m_0 + \Delta m)' C_v^{-1} (m_0 + \Delta m) + \lambda_h (m_0 + \Delta m)' C_h^{-1} (m_0 + \Delta m)$$

where Δt is a vector containing the differences between observed and predicted travel-times; C_d is a diagonal matrix containing the data variance defined by the squared travel-time uncertainties; m_0 is a vector of the cumulative perturbation to the isotropic and anisotropic model parameters from previous iterations; Δm is the model perturbation for the current iteration; C_m is a diagonal matrix containing the *a priori* model variance; C_v and C_h are matrices that apply vertical and horizontal nearest-neighbour smoothing, respectively, to each model parameter; and λ_p, λ_v, and λ_h are weighting parameters that set the relative importance of damping, vertical smoothing, and horizontal smoothing constraints, respectively. The perturbational model for isotropic slowness is gridded at 1 km intervals in the x-, y-, and z-directions. With nearest-neighbour smoothing constraints, this grid spacing results in slowness perturbations that are smoothed over a volume comparable to that of the first mantle Pn Fresnel volume, which defines the

theoretical limit of our spatial resolution (Zhang et al., 2007). We assess the model fit to the observed travel-times and compare alternative solutions using the following metric:

$$\chi^2 = \frac{1}{N}\sum_{i=1}^{N}\frac{\Delta t_i^2}{\sigma_i^2}$$

where N is the number of travel-time residuals and Δt_i and σ_i are the travel-time residual and pick error for the ith observation, respectively. Values of $\chi^2 < 1$ suggest the model is overfitting the data and values of $\chi^2 > 1$ suggest the model is underfitting the data. We seek solutions that are spatially smooth, limit the norm of the perturbational model vector, and attain a χ^2 reasonably close to unity.

Our preferred model was obtained with $\lambda_v = \lambda_h = 200$, $\lambda_p = 1$, and depth dependent slowness uncertainties increasing from 1% in the upper crust to 50% in the mantle. Crustal uncertainties are taken to be small since the three-dimensional crustal structure and thickness is constrained by previous work (Weekly et al., 2014; Soule et al., 2016). The Pn ray paths sample a depth range between 6.5 and 8 km beneath the seafloor and because their Fresnel zone is approximately 2 km in the vertical dimension we cannot resolve vertical variations in structure beneath the Moho. Therefore, we chose a vertical smoothing value such that model perturbations do not vary significantly with depth beneath the Moho (Figure S5). We display our preferred solution at 7.8 km beneath the seafloor (Chapter II, Figure 2b), which is the shallowest seafloor-conformable depth that is entirely within the mantle (Figure S5a-b). A map view section that is conformable to the Moho surface is effectively identical (Figure S5c). We searched over various horizontal smoothing values and chose that which provided a smooth solution that fit the data well. Travel-time calculations and inversion for model parameters were performed

until the RMS travel-time residual converged (typically 4-5 iterations). Our preferred model converged to a χ^2-misfit of 1.06 and RMS travel-time residual of 11 ms after 4 iterations (Figure S6).

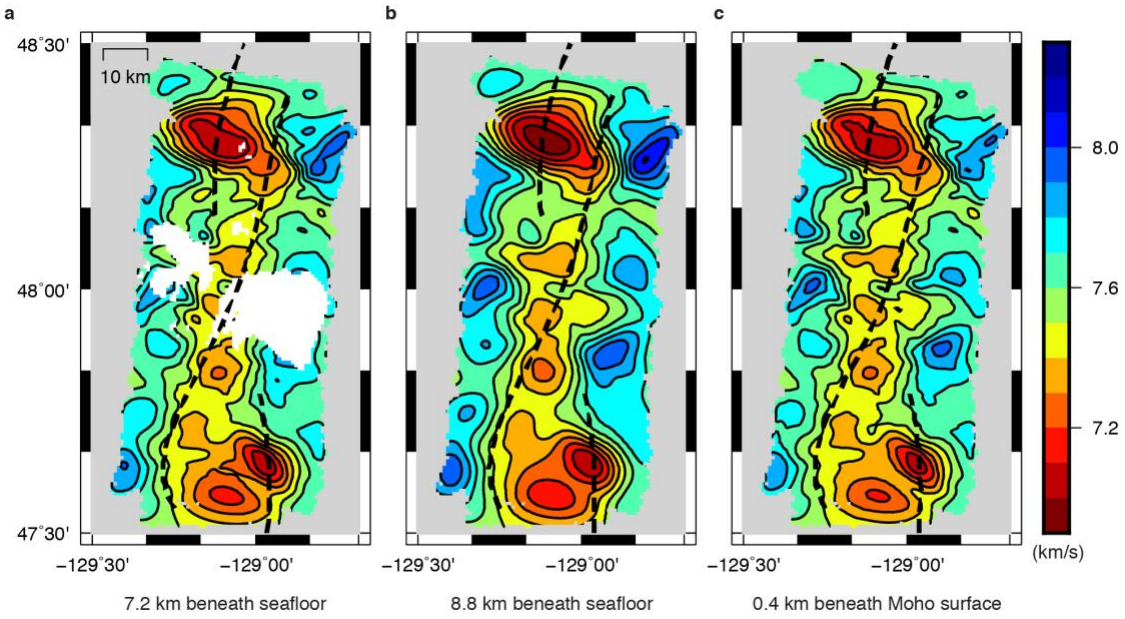

Figure S5. Alternative depth slices through the preferred tomographic mantle velocity model. The isotropic mantle velocity structure is shown at (a) 7.2 km and (b) 8.8 km beneath the seafloor. In (c), we show the isotropic structure on a Moho-conformable surface located 400 m beneath the Moho. Regions of the model space located above the Moho are masked in white and regions with low Pn data coverage are masked in grey. Mantle velocities at each depth slice are effectively identical to each other. The contour interval is 0.1 km/s. The plate boundary is shown by the dashed black line.

Model Sensitivity

We performed numerous inversions to test the stability of our result with respect to inversion parameters, perturbational grid size, and the starting mantle and crustal velocity models. In general, decreased smoothing and damping constraints and finer perturbation grids result in higher magnitude, shorter wavelength perturbations while increased smoothing and damping constraints, and coarser perturbation grids result in lower magnitude and smoother perturbations. Changes to the initial isotropic mantle velocity produced effectively identical mantle images. The main features of our preferred model, anomalously broad and high magnitude MLVZs beneath the OSCs and a narrower region

of low velocities beneath the segment centre, were consistently observed in all our tomographic solutions.

To examine the trade-off between isotropic and anisotropic structure we performed a series of grid-search inversions over starting models with fixed anisotropy orientations. A clear minimum in the χ^2-misfit is observed when the fast-axis orientation matches that fit to the Pn travel-time residuals (Figure S7), which is rotated 12° clockwise from the plate-spreading direction. The grid-search results presented in Figure S7 were performed with a magnitude of anisotropy of 4.7% (i.e. the best-fit magnitude determined from travel-time residuals). Similar curves are obtained when imposing a magnitude of anisotropy of 3.5% and 6% (Figure S7). However, at these magnitudes the model misfit is systematically greater compared to the best-fit magnitude. Imposing an isotropic mantle resulted in a significantly increased χ^2-misfit (1.62) substantiating the presence of mantle anisotropy. Limited azimuthal coverage and strong isotropic heterogeneity prevented a robust interpretation of mantle anisotropy beneath overlapping portions of the Endeavour from

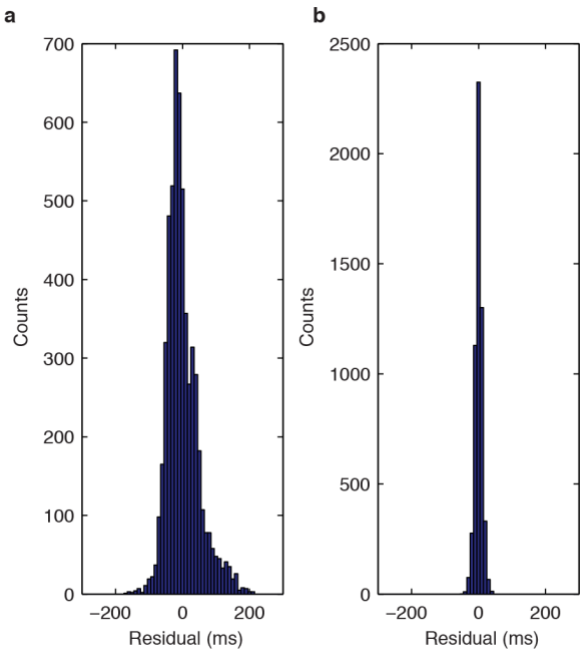

Figure S6. Distribution of Pn travel-time residuals before and after tomographic analysis. Histogram plots of travel-time residuals with respect to (a) the starting 3D crustal model and a homogeneous, anisotropic mantle model and (b) the preferred mantle solution (Chapter II, Figure 2b). Residuals are binned at 10 ms intervals. Prior to inversion (a), the Pn travel-time residuals have a mean and standard deviation of 0 ms and 48 ms, respectively. After four iterations (b), the mean residual is 0 ms and the standard deviation is reduced to 11 ms. The preferred solution (Chapter II, Figure 2b and 3) explains greater than 97% of the data variance.

travel-time residuals alone. To determine if anisotropic structure is required beneath the segment ends, we inverted our Pn dataset assuming only the mantle beneath the central, non-overlapping, portion of the Endeavour is seismically anisotropic. This resulted in an increased χ^2-misfit (1.14) suggesting the mantle beneath the entire length of the Endeavour is seismically anisotropic.

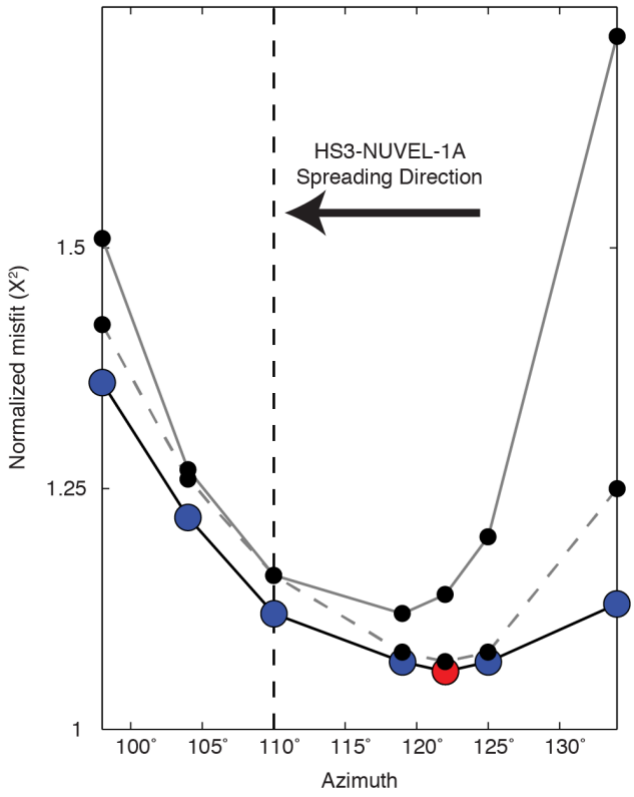

Figure S7. Normalized data misfit versus azimuth of anisotropy. The fit of tomographic solutions to the Pn travel-time data is shown for different anisotropic mantle models. Red and blue points along the black curve show how the normalized data misfit varies as a function of the seismically fast-axis orientation at a constant magnitude of anisotropy of 4.7%. Similarly, the black points along the solid and dashed gray lines show the normalized data misfit as a function of the seismically fast-axis orientation for models with 6% and 3.5% anisotropy, respectively. The vertical dashed black line indicates the plate-spreading direction (Gripp & Gordon, 2002).

To test the sensitivity of our preferred solution to the starting crustal thickness model, we inverted the Pn arrival times under the assumption that crustal thickness does

not vary, which is a poor assumption given previous studies at Endeavour (Soule et al., 2016; Carbotte et al., 2008) and elsewhere along the JdFR (Carbotte et al., 2008; Marjanović et al., 2011) and EPR (Canales et al., 2003). We created a model with uniform crustal thickness of 6.8 km (the mean value of the tomographically determined crustal thickness model from Soule et al., 2016) and inverted our Pn dataset for isotropic perturbations. We assumed our preferred anisotropic model and followed the inversion procedure outlined above. The recovered isotropic structure (Figure S8a) is comparable to our preferred results (Chapter II, Figure 2b and Figure S5). In particular, the MLVZ is relatively narrow beneath the central region of the Endeavour segment and anomalously wide beneath each OSC. The primary effect of assuming constant crustal thickness is to decrease the amplitude of the low-velocity anomalies beneath each OSC. This occurs because the assumed crustal thickness (6.8 km) overestimates the thickness of the crust beneath each OSC by 0.5-0.8 km. We also verified that the anisotropic structure interpreted from Pn delays is insensitive to crustal thickness variations. We calculated azimuthal variations in Pn travel-times relative to a model with constant crustal thickness (6.8 km) and an isotropic, homogeneous (7.6 km/s) mantle (Figure S8b). These residuals are processed and fit following the same procedure used to construct our preferred anisotropic model. The best-fit fast-axis orientation and magnitude is 125° ± 1° (15° clockwise from the plate-spreading direction) and 4.7% ± 0.4%, respectively. This result is nearly identical to our preferred estimate of mantle anisotropy. We conclude that the mantle isotropic and anisotropic structure is relatively insensitive to crustal thickness variations.

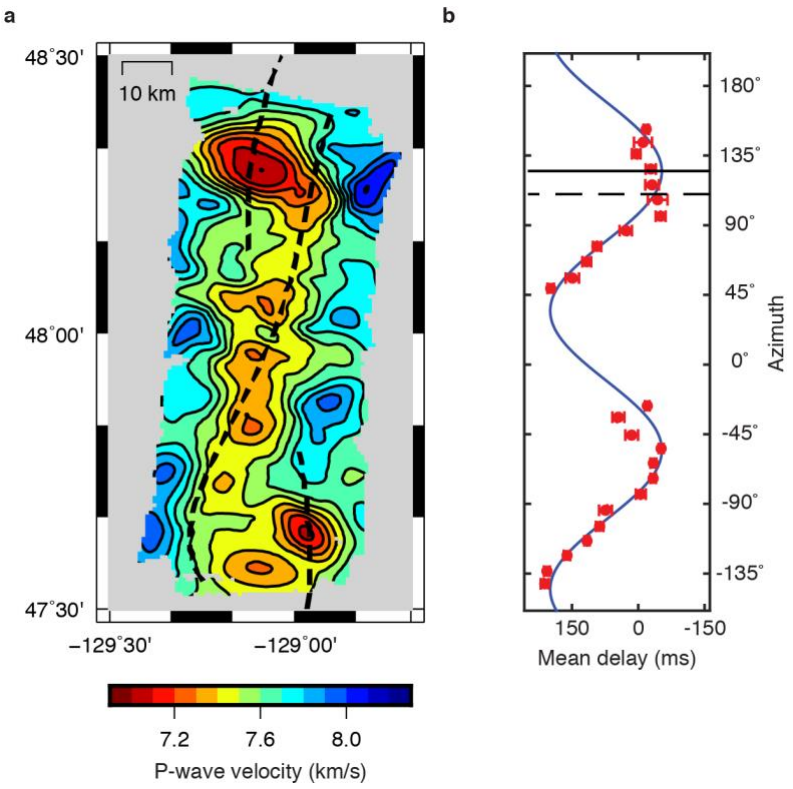

Figure S8. Tomographic result assuming constant crustal thickness. (a) The isotropic mantle velocity structure recovered from inverting our Pn dataset using a starting model with uniform crustal thickness (6.8 km) is shown at 7.8 km beneath the seafloor. Contour interval is 0.1 km/s. Areas of low Pn data coverage are masked in grey. The plate boundary is shown by the dashed black line. In (b), we show the mean Pn delays plotted by azimuth. Error bars show the 95% confidence interval in the mean delay time as determined by a Student's t-test. The best-fit fast-axis orientation and magnitude is 125° ± 1° (15° clockwise from the plate-spreading direction) and 4.7% ± 0.4%, respectively. The vertical dashed and solid lines mark the spreading direction (110°; Gripp & Gordon, 2002) and the seismically fast-axis orientation, respectively.

Model Resolution

We identify the region in which our preferred model is well resolved by analysing the spatial distribution of ray paths. Specifically, we use the derivative weight sum (DWS) to measure the density of predicted ray paths that influence each perturbational node in the inversion volume (Toomey & Foulger, 1989). Based on checkerboard resolution tests (discussed below), anomalies located within regions of the model space with a DWS less than ~30 are poorly reconstructed. Therefore, we mask regions of the model with a DWS

below 30. The vast majority of mantle perturbational nodes within 20 km of the plate boundary have a DWS value greater than 1000 (Figure S9a).

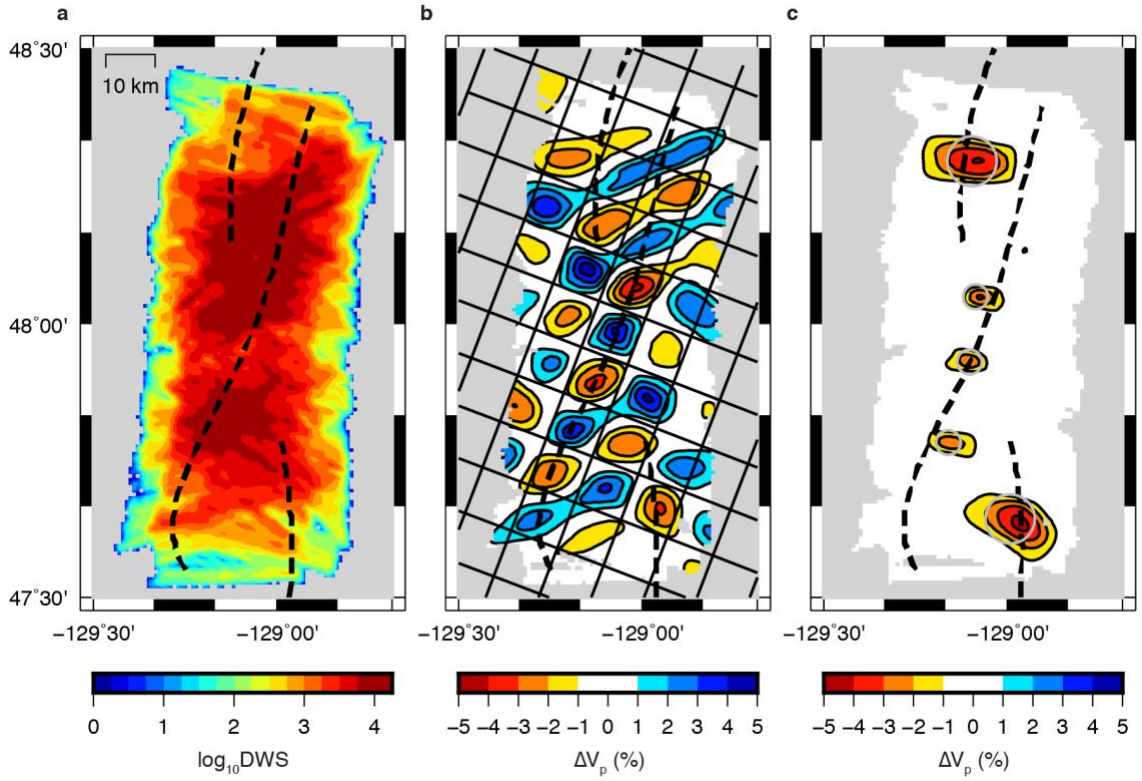

Figure S9. Mantle data coverage and resolution. (a) The relative density of mantle ray coverage is shown by the derivative weight sum (DWS; Toomey & Foulger, 1989). Dense mantle ray coverage (DWS > ~30) extends along the entire length of the Endeavour segment and within ~20 km of the plate boundary. (b) The recovery of synthetic mantle checkerboard-patterned anomalies is shown at 7.8 km beneath the seafloor. The true model contains a sinusoidal pattern of velocity perturbation in the xy-plane with a peak magnitude of 5% applied to a 7.6 km/s mantle. The wavelength of the velocity perturbations is 10 km in both x- and y-directions. Black gridlines mark the true boundary between alternating fast and slow perturbations in the synthetic model. (c) The recovery of cylindrical mantle low-velocity anomalies is shown at 7.8 km beneath the seafloor. The size and locations of the five anomalies are shown by grey circles. The magnitude of each low-velocity anomaly is 5% with respect to a 7.6 km/s mantle. In (b) and (c), contours are drawn at 1% intervals and the 0% contour is omitted for clarity. The dashed black lines in each panel show the location of the plate boundary.

We assess the resolution of mantle isotropic structure using checkerboard tests. We constructed synthetic models with an alternating sinusoidal pattern of positive and negative isotropic velocity anomalies with a magnitude of 5% applied to a homogeneous mantle with velocity of 7.6 km/s. Each anomaly covered a 10 km by 10 km square region in the xy-plane and the polarity of the anomalies did not vary with depth. No anomalies

were placed within the crust and we imposed 4% mantle anisotropy with a fast-axis rotated 12° clockwise from the plate-spreading direction. We calculated travel-times for Pn arrivals using the same data geometry used to construct our preferred solution. Each travel-time was assigned an uncertainty of 11 ms and random noise with a standard deviation of 11 ms was added to the synthetic Pn dataset. These travel-times were then inverted for isotropic perturbations (the true anisotropic structure was assumed for the starting model) following the same inversion procedure used in our preferred solution. The results of this test are shown in Figure S9b. In general, the distribution of recovered mantle perturbations accurately reflects the true checkerboard model. The locations of low-velocity anomalies are well recovered while the magnitudes are typically underestimated. Our checkerboard tests indicate mantle structure is well constrained within ~20 km of the plate boundary and beneath each OSC.

In addition to checkerboard tests, we assess our model resolution by reconstructing more geologically plausible anomalies. We constructed a synthetic model containing three circular low-velocity anomalies, 5 km in diameter, along the segment centre. We also placed two circular low-velocity anomalies, 10 km in diameter, beneath either OSC. The magnitude of all five MLVZs is 5% with respect to a 7.6 km/s mantle and each anomaly extends from the Moho to the base of our model. Synthetic arrival times were created, processed, and inverted the same as for the checkerboard test described above. The true and recovered models are shown in Figure S9c. The locations of all five anomalies are accurately recovered and, as is common in tomography, the magnitude of the low-velocity anomalies are underestimated by ~1-2%. As a consequence of the smoothing constraints required to regularize the inverse problem, the

spatial extent of each anomaly is overestimated by at most a few kilometres. We conclude from this resolution test that the broad MLVZs beneath the OSCs observed in our preferred tomographic solution (Chapter II, Figure 2b) are a robust feature and that velocity anomalies as small as ~5 km in diameter are resolved by our Pn dataset.

Estimates of Melt Fraction

We attribute variations in the isotropic component of mantle velocity to elevated temperatures and partial melt. We first attempt to explain the low-velocity anomalies in terms of thermal perturbations alone. Away from tectonic offsets, velocity minima beneath the ridge axis are 0.4 km/s slower than seismic velocities 10 km off axis. Within the OSCs, mantle velocities are reduced by 0.6 km/s with respect to velocities 15 km from the plate boundary. Accounting for both anharmonic and anelastic effects (Dunn et al., 2000; Karato, 1993), thermal anomalies in excess of 300 K and 500 K are required to fully explain the reduced seismic velocities across the segment centre and segment ends, respectively. Such cross-axis variations in sub-Moho temperatures are inconsistent with mid-ocean ridge thermal models (Morgan & Chen, 1993), which predict gradual temperature variations of ~200 K within 10 km of the plate boundary. An increase in temperature of 200 K explains less than 60% of the MLVZ minima near the segment centre and less than 40% of the MLVZ minima within the OSCs. We interpret the remaining velocity anomaly in terms of partial melt. If melt is distributed in thin films and tubules (Hammond & Humphreys, 2000), the remaining velocity anomaly is consistent with <2% melt beneath the segment centre and 1 to 5% melt beneath the OSCs. Along-axis variations in seismic wave speeds likely reflect variations in the extent of partial melt within the mantle. Temperature is not expected to vary significantly in the

ridge-parallel direction except near tectonic offsets where the juxtaposition of older crust should result in cooler axial temperatures (Neumann & Forsyth, 1993; Magde & Sparks, 1997). However, we observe the lowest velocities beneath the OSCs, which does not suggest a cooler mantle and instead suggests these 2nd-order discontinuities are currently regions of greater melt fractions.

We use our preferred tomographic solution (Chapter II, Figure 2b) to make an upper estimate of the volume of mantle melt beneath each OSC and the segment centre. We calculate the change in P-wave velocity with respect to a 7.8 km/s mantle assuming no melt is present at velocities ≥ 7.8 km/s. Next, we adjust the velocity perturbations to account for a 200 K thermal anomaly and include both the anharmonic and anelastic effects of temperature on P-wave velocity (Dunn et al., 2000; Karato, 1993). We convert the remaining velocity anomaly to partial melt assuming melt is distributed in relaxed thin films and tubules (Hammond & Humphreys, 2000). The calculated partial melt fractions are partitioned into three regions—the southern OSC (below ~47°45'N), the central Endeavour (between ~47°45'N and ~48°10'N), and the northern OSC (above ~48°10'N). To estimate the volume of melt within each region, the melt fractions are integrated over each of the three areas to a depth of 4 km (the approximate sub-Moho depth sensitivity of Pn phases). Only velocity perturbations in well-resolved (unmasked) regions of our preferred solution (Chapter II, Figure 2b; Figure S9a) were used in this calculation. We estimate as much as 90 km^3 of melt is present beneath each OSC. We estimate as much as 40 km^3 of melt is present beneath the central Endeavour.

Potential Influence of Seamount Chains on Mantle Melt Distribution

We argue that the seismically inferred mantle melt distribution beneath the Endeavour segment cannot be attributed to the influence of nearby seamount chains. There are three seamount chains that intersect the Endeavour ridge. From south to north these are the Springfield, Heckle, and Heck Seamounts that intersect the ridge at the southern OSC, segment centre, and northern OSC, respectively. Geochemical investigation of these seamounts shows them to be petrologically distinct from Endeavour axial basalts (Karsten et al., 1990). Additionally, the petrology of basalts collected along the Endeavour ridge do not show evidence for along-axis variations in melt supply (Karsten et al., 1990). These observations suggest that nearby seamount chains have not influenced melt production beneath the Endeavour. We also note that Endeavour seamount, which sits between the overlapping limbs of the northern OSC, was not produced *in situ* but was captured following a ridge propagation event (Karsten et al., 1986) and thus does not reflect recent melt production or melt extraction processes beneath the northern Endeavour ridge. However, if we assume these seamount chains are associated with melting anomalies, then both the segment centre and segment ends should be regions of enhanced mantle melt supply. However, anomalously thick crust is only located beneath the segment centre (near the intersection of the Heckle seamounts) and the crust thins beneath either OSC (Soule et al., 2016; Carbotte et al., 2008). Given that we observe anomalously low and broad seismic velocity anomalies beneath either OSC with respect to the segment centre, the hypothetical excess melt associated with the Springfield and Heck Seamounts would appear to be preferentially trapped beneath the

OSCs. Thus, as we have argued, along-axis variations in the volume of mantle melt must be related to variations in the efficiency of mantle melt extraction.

APPENDIX B

CHAPTER III SUPPORTING INFORMATION

Introduction

Here we provide additional details of our data analysis. We describe our arrival time picking strategy (Text S1), present the data subsets and Pn ray coverage used in our analysis (Text S2), and discuss the sensitivity of our preferred solution to prescribed model parameters (Text S3). In Text S4, we describe how we estimate the mean paleo-spreading direction sampled by our dataset. Five supporting figures relevant to our results are included.

Text S1. Arrival Time Picking Procedure

Following Skintaku et al. (2014), we employ an automated picking method in which we fit a linear profile to the logarithm of the envelope of the Pn waveform (Chapter III, Figure 2). This method takes advantage of the clear ramp-up in amplitude at the onset of the Pn arrival. Seismograms are bandpass filtered between 5 Hz and 10 Hz (the band in which the Pn phase is most clearly visible; Chapter III, Figure 2a-b). Next, we calculate the envelopes of the filtered waveforms and take the natural logarithm of the envelope. As pointed out by Shintaku et al. (2014) and observed in our dataset, the noise pattern before and after the onset of Pn is not normally distributed but contains larger negative excursions than positive. A least-squares fitting technique assumes the noise in the data to be fit is normally distributed. Thus, we smooth the logarithm of the envelope with a 10-point moving average (Chapter III, Figure 2c-d) such that this assumption is met.

While our data processing steps are identical to Shintaku et al. (2014), our fitting procedure differs. We characterize the smoothed logarithm of the Pn envelopes with three domains defined by the lines (Chapter III, Figure 2c):

$$y(t < t_0) = y_0$$

$$y(t_0 \leq t < t_1) = \frac{(y_1 - y_0)}{(t_1 - t_0)}(t - t_0) + y_0$$

$$y(t \geq t_1) = y_1$$

Domain I ($t < t_0$) includes 10 s of signal before the ramp onset, domain II ($t_0 \leq t < t_1$) spans the duration of the ramp, and domain III ($t \geq t_1$) includes 10 s following the end of the ramp. We invert in a least-squares sense for the best-fit t_0, y_0, t_1, and y_1 parameters which define the starting and ending points of the ramp (Chapter III, Figure 2c). This problem is non-linear so we iterate to find the optimal solution. The solution converges quickly within 10 iterations (Chapter III, Figure 2c-d). The best-fit t_0 parameter (i.e. the starting time of the ramp) after 10 iterations is taken as the Pn arrival time. The starting model for the picking procedure is defined as follows; t_0 is the predicted Pn arrival time; t_1 is equal to $t_0 + 2$ (i.e. a 2 s ramp duration is initially assumed); and y_0 and y_1 are defined as the mean of the smoothed logarithm of the envelope on the intervals of $(t_0 - 10, t_0)$ and $(t_1, t_1 + 10)$, respectively. All picks are visually inspected and assigned user-defined relative errors based on the signal-to-noise ratio and impulsiveness of the Pn arrival. The errors are used to weight the Pn travel-times for event relocations.

In comparison, Shintaku et al. (2014) require the ramp duration to be the same for all stations for a given event. However, we find that for a given event the ramp duration tends to vary with offset with closer range arrivals typically having a shorter ramp

duration. It may be that this dependence is only seen in relatively short-range arrivals and becomes less significant when propagation distances exceed 500 km (as in Shintaku et al., 2014). Additionally, Shintaku et al. (2014) grid-search over prescribed t_0 values to find the optimal solution whereas we have adopted an iterative least-squares approach.

Text S2. Data Coverage

To characterize the anisotropic structure surrounding the Blanco Transform Fault separate from that of the plate interior and to mitigate potential relocation errors associated with biased azimuthal ray coverage, we relocate Blanco events using a subset of our Pn dataset that only includes arrivals recorded on stations located within 180 km of the transform fault. Figure S1a shows the ray paths for the 317 arrivals included in this data subset. We use Pn travel-times with ray paths that are confined to the Juan de Fuca (JdF) plate (Figure S1b) to estimate the uppermost mantle anisotropic structure of the plate interior. This plate interior dataset includes 623 arrival times 183 of which are common to the relocation data subset. We note that due to limited azimuthal coverage, we cannot resolve any spatial variations that might exists in the anisotropic signal.

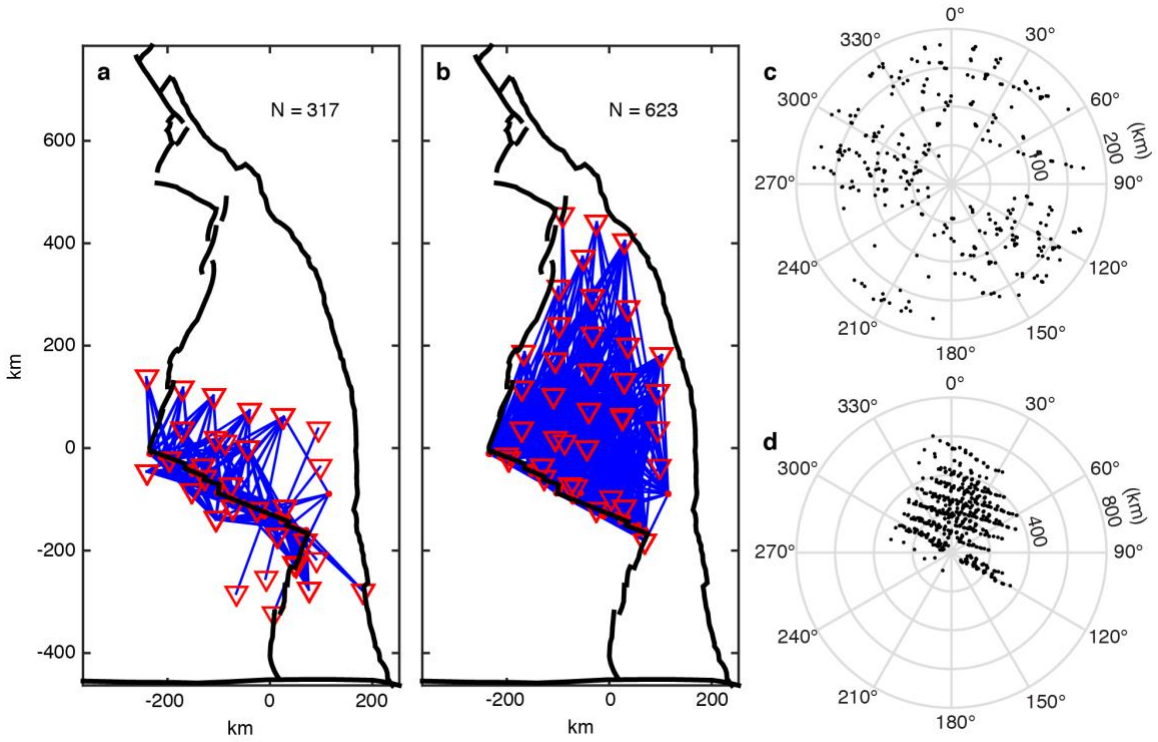

Figure S1. Map-view Pn ray paths for the (a) Blanco and (b) plate interior data subset. Seismic stations and relocated events are shown by the red triangles and points, respectively. The black line identifies the plate boundaries. The number of rays in each data subset is defined in the top right corner. The polar plots display the range (radial axis) and azimuth (clockwise from north) of each Pn travel-time measurement in the (c) Blanco and (d) plate interior data subsets.

Text S3. Preferred Model and Solution Sensitivity

As a consequence of imperfect ray coverage, the uncertainty in our estimates of mantle anisotropy largely reflects the trade-off between epicentral and anisotropic parameters. Therefore, we adopted a grid-search strategy to determine our preferred model and to characterize the uncertainty in this model (Figure S2). Using the Blanco domain dataset, we perform a least-squares inversion for perturbations to Blanco epicentral parameters, damped station static terms, and isotropic mantle velocity under a prescribed magnitude and orientation of mantle seismic anisotropy. In Figure S2a, the best-fit to the Blanco domain dataset is plotted as a function of the prescribed magnitude and orientation of mantle anisotropy used to relocate Blanco events. For each relocation solution, we estimate the best-fit anisotropic parameters to the plate interior dataset by

least-squares fitting Equation 1 in Chapter III to the mantle velocities estimated from Pn travel-times binned as a function of azimuth (20° intervals). Thus, we are searching for separate anisotropic mantle models for each dataset. The best-fit to the plate interior dataset for a given relocation model is shown in Figure S2b. We prefer models that provide a good fit at the 1σ confidence interval (based on an F-test) to both datasets. In doing so, we find that relocating Blanco events assuming 4.6%-5% mantle anisotropy with a fast-axis azimuth of 85°-96° yields adequate fits to both datasets. Solutions that fall outside this range are less likely. We assume this range reflects the uncertainty in the best-fit anisotropic model to the Blanco dataset. In Figure S2c-e we show how the fast-axis orientation, percent anisotropy, and mean mantle velocity resolved using the plate interior dataset varies as a function of the anisotropic model used to relocate Blanco events. We reject any solution obtained where the Blanco anisotropic parameters fall outside the best-fit range quoted above. This yields a range of acceptable mantle anisotropic models (fast-axis azimuth = 84°-90°; anisotropic magnitude = 4.2%-5%; mean mantle velocity = 7.83 km/s-7.87 km/s) to the plate interior dataset. Again, we assume this range reflects the uncertainty in the best-fit anisotropic model to the plate interior dataset. As shown in Figure S2f, we estimate the uncertainty in the best-fit mean mantle velocity in the Blanco domain in a similar manner. We find that the acceptable range of mean mantle velocities in the Blanco domain is 7.82 km/s-7.88 km/s.

In Figure S3, we show the distribution of Pn travel-time residuals calculated with respect to our starting (isotropic, 7.8 km/s mantle) and preferred model for each data subset. Our preferred solution (identified by stars in Figure S2) to the Blanco and plate interior data subsets decrease the variance in the Pn travel-time residuals by 99.8% and

61.2%, respectively (Figure S3). The substantially larger variance reduction in the Blanco data subset is due to differences between the starting models for each dataset. The starting model for the Blanco data subset uses the catalogued epicentral parameters whereas the starting model for the plate interior data subset uses the relocated event parameters. The misfit to the Pn travel-time residuals (as defined by the weighted root mean square) for our preferred solution to the Blanco and plate interior data subsets is 195 ms and 416 ms, respectively. The misfit to either data subset is significantly increased (at the 1σ confidence level) if only isotropic mantle velocity models are considered. We note that the misfit to the Blanco data subset is less sensitive to the Blanco domain anisotropic structure compared to the plate interior data subset (Figure S2a-b). This may be due to the shorter Pn propagation distances associated with the Blanco dataset resulting in lower magnitude arrival time residuals related to anisotropic structure. A more complex anisotropic field surrounding the Blanco Transform Fault may also contribute to this observation.

Figure S2 (next page). Results of the grid-search over anisotropic mantle velocity models used to relocate Blanco events. The weighted sum of the squared Pn travel-time residuals (WSSR) are plotted for (a) the Blanco and (b) the plate interior data subset as a function of the fast-axis azimuth (x-axis) and percent mantle anisotropy (colored curves) assumed for earthquake relocation. The horizontal dashed and solid black lines identify the 1σ and 2σ confidence intervals. The best-fit (c) fast-axis orientation, (d) percent anisotropy, and (e) mean mantle velocity to the plate interior dataset and (f) the best-fit mean mantle velocity to the Blanco dataset are also plotted as a function of the anisotropic mantle velocity model assumed for earthquake relocation. Points that fall along the curves in gray-scale in (c-f) identify models that we have rejected because they do not provide a good fit to both data subsets (a-b) at the 1σ confidence level. The vertical dashed and solid lines in (c-f) identify the acceptable range of fast-axis azimuths in the anisotropic mantle velocity model used for earthquake relocation at the 1σ and 2σ confidence levels, respectively. The range of mantle velocity parameters that provide good fits to the data (at 1σ uncertainty) fall along the colored curves and between the vertical dashed lines in (c-f). The red star marks our preferred solution. See Appendix B, Text S3 for further discussion.

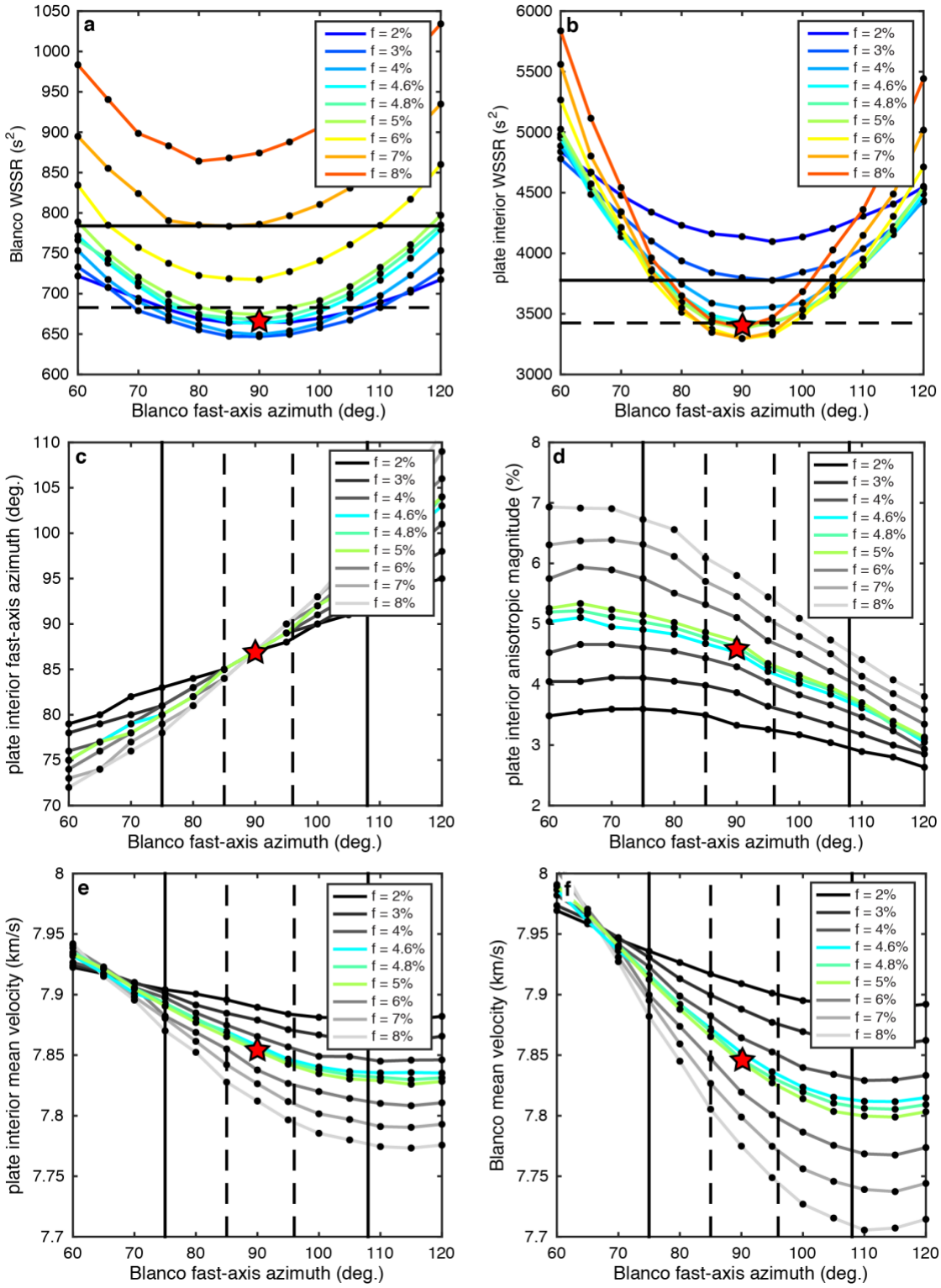
a
b
c
d
e
f
f = 2%
f = 3%
f = 4%
f = 4.6%
f = 4.8%
f = 5%
f = 6%
f = 7%
f = 8%
Blanco WSSR (s^2)
plate interior WSSR (s^2)
plate interior fast-axis azimuth (deg.)
plate interior anisotropic magnitude (%)
plate interior mean velocity (km/s)
Blanco mean velocity (km/s)
Blanco fast-axis azimuth (deg.)

To estimate the errors in our earthquake locations, we grid-search over perturbations to the event positions in our preferred solution (Chapter III, Figure 3). For each perturbed position, we calculate the weighted sum of the squared Pn travel-time residuals and use an F-test at the 1σ confidence level to define points on an error ellipse. The anisotropic model is held fixed during this grid-search. We find that the positions of our earthquake relocations depend on the mantle anisotropic model but the error ellipse mostly reflect the number of arrivals constraining the epicentral parameters for a given event.

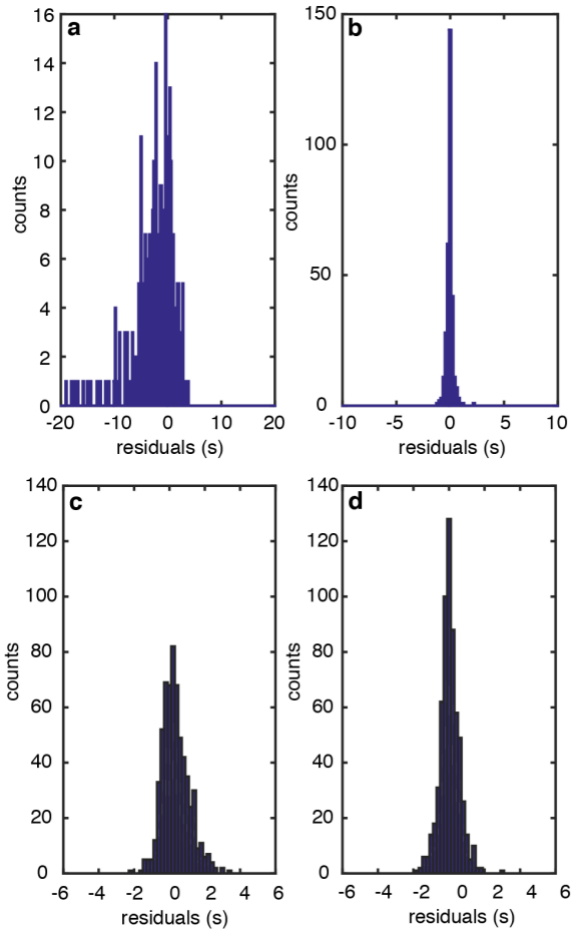

Figure S3. The distribution of the Pn travel-time residuals for the (a-b) Blanco and (c-d) plate interior data subsets with respect to (a,c) the starting model and (b,d) our preferred solutions.

We investigate the sensitivity of our result to the chosen inversion strategy and user-defined parameters and find that our preferred solution is a stable result. Joint least-squares inversions for epicentral and anisotropic parameters using the entire Pn dataset recover similar anisotropic fast-axis orientations (84°-90°) as our preferred solution and slightly reduced magnitudes of anisotropy (3%-4%). The exclusion of station statics does not alter the best-fit anisotropic solution to either dataset. However, the inclusion of station statics decreases the model misfit to both the Blanco and plate interior data

subsets by 65 ms and 122 ms, respectively. We note that the value of the station statics recovered in our preferred solution (Figure S4) are less than the magnitude of the anisotropic signal of interest (>600 ms for 4.5% anisotropy and ray paths >100 km). Perturbing the source depths by ±2 km does not significantly alter our preferred solution. Oceanic crustal thickness and velocity variations are not likely to exceed 1 km and 1 km/s, respectively. Such perturbations to the assumed crustal structure do not alter our solution. The east-west directed gradient in sediment thickness (Divins, 2003) in combination with uneven azimuthal data coverage could bias our estimate of mantle anisotropy by making mantle velocities appear artificially slower for ray azimuths that preferentially sample more heavily sedimented regions. To estimate the effect of sediment thickness on the anisotropic structure we scale our sediment corrections by 50% and 150%. In doing so we find that the recovered fast-propagation direction does not vary by more than ±3° (i.e. within estimated error).

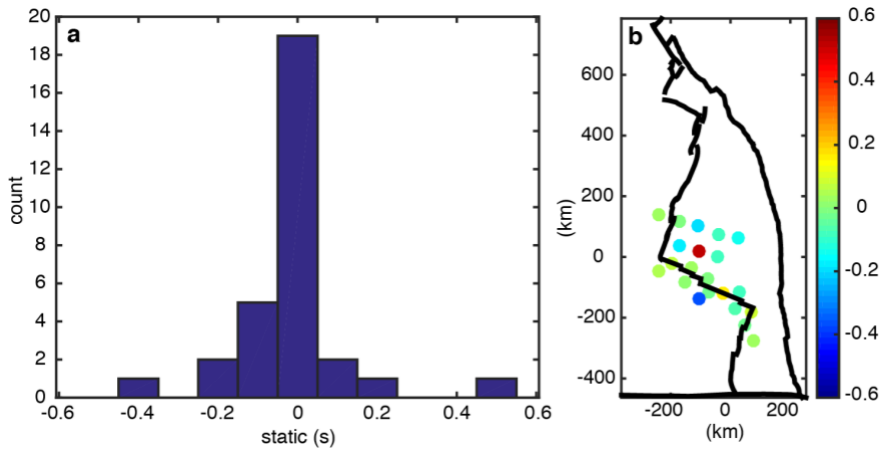

Figure S4. (a) The distribution of station statics used in our preferred solution. (b) Map view of the applied station statics.

Age-dependent thermal structure is likely the primary cause for variations in the isotropic velocity of uppermost oceanic mantle. Age-dependent variations in mantle velocity in combination with uneven azimuthal sampling may bias our estimate of mantle

anisotropy. We use a synthetic test to estimate the significance of thermally-induced perturbations to mantle velocity on our recovery of mantle anisotropy. We calculate Pn arrival times for a model with the crustal structure assumed for our preferred solution, isotropic mantle velocities that vary with plate age (Figure S5), and 5% mantle anisotropy with a fast propagation azimuth of 110°. Synthetic data coverage matches that used in this study (i.e. Figure S1). The isotropic velocities are calculated from the temperatures predicted at 10 km beneath the Moho (the average depth sensitivity of our Pn data) based on a half-space cooling model with a temperature of 1300 °C at zero age and mantle thermal diffusivity of 8e-7 m^2s^{-1}. Temperatures are converted to P-wave velocity following Karato (1993). The isotropic velocity at zero age is defined as 7.6 km/s (based on the results of VanderBeek et al., 2016) and the maximum isotropic velocity is not allowed to exceed 8.2 km/s. We apply random errors to the x-, and y-positions of the earthquakes in this synthetic test. The errors are drawn from a normal distribution with standard deviation of 30 km and are forced to be positive such that the events are shifted to the northeast as observed in this study. Errors are also applied to the event origin times and these are drawn from a normal distribution with standard deviation of 1 s. We then proceed to invert for epicentral and anisotropic parameters following the procedure for our preferred solution (Text S3). Neglecting

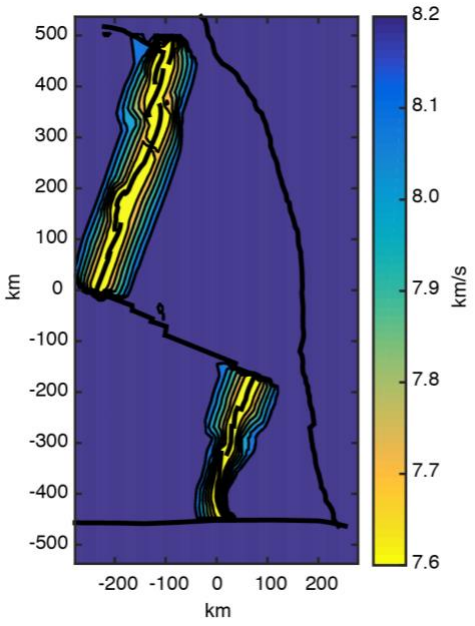

Figure S5. The isotropic mantle velocity model used to test the sensitivity of the recovered anisotropic structure to isotropic heterogeneity (Appendix B, Text S3). Mantle velocities do not vary with depth.

isotropic mantle heterogeneity could bias the fast-axis in the counterclockwise direction by up to 5°. This bias, if present in our data, is not significant enough to alter our interpretation. We note that available constraints on uppermost mantle velocity beneath the JdF plate do not strongly correlate with age except directly beneath the spreading center (VanderBeek et al., 2016; Horning et al., 2016). Thus, isotropic velocity anomalies likely do not influence our estimates of mantle anisotropy.

Text S4: Estimation of Mean Paleo-spreading Direction

The JdF ridge spreading direction has been rotating clockwise over the last ~10 Myr (Riddihough, 1984). Using the Pn ray coverage (Figure S1) and crustal age map of Wilson (1988) we calculate the mean plate age sample by both datasets. Assuming the plate spreading direction is orthogonal to magnetic anomaly lineations, we convert these mean ages to mean spreading directions from the strike of the magnetic anomalies measured through time on the Juan de Fuca and Pacific plates as presented in Riddihough (1984). The Blanco and plate interior Pn datasets sample 4.1 Myr and 4.4 Myr old uppermost mantle corresponding to a mean spreading direction of 101° and 105°, respectively.

REFERENCES CITED

Chapter II

Aghaei, O., Nedimović, M. R., Carton, H., Carbotte, S. M., Canales, J. P., & Mutter, J. C. (2014). Crustal thickness and Moho character of the fast-spreading East Pacific Rise from 9° 42′ N to 9° 57′ N from poststack-migrated 3-D MCS data. *Geochemistry, Geophysics, Geosystems*, *15*(3), 634-657.

Backus, G. E. (1965). Possible forms of seismic anisotropy of the uppermost mantle under oceans. *Journal of Geophysical Research*, *70*(14), 3429-3439.

Barclay, A. H., Toomey, D. R., & Solomon, S. C. (1998). Seismic structure and crustal magmatism at the Mid-Atlantic Ridge, 35° N. *Journal of Geophysical Research: Solid Earth*, *103*(B8), 17827-17844.

Barth, G. A., & Mutter, J. C. (1996). Variability in oceanic crustal thickness and structure: Multichannel seismic reflection results from the northern East Pacific Rise. *Journal of Geophysical Research: Solid Earth*, *101*(B8), 17951-17975.

Bazin, S., Harding, A. J., Kent, G. M., Orcutt, J. A., Singh, S. C., Tong, C. H., ... & Hobbs, R. W. (2003). A three-dimensional study of a crustal low velocity region beneath the 9°03′ N overlapping spreading center. *Geophysical research letters*, *30*(2).

Becker, T. W., Chevrot, S., Schulte-Pelkum, V., & Blackman, D. K. (2006). Statistical properties of seismic anisotropy predicted by upper mantle geodynamic models. *Journal of Geophysical Research: Solid Earth*, *111*(B8).

Bell, R. E., & Buck, W. R. (1992). Crustal control of ridge segmentation inferred from observations of the Reykjanes Ridge. *Nature*, *357*(6379), 583.

Blackman, D. K., & Kendall, J. M. (2002). Seismic anisotropy in the upper mantle 2. Predictions for current plate boundary flow models. *Geochemistry, Geophysics, Geosystems*, *3*(9), 1-of.

Bodmer, M., Toomey, D. R., Hooft, E. E., Nábělek, J., & Braunmiller, J. (2015). Seismic anisotropy beneath the Juan de Fuca plate system: Evidence for heterogeneous mantle flow. *Geology*, *43*(12), 1095-1098.

Pablo Canales, J., Detrick, R. S., Toomey, D. R., & Wilcock, W. S. (2003). Segment-scale variations in the crustal structure of 150–300 kyr old fast spreading oceanic crust (East Pacific Rise, 8 15′ N–10 5′ N) from wide-angle seismic refraction profiles. *Geophysical Journal International*, *152*(3), 766-794.

Cannat, M. (1996). How thick is the magmatic crust at slow spreading oceanic ridges?. *Journal of Geophysical Research: Solid Earth*, *101*(B2), 2847-2857.

Carbotte, S. M., Small, C., & Donnelly, K. (2004). The influence of ridge migration on the magmatic segmentation of mid-ocean ridges. *Nature*, *429*(6993), 743.

Carbotte, S. M., Detrick, R. S., Harding, A., Canales, J. P., Babcock, J., Kent, G., ... & Diebold, J. (2006). Rift topography linked to magmatism at the intermediate spreading Juan de Fuca Ridge. *Geology*, *34*(3), 209-212.

Carbotte, S. M., Nedimović, M. R., Canales, J. P., Kent, G. M., Harding, A. J., & Marjanović, M. (2008). Variable crustal structure along the Juan de Fuca Ridge: Influence of on-axis hot spots and absolute plate motions. *Geochemistry, Geophysics, Geosystems*, *9*(8).

Carbotte, S. M., Smith, D. K., Cannat, M., & Klein, E. M. (2015). Tectonic and magmatic segmentation of the Global Ocean Ridge System: A synthesis of observations. *Geological Society, London, Special Publications*, *420*, SP420-5.

Collier, J. S., & Sinha, M. C. (1992). Seismic mapping of a magma chamber beneath the Valu Fa Ridge, Lau Basin. *Journal of Geophysical Research: Solid Earth*, *97*(B10), 14031-14053.

Cormier, M. H., Scheirer, D. S., & Macdonald, K. C. (1996). Evolution of the East Pacific Rise at 16° –19° S since 5 Ma: Bisection of overlapping spreading centers by new, rapidly propagating ridge segments. *Marine Geophysical Researches*, *18*(1), 53-84.

Crawford, W. C., & Webb, S. C. (2002). Variations in the distribution of magma in the lower crust and at the Moho beneath the East Pacific Rise at 9°–10° N. *Earth and Planetary Science Letters*, *203*(1), 117-130.

Dunn, R. A., Toomey, D. R., & Solomon, S. C. (2000). Three-dimensional seismic structure and physical properties of the crust and shallow mantle beneath the East Pacific Rise at 9° 30'N. *Journal of Geophysical Research: Solid Earth*, *105*(B10), 23537-23555.

Dunn, R. A., Lekić, V., Detrick, R. S., & Toomey, D. R. (2005). Three-dimensional seismic structure of the Mid-Atlantic Ridge (35° N): Evidence for focused melt supply and lower crustal dike injection. *Journal of Geophysical Research: Solid Earth*, *110*(B9).

Dunn, R. A., Martinez, F., & Conder, J. A. (2013). Crustal construction and magma chamber properties along the Eastern Lau Spreading Center. *Earth and Planetary Science Letters*, *371*, 112-124.

Gripp, A. E., & Gordon, R. G. (2002). Young tracks of hotspots and current plate velocities. *Geophysical Journal International*, *150*(2), 321-361.

Hammond, W. C., & Humphreys, E. D. (2000). Upper mantle seismic wave attenuation: Effects of realistic partial melt distribution. *Journal of Geophysical Research: Solid Earth*, *105*(B5), 10987-10999.

Hooft, E. E. E., Detrick, R. S., Toomey, D. R., Collins, J. A., & Lin, J. (2000). Crustal thickness and structure along three contrasting spreading segments of the Mid-Atlantic Ridge, 33.5°–35° N. *Journal of Geophysical Research: Solid Earth*, *105*(B4), 8205-8226.

Ismaïl, W. B., & Mainprice, D. (1998). An olivine fabric database: an overview of upper mantle fabrics and seismic anisotropy. *Tectonophysics*, *296*(1-2), 145-157.

Karato, S. I. (1993). Importance of anelasticity in the interpretation of seismic tomography. *Geophysical Research Letters*, *20*(15), 1623-1626.

Karsten, J. L., Hammond, S. R., Davis, E. E., & Currie, R. G. (1986). Detailed geomorphology and neotectonics of the Endeavour Segment, Juan de Fuca Ridge: New results from Seabeam swath mapping. *Geological Society of America Bulletin*, *97*(2), 213-221.

Karsten, J. L., Delaney, J. R., Rhodes, J. M., & Liias, R. A. (1990). Spatial and temporal evolution of magmatic systems beneath the Endeavour Segment, Juan de Fuca Ridge: Tectonic and petrologic constraints. *Journal of Geophysical Research: Solid Earth*, *95*(B12), 19235-19256.

Kent, G. M., Harding, A. J., & Orcutt, J. A. (1993). Distribution of magma beneath the East Pacific Rise between the Clipperton transform and the 9° 17′ N Deval from forward modeling of common depth point data. *Journal of Geophysical Research: Solid Earth*, *98*(B8), 13945-13969.

Kent, G. M., Singh, S. C., Harding, A. J., Sinha, M. C., Orcutt, J. A., Barton, P. J., ... & Pye, J. W. (2000). Evidence from three-dimensional seismic reflectivity images for enhanced melt supply beneath mid-ocean-ridge discontinuities. *Nature*, *406*(6796), 614.

Langmuir, C. H., Bender, J. F., & Batiza, R. (1986). Petrological and tectonic segmentation of the East Pacific Rise, 5° 30′–14° 30′ N. *Nature*, *322*(6078), 422.

Lonsdale, P. (1989). Segmentation of the Pacific-Nazca spreading center, 1° N–20° S. *Journal of Geophysical Research: Solid Earth*, *94*(B9), 12197-12225.

Macdonald, K. C., Fox, P. J., Perram, L. J., Eisen, M. F., Haymon, R. M., Miller, S. P., ... & Shor, A. N. (1988). A new view of the mid-ocean ridge from the behaviour of ridge-axis discontinuities. *Nature*, *335*(6187), 217.

Magde, L. S., & Sparks, D. W. (1997). Three-dimensional mantle upwelling, melt generation, and melt migration beneath segment slow spreading ridges. *Journal of Geophysical Research: Solid Earth*, *102*(B9), 20571-20583.

Marjanović, M., Carbotte, S. M., Nedimović, M. R., & Canales, J. P. (2011). Gravity and seismic study of crustal structure along the Juan de Fuca Ridge axis and across pseudofaults on the ridge flanks. *Geochemistry, Geophysics, Geosystems*, *12*(5).

Morgan, J. P., & Chen, Y. J. (1993). The genesis of oceanic crust: Magma injection, hydrothermal circulation, and crustal flow. *Journal of Geophysical Research: Solid Earth*, *98*(B4), 6283-6297.

Morgan, J. P., & Sandwell, D. T. (1994). Systematics of ridge propagation south of 30° S. *Earth and Planetary Science Letters*, *121*(1-2), 245-258.

Moser, T. J. (1991). Shortest path calculation of seismic rays. *Geophysics*, *56*(1), 59-67.

Nedimović, M. R., Carbotte, S. M., Harding, A. J., Detrick, R. S., Canales, J. P., Diebold, J. B., ... & Babcock, J. M. (2005). Frozen magma lenses below the oceanic crust. *Nature*, *436*(7054), 1149.

Neumann, G. A., & Forsyth, D. W. (1993). The paradox of the axial profile: Isostatic compensation along the axis of the Mid-Atlantic Ridge?. *Journal of Geophysical Research: Solid Earth*, *98*(B10), 17891-17910.

Nicolas, A., & Christensen, N. I. (1987). Formation of anisotropy in upper mantle peridotites-A review. *Composition, structure and dynamics of the lithosphere-asthenosphere system*, *16*, 111-123.

Pockalny, R. A., Fox, P. J., Fornari, D. J., Macdonald, K. C., & Perfit, M. R. (1997). Tectonic reconstruction of the Clipperton and Siqueiros Fracture Zones: Evidence and consequences of plate motion change for the last 3 Myr. *Journal of Geophysical Research: Solid Earth*, *102*(B2), 3167-3181.

Pollard, D. D., Segall, P., & Delaney, P. T. (1982). Formation and interpretation of dilatant echelon cracks. *Geological Society of America Bulletin*, *93*(12), 1291-1303.

Schouten, H., Klitgord, K. D., & Whitehead, J. A. (1985). Segmentation of mid-ocean ridges. *Nature*, *317*(6034), 225.

Sempéré, J. C., Purdy, G. M., & Schouten, H. (1990). Segmentation of the Mid-Atlantic Ridge between 24° N and 30° 40'N. *Nature*, *344*(6265), 427.

Shearer, P. M., & Orcutt, J. A. (1986). Compressional and shear wave anisotropy in the oceanic lithosphere-the Ngendei seismic refraction experiment. *Geophysical Journal of the Royal Astronomical Society*, *87*(3), 967-1003.

Shoberg, T., & Stein, S. (1994). Investigation of spreading center evolution by joint inversion of seafloor magnetic anomaly and tectonic fabric data. *Earth and planetary science letters*, *122*(1), 195-206.

Sinton, J. M., Wilson, D. S., Christie, D. M., Hey, R. N., & Delaney, J. R. (1983). Petrologic consequences of rift propagation on oceanic spreading ridges. *Earth and Planetary Science Letters*, *62*(2), 193-207.

Sloan, H., & Patriat, P. (1992). Kinematics of the North American-African plate boundary between 28° and 29° N during the last 10 Ma: Evolution of the axial geometry and spreading rate and direction. *Earth and Planetary Science Letters*, *113*(3), 323-341.

Soule, D., Wilcock, W. S., Toomey, D. R., Hooft, E. E., & Weekly, R. T. (2016). Near-axis crustal structure and thickness of the Endeavour Segment, Juan de Fuca Ridge. *Geophysical Research Letters*, *43*(11), 5688-5695.

Sparks, D. W., & Parmentier, E. M. (1991). Melt extraction from the mantle beneath spreading centers. *Earth and Planetary Science Letters*, *105*(4), 368-377.

Taylor, J. R (1994). An Introduction to Error Analysis: The study of uncertainties in physical measurements. *University Science Books*.

Toomey, D. R., & Foulger, G. R. (1989). Tomographic inversion of local earthquake data from the Hengill-Grensdalur central volcano complex, Iceland. *Journal of Geophysical Research: Solid Earth*, *94*(B12), 17497-17510.

Toomey, D. R., Solomon, S. C., & Purdy, G. M. (1994). Tomographic imaging of the shallow crustal structure of the East Pacific Rise at 9° 30′ N. *Journal of Geophysical Research: Solid Earth*, *99*(B12), 24135-24157.

Toomey, D. R., Jousselin, D., Dunn, R. A., Wilcock, W. S., & Detrick, R. S. (2007). Skew of mantle upwelling beneath the East Pacific Rise governs segmentation. *Nature*, *446*(7134), 409.

Toomey, D. R., & Hooft, E. E. (2008). Mantle upwelling, magmatic differentiation, and the meaning of axial depth at fast-spreading ridges. *Geology*, *36*(9), 679-682.

Wanless, V. D., Perfit, M. R., Klein, E. M., White, S., & Ridley, W. I. (2012). Reconciling geochemical and geophysical observations of magma supply and melt distribution at the 9 N overlapping spreading center, East Pacific Rise. *Geochemistry, Geophysics, Geosystems*, *13*(11).

White, S. M., Haymon, R. M., Fornari, D. J., Perfit, M. R. & Macdonald, K. C. Correlation between volcanic and tectonic segmentation of fast-spreading ridges: Evidence from volcanic structures and lava flow morphology on the East Pacific Rise at 9^{o}-10^{o}N. *J. Geophys. Res.* 107, B8–2173 (2002).

Wilson, D. S. (1988). Tectonic history of the Juan de Fuca Ridge over the last 40 million years. *Journal of Geophysical Research: Solid Earth*, *93*(B10), 11863-11876.

Weekly, R. T., Wilcock, W. S., Toomey, D. R., Hooft, E. E., & Kim, E. (2014). Upper crustal seismic structure of the Endeavour segment, Juan de Fuca Ridge from traveltime tomography: Implications for oceanic crustal accretion. *Geochemistry, Geophysics, Geosystems*, *15*(4), 1296-1315.

Zha, Y., Webb, S. C., Wei, S. S., Wiens, D. A., Blackman, D. K., Menke, W., ... & Conder, J. A. (2014). Seismological imaging of ridge–arc interaction beneath the Eastern Lau Spreading Center from OBS ambient noise tomography. *Earth and Planetary Science Letters*, *408*, 194-206.

Zhang, S., & Karato, S. I. (1995). Lattice preferred orientation of olivine aggregates deformed in simple shear. *Nature*, *375*(6534), 774.

Zhang, Z., Shen, Y., & Zhao, L. (2007). Finite-frequency sensitivity kernels for head waves. *Geophysical Journal International*, *171*(2), 847-856.

Chapter III

Backus, G. E. (1965). Possible forms of seismic anisotropy of the uppermost mantle under oceans. *Journal of Geophysical Research*, *70*(14), 3429-3439.

Becker, T. W., Chevrot, S., Schulte-Pelkum, V., and Blackman, D. K. (2006). Statistical properties of seismic anisotropy predicted by upper mantle geodynamic models. *Journal of Geophysical Research: Solid Earth*, *111*(B8).

Becker, T. W., Conrad, C. P., Schaeffer, A. J., and Lebedev, S. (2014). Origin of azimuthal seismic anisotropy in oceanic plates and mantle. *Earth and Planetary Science Letters*, *401*, 236-250.

Bell, S. W., Ruan, Y., and Forsyth, D. W. (2015). Shear velocity structure of abyssal plain sediments in Cascadia. *Seismological Research Letters*.

Blackman, D. K. and Kendall, J. M. (2002). Seismic anisotropy of the upper mantle 2. Predictions for current plate boundary flow models. *Geochemistry, Geophysics, Geosystems*, *3*(9), 1-24.

Bodmer, M., Toomey, D. R., Hooft, E. E., Nábělek, J., and Braunmiller, J. (2015). Seismic anisotropy beneath the Juan de Fuca plate system: Evidence for heterogeneous mantle flow. *Geology*, *43*(12), 1095-1098.

Boneh, Y., and Skemer, P. (2014). The effect of deformation history on the evolution of olivine CPO. *Earth and Planetary Science Letters*, *406*, 213-222.

Boneh, Y., Morales, L. F., Kaminski, E., and Skemer, P. (2015). Modeling olivine CPO evolution with complex deformation histories: Implications for the interpretation of seismic anisotropy in the mantle. *Geochemistry, Geophysics, Geosystems*, 16(10), 3436-3455.

Braunmiller, J., and Nábělek, J. (2008). Segmentation of the Blanco Transform Fault Zone from earthquake analysis: Complex tectonics of an oceanic transform fault. *Journal of Geophysical Research: Solid Earth*, *113*(B7).

Divins, D.L. (2003). Total Sediment Thickness of the World's Oceans and Marginal Seas. *NOAA National Geophysical Data Center*, Boulder, CO.

Dunn, R. A., Lekić, V., Detrick, R. S., and Toomey, D. R. (2005). Three-dimensional seismic structure of the Mid-Atlantic Ridge (35 N): Evidence for focused melt supply and lower crustal dike injection. *Journal of Geophysical Research: Solid Earth*, 110(B9).

Embley, R. W., and Wilson, D. S. (1992). Morphology of the Blanco Transform Fault Zone-NE Pacific: implications for its tectonic evolution. *Marine Geophysical Research*, *14*(1), 25-45.

Francis, T. J. G. (1969). Generation of seismic anisotropy in the upper mantle along the mid-oceanic ridges. *Nature*, *221*(5176), 162-165.

Gaherty, J. B., Lizarralde, D., Collins, J. A., Hirth, G., and Kim, S. (2004). Mantle deformation during slow seafloor spreading constrained by observations of seismic anisotropy in the western Atlantic. *Earth and Planetary Science Letters*, *228*(3), 255-265.

Gripp, A. E., and Gordon, R. G. (2002). Young tracks of hotspots and current plate velocities. *Geophysical Journal International*, *150*(2), 321-361.

Hamilton, E. L. (1979). V p/V s and Poisson's ratios in marine sediments and rocks. *The Journal of the Acoustical Society of America*, *66*(4), 1093-1101.

Hearn, T., Beghoul, N., and Barazangi, M. (1991). Tomography of the western United States from regional arrival times. *Journal of Geophysical Research: Solid Earth*, *96*(B10), 16369-16381.

Hess, H. H. (1964). Seismic anisotropy of the uppermost mantle under oceans. *Nature*, *203*(4945), 629-631.

Horning, G., Canales, J. P., Carbotte, S. M., Han, S., Carton, H., Nedimović, M. R., and Keken, P. E. (2016). A 2-D tomographic model of the Juan de Fuca plate from accretion at axial seamount to subduction at the Cascadia margin from an active source ocean bottom seismometer survey. *Journal of Geophysical Research: Solid Earth*, *121*(8), 5859-5879.

Karato, S. I. (1993). Importance of anelasticity in the interpretation of seismic tomography. *Geophysical Research Letters*, *20*(15), 1623-1626.

Karato, S. I., Jung, H., Katayama, I., and Skemer, P. (2008). Geodynamic significance of seismic anisotropy of the upper mantle: new insights from laboratory studies. *Annu. Rev. Earth Planet. Sci.*, *36*, 59-95.

Lin, P. Y. P., Gaherty, J. B., Jin, G., Collins, J. A., Lizarralde, D., Evans, R. L., and Hirth, G. (2016). High-resolution seismic constraints on flow dynamics in the oceanic asthenosphere. *Nature*, *535*(7613), 538-541.

Martin-Short, R., Allen, R. M., Bastow, I. D., Totten, E., and Richards, M. A. (2015). Mantle flow geometry from ridge to trench beneath the Gorda-Juan de Fuca plate system. *Nature Geoscience*, *8*(12), 965.

Morris, G. B., Raitt, R. W., and Shor, G. G. (1969). Velocity anisotropy and delay-time maps of the mantle near Hawaii. *Journal of Geophysical Research*, *74*(17), 4300-4316.

Nicolas, A., and Violette, J. F. (1982). Mantle flow at oceanic spreading centers: models derived from ophiolites. *Tectonophysics*, 81(3-4), 319-339.

Nicolas, A., and Christensen, N. I. (1987). Formation of Anisotropy in Upper Mantle Peridotites-A Review. *Composition, structure and dynamics of the lithosphere-asthenosphere system*, 111-123.

Pei, S., Zhao, J., Sun, Y., Xu, Z., Wang, S., Liu, H., Rowe, C.A., Toksöz, M.N. and Gao, X., 2007. Upper mantle seismic velocities and anisotropy in China determined through Pn and Sn tomography. *Journal of Geophysical Research: Solid Earth*, *112*(B5).

Raitt, R. W., Shor, G. G., Francis, T. J. G., and Morris, G. B. (1969). Anisotropy of the Pacific upper mantle. *Journal of Geophysical Research*, *74*(12), 3095-3109.

Ribe, N. M. (1989). Seismic anisotropy and mantle flow. *Journal of Geophysical Research: Solid Earth*, *94*(B4), 4213-4223.

Riddihough, R. (1984). Recent movements of the Juan de Fuca plate system. *Journal of Geophysical Research: Solid Earth*, *89*(B8), 6980-6994.

Ruan, Y., Forsyth, D. W., and Bell, S. W. (2014). Marine sediment shear velocity structure from the ratio of displacement to pressure of Rayleigh waves at seafloor. *Journal of Geophysical Research: Solid Earth*, *119*(8), 6357-6371.

Rümpker, G., Tommasi, A., and Kendall, J. (1999). Numerical simulations of depth-dependent anisotropy and frequency-dependent wave propagation effects. Journal of Geophysical Research: Solid Earth, 104(B10), 23141-23153.

Shearer, P. M., and Orcutt, J. A. (1986). Compressional and shear wave anisotropy in the oceanic lithosphere-the Ngendei seismic refraction experiment. *Geophysical Journal International*, *87*(3), 967-1003.

Shintaku, N., Forsyth, D. W., Hajewski, C. J., and Weeraratne, D. S. (2014). Pn anisotropy in Mesozoic western Pacific lithosphere. *Journal of Geophysical Research: Solid Earth*, *119*(4), 3050-3063.

Shito, A., Suetsugu, D., Furumura, T., Sugioka, H., and Ito, A. (2013). Small-scale heterogeneities in the oceanic lithosphere inferred from guided waves. *Geophysical Research Letters*, *40*(9), 1708-1712.

Song, T. R. A., and Kim, Y. (2012). Anisotropic uppermost mantle in young subducted slab underplating Central Mexico. *Nature Geoscience*, *5*(1), 55.

Takeo, A., Forsyth, D. W., Weeraratne, D. S., and Nishida, K. (2014). Estimation of azimuthal anisotropy in the NW Pacific from seismic ambient noise in seafloor records. *Geophysical Journal International*, *199*(1), 11-22.

Tommasi, A. (1998). Forward modeling of the development of seismic anisotropy in the upper mantle. Earth and Planetary Science Letters, 160(1), 1-13.

Toomey, D. R., Jousselin, D., Dunn, R. A., Wilcock, W. S., and Detrick, R. S. (2007). Skew of mantle upwelling beneath the East Pacific Rise governs segmentation. *Nature*, 446(7134), 409-414.

Toomey, D.R., Allen, R.M., Barclay, A.H., Bell, S.W., Bromirski, P.D., Carlson, R.L., Chen, X., Collins, J.A., Dziak, R.P., Evers, B. and Forsyth, D.W., 2014. The Cascadia Initiative: A sea change in seismological studies of subduction zones. *Oceanography*, *27*(2), 138-150.

VanderBeek, B. P., Toomey, D. R., Hooft, E. E., and Wilcock, W. S. (2016). Segmentation of mid-ocean ridges attributed to oblique mantle divergence. *Nature Geoscience*, *9*(8), 636-642.

Warren, J. M., Hirth, G., and Kelemen, P. B. (2008). Evolution of olivine lattice preferred orientation during simple shear in the mantle. *Earth and Planetary Science Letters*, 272(3), 501-512.

Williams, S. E., Flament, N., and Müller, R. D. (2016). Alignment between seafloor spreading directions and absolute plate motions through time. *Geophysical Research Letters*, *43*(4), 1472-1480.

Wilson, D. S. (1988). Tectonic history of the Juan de Fuca Ridge over the last 40 million years. *Journal of Geophysical Research: Solid Earth*, *93*(B10), 11863-11876.

Wolfe, C. J., and Solomon, S. C. (1998). Shear-wave splitting and implications for mantle flow beneath the MELT region of the East Pacific Rise. *Science*, 280(5367), 1230-1232.

Zhang, S., and Karato, S. I. (1995). Lattice preferred orientation of olivine aggregates deformed in simple shear. *Nature*, *375*(6534), 774-777.

Zhang, Z., Shen, Y., and Zhao, L. (2007). Finite-frequency sensitivity kernels for head waves. *Geophysical Journal International*, *171*(2), 847-856.

Chapter IV

Abers, G. A., van Keken, P. E., & Hacker, B. R. (2017). The cold and relatively dry nature of mantle forearcs in subduction zones. *Nature Geoscience*, *10*(5), 333.

Backus, G. E. (1965). Possible forms of seismic anisotropy of the uppermost mantle under oceans. *Journal of Geophysical Research*, *70*(14), 3429-3439.

Becker, T. W., Chevrot, S., Schulte-Pelkum, V., and Blackman, D. K. (2006). Statistical properties of seismic anisotropy predicted by upper mantle geodynamic models. *Journal of Geophysical Research: Solid Earth*, *111*(B8).

Bell, S. W., Ruan, Y., and Forsyth, D. W. (2015). Shear velocity structure of abyssal plain sediments in Cascadia. *Seismological Research Letters*.

Bell, S., Ruan, Y., & Forsyth, D. W. (2016). Ridge asymmetry and deep aqueous alteration at the trench observed from Rayleigh wave tomography of the Juan de Fuca plate. *Journal of Geophysical Research: Solid Earth*, *121*(10), 7298-7321.

Blackman, D. K. and Kendall, J. M. (2002). Seismic anisotropy of the upper mantle 2. Predictions for current plate boundary flow models. *Geochemistry, Geophysics, Geosystems*, *3*(9), 1-24.

Bodmer, M., Toomey, D. R., Hooft, E. E., Nábělek, J., and Braunmiller, J. (2015). Seismic anisotropy beneath the Juan de Fuca plate system: Evidence for heterogeneous mantle flow. *Geology*, *43*(12), 1095-1098.

Braunmiller, J., and Nábělek, J. (2008). Segmentation of the Blanco Transform Fault Zone from earthquake analysis: Complex tectonics of an oceanic transform fault. *Journal of Geophysical Research: Solid Earth*, *113*(B7).

Buehler, J. S., & Shearer, P. M. (2010). Pn tomography of the western United States using USArray. *Journal of Geophysical Research: Solid Earth*, *115*(B9).

Byrnes, J. S., Toomey, D. R., Hooft, E. E., Nábělek, J., & Braunmiller, J. (2017). Mantle dynamics beneath the discrete and diffuse plate boundaries of the J uan de F uca plate: Results from C ascadia I nitiative body wave tomography. *Geochemistry, Geophysics, Geosystems*, *18*(8), 2906-2929.

Canales, P. J., Detrick, R. S., Toomey, D. R., & Wilcock, W. S. (2003). Segment-scale variations in the crustal structure of 150–300 kyr old fast spreading oceanic crust (East Pacific Rise, 8° 15′ N–10° 5′ N) from wide-angle seismic refraction profiles. *Geophysical Journal International*, *152*(3), 766-794.

Canales, J. P., Carbotte, S. M., Nedimović, M. R., & Carton, H. (2017). Dry Juan de Fuca slab revealed by quantification of water entering Cascadia subduction zone. *Nature Geoscience*, *10*(11), 864.

Chadwick Jr, W. W., Embley, R. W., & Shank, T. M. (1998). The 1996 Gorda Ridge eruption: Geologic mapping, sidescan sonar, and SeaBeam comparison results. *Deep Sea Research Part II: Topical Studies in Oceanography*, *45*(12), 2547-2569.

Chaytor, J. D., Goldfinger, C., Dziak, R. P., & Fox, C. G. (2004). Active deformation of the Gorda plate: Constraining deformation models with new geophysical data. *Geology*, *32*(4), 353-356.

Chen, C., Zhao, D., & Wu, S. (2015). Tomographic imaging of the Cascadia subduction zone: constraints on the Juan de Fuca slab. *Tectonophysics*, *647*, 73-88.

Crampin, S. (1993). A review of the effects of crack geometry on wave propagation through aligned. *Can. J. Exp. Geophys.*, *29*, 3-17.

Davis, A. S., & Clague, D. A. (1987). Geochemistry, mineralogy, and petrogenesis of basalt from the Gorda Ridge. *Journal of Geophysical Research: Solid Earth*, *92*(B10), 10467-10483.

Davis, A. S., Clague, D. A., Cousens, B. L., Keaten, R., & Paduan, J. B. (2008). Geochemistry of basalt from the North Gorda segment of the Gorda Ridge: Evolution toward ultraslow spreading ridge lavas due to decreasing magma supply. *Geochemistry, Geophysics, Geosystems*, *9*(4).

Dickinson, W. R., & Snyder, W. S. (1979). Geometry of triple junctions related to San Andreas transform. *Journal of Geophysical Research: Solid Earth*, *84*(B2), 561-572.

Dijkstra, E. W. (1959). A note on two problems in connexion with graphs. *Numerische mathematik*, *1*(1), 269-271.

Divins, D. L. (2003). Total Sediment Thickness of the World\'s Oceans and Marginal Seas.

Dunn, R. A., & Toomey, D. R. (2001). Crack-induced seismic anisotropy in the oceanic crust across the East Pacific Rise (9 30′ N). *Earth and Planetary Science Letters*, *189*(1-2), 9-17.

Dunn, R. A., Lekić, V., Detrick, R. S., and Toomey, D. R. (2005). Three-dimensional seismic structure of the Mid-Atlantic Ridge (35 N): Evidence for focused melt supply and lower crustal dike injection. *Journal of Geophysical Research: Solid Earth*, 110(B9).

Dziak, R. P., Fox, C. G., Bobbitt, A. M., & Goldfinger, C. (2001). Bathymetric map of the Gorda Plate: Structural and geomorphological processes inferred from multibeam surveys. *Marine Geophysical Researches*, *22*(4), 235-250.

Dziak, R. P. (2006). Explorer deformation zone: Evidence of a large shear zone and reorganization of the Pacific–Juan de Fuca–North American triple junction. *Geology*, *34*(3), 213-216.

Dziak, R. P., Hammond, S. R., & Fox, C. G. (2011). A 20-year hydroacoustic time series of seismic and volcanic events in the Northeast Pacific Ocean. *Oceanography*, *24*(3), 280-293.

Eilon, Z. C., & Abers, G. A. (2017). High seismic attenuation at a mid-ocean ridge reveals the distribution of deep melt. *Science advances*, *3*(5), e1602829.

Embley, R. W., & Wilson, D. S. (1992). Morphology of the Blanco transform fault zone-NE Pacific: Implications for its tectonic evolution. *Marine geophysical researches*, *14*(1), 25-45.

Faccenda, M., Gerya, T. V., & Burlini, L. (2009). Deep slab hydration induced by bending-related variations in tectonic pressure. *Nature Geoscience*, *2*(11), 790.

Faccenda, M. (2014). Water in the slab: A trilogy. *Tectonophysics*, *614*, 1-30.

Furlong, K. P., & Schwartz, S. Y. (2004). Influence of the Mendocino triple junction on the tectonics of coastal California. *Annu. Rev. Earth Planet. Sci.*, *32*, 403-433.

Gaherty, J. B., Lizarralde, D., Collins, J. A., Hirth, G., and Kim, S. (2004). Mantle deformation during slow seafloor spreading constrained by observations of seismic anisotropy in the western Atlantic. *Earth and Planetary Science Letters*, *228*(3), 255-265.

Gardner, J.V., Cacchione, D.A., Drake, D.E., Edwards, B.D., Field, M.E., Hampton, M.A., Karl, H.A., Kenyon, N.H., Masson, D.G., McCulloch, D.S., and Grim, M.S., 1993, Map showing sediment isopachs in the deep-sea basins of the Pacific continental margin, Strait of Juan de Fuca to Cape Mendocino: U. S. Geological Survey Miscellaneous Investigations Series Map I-2091-A, 1 sheet, scale 1:1,000,000.

Gulick, S. P., Meltzer, A. M., & Clarke Jr, S. H. (1998). Seismic structure of the southern Cascadia subduction zone and accretionary prism north of the Mendocino triple junction. *Journal of Geophysical Research: Solid Earth*, *103*(B11), 27207-27222.

Gulick, S. P., Meltzer, A. S., Henstock, T. J., & Levander, A. (2001). Internal deformation of the southern Gorda plate: Fragmentation of a weak plate near the Mendocino triple junction. *Geology*, *29*(8), 691-694.

Hacker, B. R., Abers, G. A., & Peacock, S. M. (2003a). Subduction factory 1. Theoretical mineralogy, densities, seismic wave speeds, and H2O contents. *Journal of Geophysical Research: Solid Earth*, *108*(B1).

Hacker, B. R., Peacock, S. M., Abers, G. A., & Holloway, S. D. (2003b). Subduction factory 2. Are intermediate-depth earthquakes in subducting slabs linked to metamorphic dehydration reactions?. *Journal of Geophysical Research: Solid Earth*, *108*(B1).

Han, S., Carbotte, S. M., Canales, J. P., Nedimović, M. R., Carton, H., Gibson, J. C., & Horning, G. W. (2016). Seismic reflection imaging of the Juan de Fuca plate from ridge to trench: New constraints on the distribution of faulting and evolution of the crust prior to subduction. *Journal of Geophysical Research: Solid Earth*, *121*(3), 1849-1872.

Han, S., Carbotte, S. M., Canales, J. P., Nedimović, M. R., & Carton, H. (2018). Along-Trench Structural Variations of the Subducting Juan de Fuca Plate from Multichannel Seismic Reflection Imaging. *Journal of Geophysical Research: Solid Earth*, *123*(4), 3122-3146.

Hearn, T., Beghoul, N., & Barazangi, M. (1991). Tomography of the western United States from regional arrival times. *Journal of Geophysical Research: Solid Earth*, *96*(B10), 16369-16381.

Hirschmann, M. M. (2000). Mantle solidus: Experimental constraints and the effects of peridotite composition. *Geochemistry, Geophysics, Geosystems*, *1*(10).

Hooft, E. E., & Detrick, R. S. (1995). Relationship between axial morphology, crustal thickness, and mantle temperature along the Juan de Fuca and Gorda Ridges. *Journal of Geophysical Research: Solid Earth*, *100*(B11), 22499-22508.

Horning, G., Canales, J. P., Carbotte, S. M., Han, S., Carton, H., Nedimović, M. R., & Keken, P. E. (2016). A 2-D tomographic model of the Juan de Fuca plate from accretion at axial seamount to subduction at the Cascadia margin from an active source ocean bottom seismometer survey. *Journal of Geophysical Research: Solid Earth*, *121*(8), 5859-5879.

Hudson, J. A. (1981). Wave speeds and attenuation of elastic waves in material containing cracks. *Geophysical Journal of the Royal Astronomical Society*, *64*(1), 133-150.

Isaak, D. G. (1992). High-temperature elasticity of iron-bearing olivines. *Journal of Geophysical Research: Solid Earth*, *97*(B2), 1871-1885.

Ismaïl, W. B., & Mainprice, D. (1998). An olivine fabric database: an overview of upper mantle fabrics and seismic anisotropy. *Tectonophysics*, *296*(1-2), 145-157.

Karato, S. I. (1993). Importance of anelasticity in the interpretation of seismic tomography. *Geophysical Research Letters*, *20*(15), 1623-1626.

Kennett, B. L. N., & Furumura, T. (2013). High-frequency Po/So guided waves in the oceanic lithosphere: I—long-distance propagation. *Geophysical Journal International*, *195*(3), 1862-1877.

Kennett, B. L. N., Furumura, T., & Zhao, Y. (2014). High-frequency Po/So guided waves in the oceanic lithosphere: II—heterogeneity and attenuation. *Geophysical Journal International*, *199*(1), 614-630.

Kennett, B. L. N., & Furumura, T. (2015). Toward the reconciliation of seismological and petrological perspectives on oceanic lithosphere heterogeneity. *Geochemistry, Geophysics, Geosystems*, *16*(9), 3129-3141.

Kodaira, S., Fujie, G., Yamashita, M., Sato, T., Takahashi, T., & Takahashi, N. (2014). Seismological evidence of mantle flow driving plate motions at a palaeo-spreading centre. *Nature Geoscience*, *7*(5), 371-375.

Korenaga, J. (2017). On the extent of mantle hydration caused by plate bending. *Earth and Planetary Science Letters*, *457*, 1-9.

Koulakov, I., Gordeev, E. I., Dobretsov, N. L., Vernikovsky, V. A., Senyukov, S., & Jakovlev, A. (2011). Feeding volcanoes of the Kluchevskoy group from the results of local earthquake tomography. *Geophysical research letters*, *38*(9).

Leitner, B., Tréhu, A. M., & Godfrey, N. J. (1998). Crustal structure of the northwestern Vizcaino block and Gorda Escarpment, offshore northern California, and implications for postsubduction deformation of a paleoaccretionary margin. *Journal of Geophysical Research: Solid Earth*, *103*(B10), 23795-23812.

Lizarralde, D., Gaherty, J. B., Collins, J. A., Hirth, G., & Kim, S. D. (2004). Spreading-rate dependence of melt extraction at mid-ocean ridges from mantle seismic refraction data. *Nature*, *432*(7018), 744.

Marjanović, M., Carbotte, S. M., Nedimović, M. R., & Canales, J. P. (2011). Gravity and seismic study of crustal structure along the Juan de Fuca Ridge axis and across pseudofaults on the ridge flanks. *Geochemistry, Geophysics, Geosystems*, *12*(5).

Martin-Short, R., Allen, R. M., Bastow, I. D., Totten, E., and Richards, M. A. (2015). Mantle flow geometry from ridge to trench beneath the Gorda-Juan de Fuca plate system. *Nature Geoscience*, *8*(12), 965.

McCrory, P. A., Blair, J. L., Waldhauser, F., & Oppenheimer, D. H. (2012). Juan de Fuca slab geometry and its relation to Wadati-Benioff zone seismicity. *Journal of Geophysical Research: Solid Earth*, *117*(B9).

Miller, N. C., & Lizarralde, D. (2016). Finite-frequency wave propagation through outer rise fault zones and seismic measurements of upper mantle hydration. *Geophysical Research Letters*, *43*(15), 7982-7990.

Morris, G. B., Raitt, R. W., and Shor, G. G. (1969). Velocity anisotropy and delay-time maps of the mantle near Hawaii. *Journal of Geophysical Research*, *74*(17), 4300-4316.

Moser, T. J. (1991). Shortest path calculation of seismic rays. *Geophysics*, *56*(1), 59-67.

Nedimović, M. R., Carbotte, S. M., Harding, A. J., Detrick, R. S., Canales, J. P., Diebold, J. B., ... & Babcock, J. M. (2005). Frozen magma lenses below the oceanic crust. *Nature*, *436*(7054), 1149.

Nedimović, M. R., Bohnenstiehl, D. R., Carbotte, S. M., Canales, J. P., & Dziak, R. P. (2009). Faulting and hydration of the Juan de Fuca plate system. *Earth and Planetary Science Letters*, *284*(1-2), 94-102.

Paige, C. C., & Saunders, M. A. (1982). LSQR: An algorithm for sparse linear equations and sparse least squares. *ACM Transactions on Mathematical Software (TOMS)*, *8*(1), 43-71.

Pei, S., Zhao, J., Sun, Y., Xu, Z., Wang, S., Liu, H., ... & Gao, X. (2007). Upper mantle seismic velocities and anisotropy in China determined through Pn and Sn tomography. *Journal of Geophysical Research: Solid Earth*, *112*(B5).

Paulatto, M., Laigle, M., Galve, A., Charvis, P., Sapin, M., Bayrakci, G., ... & Kopp, H. (2017). Dehydration of subducting slow-spread oceanic lithosphere in the Lesser Antilles. *Nature Communications*, *8*, 15980.

Peacock, S. M., & Hyndman, R. D. (1999). Hydrous minerals in the mantle wedge and the maximum depth of subduction thrust earthquakes. *Geophysical Research Letters*, *26*(16), 2517-2520.

Ranero, C. R., Villaseñor, A., Phipps Morgan, J., & Weinrebe, W. (2005). Relationship between bend-faulting at trenches and intermediate-depth seismicity. *Geochemistry, Geophysics, Geosystems*, *6*(12).

Riddihough, R. (1984). Recent movements of the Juan de Fuca plate system. *Journal of Geophysical Research: Solid Earth*, *89*(B8), 6980-6994.

Ruscitto, D. M., Wallace, P. J., Johnson, E. R., Kent, A. J. R., & Bindeman, I. N. (2010). Volatile contents of mafic magmas from cinder cones in the Central Oregon High Cascades: Implications for magma formation and mantle conditions in a hot arc. *Earth and Planetary Science Letters*, *298*(1-2), 153-161.

Sereno, T. J., & Orcutt, J. A. (1985). Synthetic seismogram modelling of the oceanic Pn phase. *Nature*, *316*(6025), 246.

Shearer, P., & Orcutt, J. (1985). Anisotropy in the oceanic lithosphere—theory and observations from the Ngendei seismic refraction experiment in the south-west Pacific. *Geophysical Journal International*, *80*(2), 493-526.

Shillington, D. J., Bécel, A., Nedimović, M. R., Kuehn, H., Webb, S. C., Abers, G. A., ... & Mattei-Salicrup, G. A. (2015). Link between plate fabric, hydration and subduction zone seismicity in Alaska. *Nature Geoscience*, *8*(12), 961.

Shintaku, N., Forsyth, D. W., Hajewski, C. J., & Weeraratne, D. S. (2014). Pn anisotropy in Mesozoic western Pacific lithosphere. *Journal of Geophysical Research: Solid Earth*, *119*(4), 3050-3063.

Sinton, J. M., Wilson, D. S., Christie, D. M., Hey, R. N., & Delaney, J. R. (1983). Petrologic consequences of rift propagation on oceanic spreading ridges. *Earth and Planetary Science Letters*, *62*(2), 193-207.

Soule, D., Wilcock, W. S., Toomey, D. R., Hooft, E. E., & Weekly, R. T. (2016). Near-axis crustal structure and thickness of the Endeavour Segment, Juan de Fuca Ridge. *Geophysical Research Letters*, *43*(11), 5688-5695.

Stoddard, P. R., & Woods, M. T. (1990). Master event relocation of Gorda block earthquakes: Implications for deformation. *Geophysical Research Letters*, *17*(7), 961-964.

Stoddard, P. R. (1991). A comparison of brittle deformation models for the Gorda plate. *Tectonophysics*, *187*(1-3), 205-214.

Takeuchi, N., Kawakatsu, H., Shiobara, H., Isse, T., Sugioka, H., Ito, A., & Utada, H. (2017). Determination of intrinsic attenuation in the oceanic lithosphere-asthenosphere system. *Science*, *358*(6370), 1593-1596.

Thurber, C. H. (1983). Earthquake locations and three-dimensional crustal structure in the Coyote Lake area, central California. *Journal of Geophysical Research: Solid Earth*, *88*(B10), 8226-8236.

Toomey, D. R., Solomon, S. C., & Purdy, G. M. (1994). Tomographic imaging of the shallow crustal structure of the East Pacific Rise at 9° 30′ N. *Journal of Geophysical Research: Solid Earth*, *99*(B12), 24135-24157.

Toomey, D. R., Jousselin, D., Dunn, R. A., Wilcock, W. S., & Detrick, R. S. (2007). Skew of mantle upwelling beneath the East Pacific Rise governs segmentation. *Nature*, *446*(7134), 409.

Toomey, D. R., & Hooft, E. E. (2008). Mantle upwelling, magmatic differentiation, and the meaning of axial depth at fast-spreading ridges. *Geology*, *36*(9), 679-682.

VanderBeek, B. P., Toomey, D. R., Hooft, E. E., & Wilcock, W. S. (2016). Segmentation of mid-ocean ridges attributed to oblique mantle divergence. *Nature Geoscience*, *9*(8), 636.

VanderBeek, B. P., & Toomey, D. R. (2017). Shallow mantle anisotropy beneath the Juan de Fuca plate. *Geophysical Research Letters*, *44*(22).

van Keken, P. E., Hacker, B. R., Syracuse, E. M., & Abers, G. A. (2011). Subduction factory: 4. Depth-dependent flux of H2O from subducting slabs worldwide. *Journal of Geophysical Research: Solid Earth*, *116*(B1).

Walowski, K. J., Wallace, P. J., Hauri, E. H., Wada, I., & Clynne, M. A. (2015). Slab melting beneath the Cascade Arc driven by dehydration of altered oceanic peridotite. *Nature Geoscience*, *8*(5), 404.

Wanless, V. D., Perfit, M. R., Klein, E. M., White, S., & Ridley, W. I. (2012). Reconciling geochemical and geophysical observations of magma supply and melt distribution at the 9 N overlapping spreading center, East Pacific Rise. *Geochemistry, Geophysics, Geosystems*, *13*(11).

Weekly, R. T., Wilcock, W. S., Toomey, D. R., Hooft, E. E., & Kim, E. (2014). Upper crustal seismic structure of the Endeavour segment, Juan de Fuca Ridge from traveltime tomography: Implications for oceanic crustal accretion. *Geochemistry, Geophysics, Geosystems*, *15*(4), 1296-1315.

Wilson, D. S., Hey, R. N., & Nishimura, C. (1984). Propagation as a mechanism of reorientation of the Juan de Fuca Ridge. *Journal of Geophysical Research: Solid Earth*, *89*(B11), 9215-9225.

Wilson, D. S. (1986). A kinematic model for the Gorda deformation zone as a diffuse southern boundary of the Juan de Fuca plate. *Journal of Geophysical Research: Solid Earth*, *91*(B10), 10259-10269.

Wilson, D. S. (1989). Deformation of the so-called Gorda plate. *Journal of Geophysical Research: Solid Earth*, *94*(B3), 3065-3075.

Wilson, D. S. (1993). Confidence intervals for motion and deformation of the Juan de Fuca plate. *Journal of Geophysical Research: Solid Earth*, *98*(B9), 16053-16071.

Yuan, T., Spence, G. D., & Hyndman, R. D. (1994). Seismic velocities and inferred porosities in the accretionary wedge sediments at the Cascadia margin. *Journal of Geophysical Research: Solid Earth*, *99*(B3), 4413-4427.

Zhang, Z., Shen, Y., & Zhao, L. (2007). Finite-frequency sensitivity kernels for head waves. *Geophysical Journal International*, *171*(2), 847-856.

Zhao, D., Hasegawa, A., & Horiuchi, S. (1992). Tomographic imaging of P and S wave velocity structure beneath northeastern Japan. *Journal of Geophysical Research: Solid Earth*, *97*(B13), 19909-19928.

Chapter V

Baba, K., Chave, A. D., Evans, R. L., Hirth, G., & Mackie, R. L. (2006). Mantle dynamics beneath the East Pacific Rise at 17 S: Insights from the Mantle Electromagnetic and Tomography (MELT) experiment. *Journal of Geophysical Research: Solid Earth*, *111*(B2).

Bell, S., Ruan, Y., & Forsyth, D. W. (2016). Ridge asymmetry and deep aqueous alteration at the trench observed from Rayleigh wave tomography of the Juan de Fuca plate. *Journal of Geophysical Research: Solid Earth*, *121*(10), 7298-7321.

Bodmer, M., Toomey, D. R., Hooft, E. E., & Schmandt, B. (2018). Buoyant Asthenosphere Beneath Cascadia Influences Megathrust Segmentation. *Geophysical Research Letters*.

Brown, J. W., & White, R. S. (1994). Variation with spreading rate of oceanic crustal thickness and geochemistry. *Earth and Planetary Science Letters*, *121*(3-4), 435-449.

Buck, W. R., & Su, W. (1989). Focused mantle upwelling below mid-ocean ridges due to feedback between viscosity and melting. *Geophysical Research Letters*, *16*(7), 641-644.

Byrnes, J. S., Toomey, D. R., Hooft, E. E., Nábělek, J., & Braunmiller, J. (2017). Mantle dynamics beneath the discrete and diffuse plate boundaries of the J uan de F uca plate: Results from C ascadia I nitiative body wave tomography. *Geochemistry, Geophysics, Geosystems*, *18*(8), 2906-2929.

Choblet, G., & Parmentier, E. M. (2001). Mantle upwelling and melting beneath slow spreading centers: Effects of variable rheology and melt productivity. *Earth and Planetary Science Letters*, *184*(3-4), 589-604.

Conder, J. A., Wiens, D. A., & Morris, J. (2002). On the decompression melting structure at volcanic arcs and back-arc spreading centers. *Geophysical Research Letters*, *29*(15), 17-1.

Dahlen, F. A., Hung, S. H., & Nolet, G. (2000). Fréchet kernels for finite-frequency traveltimes—I. Theory. *Geophysical Journal International*, *141*(1), 157-174.

Dasgupta, R., Mallik, A., Tsuno, K., Withers, A. C., Hirth, G., & Hirschmann, M. M. (2013). Carbon-dioxide-rich silicate melt in the Earth's upper mantle. *Nature*, *493*(7431), 211.

Dijkstra, E. W. (1959). A note on two problems in connexion with graphs. *Numerische mathematik*, *1*(1), 269-271.

Dunn, R. A., & Forsyth, D. W. (2003). Imaging the transition between the region of mantle melt generation and the crustal magma chamber beneath the southern East Pacific Rise with short-period Love waves. *Journal of Geophysical Research: Solid Earth*, *108*(B7).

Eilon, Z. C., & Abers, G. A. (2017). High seismic attenuation at a mid-ocean ridge reveals the distribution of deep melt. *Science advances*, *3*(5), e1602829.

Evans, R. L., Tarits, P., Chave, A. D., White, A., Heinson, G., Filloux, J. H., ... & Unsworth, M. J. (1999). Asymmetric electrical structure in the mantle beneath the East Pacific Rise at 17 S. *Science*, *286*(5440), 752-756.

Forsyth, D. W., Webb, S. C., Dorman, L. M., & Shen, Y. (1998). Phase velocities of Rayleigh waves in the MELT experiment on the East Pacific Rise. *Science*, *280*(5367), 1235-1238.

Forsyth, D. W., & Li, A. (2005). Array analysis of two-dimensional variations in surface wave phase velocity and azimuthal anisotropy in the presence of multipathing interference. *Seismic Earth: Array Analysis of Broadband Seismograms*, *157*, 81-97.

Gao, H. (2016). Seismic velocity structure of the Juan de Fuca and Gorda plates revealed by a joint inversion of ambient noise and regional earthquakes. *Geophysical Research Letters*, *43*(10), 5194-5201.

Golos, E. M., Fang, H., Yao, H., Zhang, H., Burdick, S., Vernon, F., ... & van der Hilst, R. D. (2018). Shear Wave Tomography Beneath the United States Using a Joint Inversion of Surface and Body Waves. *Journal of Geophysical Research: Solid Earth*, *123*(6), 5169-5189.

Hammond, W. C., & Toomey, D. R. (2003). Seismic velocity anisotropy and heterogeneity beneath the Mantle Electromagnetic and Tomography Experiment (MELT) region of the East Pacific Rise from analysis of P and S body waves. *Journal of Geophysical Research: Solid Earth*, *108*(B4).

Harmon, N., Forsyth, D. W., Fischer, K. M., & Webb, S. C. (2004). Variations in shear-wave splitting in young Pacific seafloor. *Geophysical research letters*, *31*(15).

Harmon, N., Forsyth, D. W., & Scheirer, D. S. (2006). Analysis of gravity and topography in the GLIMPSE study region: Isostatic compensation and uplift of the Sojourn and Hotu Matua Ridge systems. *Journal of Geophysical Research: Solid Earth*, *111*(B11).

Harmon, N., Forsyth, D. W., & Weeraratne, D. S. (2009). Thickening of young Pacific lithosphere from high-resolution Rayleigh wave tomography: A test of the conductive cooling model. *Earth and Planetary Science Letters*, *278*(1-2), 96-106.

Hawley, W. B., Allen, R. M., & Richards, M. A. (2016). Tomography reveals buoyant asthenosphere accumulating beneath the Juan de Fuca plate. *Science*, *353*(6306), 1406-1408.

Hirth, G., & Kohlstedt, D. L. (1996). Water in the oceanic upper mantle: implications for rheology, melt extraction and the evolution of the lithosphere. *Earth and Planetary Science Letters*, *144*(1-2), 93-108.

Katz, R. F. (2010). Porosity-driven convection and asymmetry beneath mid-ocean ridges. *Geochemistry, Geophysics, Geosystems*, *11*(11).

Key, K., Constable, S., Liu, L., & Pommier, A. (2013). Electrical image of passive mantle upwelling beneath the northern East Pacific Rise. *Nature*, *495*(7442), 499.

Langmuir, C. H., Klein, E. M., & Plank, T. (1992). Petrological systematics of mid-ocean ridge basalts: Constraints on melt generation beneath ocean ridges. *Mantle Flow and Melt Generation at Mid-Ocean Ridges*, *71*, 183-280.

Marquering, H., Dahlen, F. A., & Nolet, G. (1999). Three-dimensional sensitivity kernels for finite-frequency traveltimes: the banana-doughnut paradox. *Geophysical Journal International*, *137*(3), 805-815.

Moser, T. J. (1991). Shortest path calculation of seismic rays. *Geophysics*, *56*(1), 59-67.

Obrebski, M., Allen, R. M., Pollitz, F., & Hung, S. H. (2011). Lithosphere–asthenosphere interaction beneath the western United States from the joint inversion of body-wave traveltimes and surface-wave phase velocities. *Geophysical Journal International*, *185*(2), 1003-1021.

Paige, C. C., & Saunders, M. A. (1982). LSQR: An algorithm for sparse linear equations and sparse least squares. *ACM Transactions on Mathematical Software (TOMS)*, *8*(1), 43-71.

Saito, M. A. S. A. N. O. R. I. (1988). DISPER80: A subroutine package for the calculation of seismic normal-mode solutions. *Seismological algorithms*, 293-319.

Schmandt, B., & Humphreys, E. (2010). Complex subduction and small-scale convection revealed by body-wave tomography of the western United States upper mantle. *Earth and Planetary Science Letters*, *297*(3-4), 435-445.

Scott, D. R., & Stevenson, D. J. (1989). A self-consistent model of melting, magma migration and buoyancy-driven circulation beneath mid-ocean ridges. *Journal of Geophysical Research: Solid Earth*, *94*(B3), 2973-2988.

Spetzler, J., & Snieder, R. (2001). The effect of small scale heterogeneity on the arrival time of waves. *Geophysical Journal International*, *145*(3), 786-796.

Spiegelman, M., & McKenzie, D. (1987). Simple 2-D models for melt extraction at mid-ocean ridges and island arcs. *Earth and Planetary Science Letters*, *83*(1-4), 137-152.

Stixrude, L., & Lithgow-Bertelloni, C. (2005). Mineralogy and elasticity of the oceanic upper mantle: Origin of the low-velocity zone. *Journal of Geophysical Research: Solid Earth*, *110*(B3).

Tian, Y., Shen, W., & Ritzwoller, M. H. (2013). Crustal and uppermost mantle shear velocity structure adjacent to the Juan de Fuca Ridge from ambient seismic noise. *Geochemistry, Geophysics, Geosystems*, *14*(8), 3221-3233.

Toomey, D. R., Solomon, S. C., & Purdy, G. M. (1994). Tomographic imaging of the shallow crustal structure of the East Pacific Rise at 9° 30′ N. *Journal of Geophysical Research: Solid Earth*, *99*(B12), 24135-24157.

Toomey, D. R., Wilcock, W. S. D., Conder, J. A., Forsyth, D. W., Blundy, J. D., Parmentier, E. M., & Hammond, W. C. (2002). Asymmetric mantle dynamics in the MELT region of the East Pacific Rise. *Earth and Planetary Science Letters*, *200*(3-4), 287-295.

Toomey, D. R., Jousselin, D., Dunn, R. A., Wilcock, W. S., & Detrick, R. S. (2007). Skew of mantle upwelling beneath the East Pacific Rise governs segmentation. *Nature*, *446*(7134), 409.

Toomey, D. R., Allen, R. M., Barclay, A. H., Bell, S. W., Bromirski, P. D., Carlson, R. L., ... & Forsyth, D. W. (2014). The Cascadia Initiative: A sea change in seismological studies of subduction zones. *Oceanography*, *27*(2), 138-150.

VanDecar, J. C., & Crosson, R. S. (1990). Determination of teleseismic relative phase arrival times using multi-channel cross-correlation and least squares. *Bulletin of the Seismological Society of America*, *80*(1), 150-169.

VanderBeek, B. P., Toomey, D. R., Hooft, E. E., & Wilcock, W. S. (2016). Segmentation of mid-ocean ridges attributed to oblique mantle divergence. *Nature Geoscience*, *9*(8), 636.

Villagómez, D. R., Toomey, D. R., Hooft, E. E., & Solomon, S. C. (2007). Upper mantle structure beneath the Galápagos Archipelago from surface wave tomography. *Journal of Geophysical Research: Solid Earth*, *112*(B7).

Villagómez, D. R., Toomey, D. R., Geist, D. J., Hooft, E. E., & Solomon, S. C. (2014). Mantle flow and multistage melting beneath the Galápagos hotspot revealed by seismic imaging. *Nature Geoscience*, *7*(2), 151.

Wang, Y., Forsyth, D. W., & Savage, B. (2009). Convective upwelling in the mantle beneath the Gulf of California. *Nature*, *462*(7272), 499.

West, M., Gao, W., & Grand, S. (2004). A simple approach to the joint inversion of seismic body and surface waves applied to the southwest US. *Geophysical research letters*, *31*(15).

Wolfe, C. J., & Solomon, S. C. (1998). Shear-wave splitting and implications for mantle flow beneath the MELT region of the East Pacific Rise. *Science*, *280*(5367), 1230-1232.

Yang, Y., & Forsyth, D. W. (2006). Regional tomographic inversion of the amplitude and phase of Rayleigh waves with 2-D sensitivity kernels. *Geophysical Journal International*, *166*(3), 1148-1160.

Yang, Y., Forsyth, D. W., & Weeraratne, D. S. (2007). Seismic attenuation near the East Pacific Rise and the origin of the low-velocity zone. *Earth and Planetary Science Letters*, *258*(1-2), 260-268.

Zhou, Y., Dahlen, F. A., & Nolet, G. (2004). Three-dimensional sensitivity kernels for surface wave observables. *Geophysical Journal International*, *158*(1), 142-168.